AN ABSTRACT OF THE DISSERTATION OF

Hannah O'Hern for the degree of Doctor of Philosophy in Mechanical Engineering presented on May 18, 2022.

Title: Modeling Methods for Hydraulic Fracturing Wastewater Treatment Applications

Abstract approved: _____

Bahman Abbasi

Modeling of hydraulic fracturing wastewater treatment systems must be very accurate so it can be used for real-time modeling and control of the process. The treatment of hydraulic fracturing wastewater is complex because of the variability of the composition of hydraulic fracturing wastewater. In this work, literature review of hydraulic fracturing wastewater and its existing treatment options is presented to demonstrate the difficulties of treating this type of wastewater, including the presence of azeotropic contaminants that cannot be removed by straightforward distillation. Additionally, modeling of individual water treatment system components, in particular low-pressure Venturi mixing nozzles, was conducted using several modeling methods, including analytical, empirical, and neural network models. Both analytical and empirical models were determined to be insufficiently accurate for wastewater treatment applications despite the empirical models being at least twice as accurate as the analytical model, for this application. To create a more general, computationally efficient, and accurate model, artificial neural networks were implemented. The concept of physics-guided artificial neural networks is introduced and evaluated on three different multi-species mixing applications. It was found that physics-guided artificial neural networks can reduce the error of the model by up to 40% for a given network architecture or can reduce the network architecture, and thus computational intensity, by up to 60% for a given error value, as compared to traditional black box artificial neural networks. In order to train the physics-guided network model, both the

analytical and empirical models must be used. Once the physics-guided network model is trained it can be applied to any case within its training range with low error and computational intensity. The now-proven physics-guided network model concept can be applied to full wastewater treatment technologies, with sufficiently low error and computational intensity to be used for real-time modeling, control, and optimization of the system, using critical input parameters identified by literature review of existing treatment options.

Modeling Methods for Hydraulic Fracturing Wastewater Treatment Applications

by
Hannah O'Hern

A DISSERTATION

submitted to

Oregon State University

in partial fulfillment of
the requirements for the
degree of

Doctor of Philosophy

Presented May 18, 2022
Commencement June 2022

Doctor of Philosophy dissertation of Hannah O'Hern presented on May 18, 2022

APPROVED:

Major Professor, representing Mechanical Engineering

Head of the School of Mechanical, Industrial, and Manufacturing Engineering

Dean of the Graduate School

I understand that my dissertation will become part of the permanent collection of Oregon State University libraries. My signature below authorizes release of my dissertation to any reader upon request.

Hannah O'Hern, Author

ACKNOWLEDGEMENTS

First, I would like to thank my advisor, Dr. Abbasi, and my committee, Dr. Liburdy, Dr. Pence, Dr. Webb, and Dr. Wengrove for their support, patience, and feedback throughout my degree. I would especially like to thank Dr. Abbasi for his guidance throughout this process.

I would also like to thank my lab mates, whose proof-reading, brain storming, and moral support were indispensable.

Finally, I'd like to thank my family: my parents, my brother and sister-in-law, my partner, and my cats, for loving and supporting me unconditionally when I struggled. I truly could not have completed this degree without your constant support. Kyle, thank you for being my rock throughout this journey, and on to the next one.

Thank you!

CONTRIBUTION OF AUTHORS

Chapter Two contributions:

- Hannah O'Hern: Conducted literature review of hydraulic fracturing wastewater and the associated treatment options. Wrote manuscript.
- Elnaz Nikooei: Conducted literature review of and wrote azeotropic removal section of manuscript.
- Xiang Zhang: Contributed to manuscript revisions.
- Chris Hagen: Contributed to manuscript revisions.
- Nicholas AuYeung: Contributed to azeotropic removal section and to manuscript revisions.
- David Tew: Contributed to manuscript revisions.
- Bahman Abbasi: Conceived and led the study and contributed to manuscript revisions.

Chapter Three contributions:

- Hannah O'Hern: Conceived the study. Conducted CFD and experimental studies. Interpreted results and developed empirical models. Wrote manuscript.
- Timothy Murphy: Assisted in data collection and writing description of experimental set ups in manuscript.
- Xiang Zhang: Assisted in CFD simulations and experimental design and setup.
- James Liburdy: Significant contributions to the theory of the problem and interpreting the data to understand the phenomena. Contributed to manuscript revisions.
- Bahman Abbasi: Conceived and led the study and contributed to manuscript revisions.

Chapter Four contributions:

- Hannah O'Hern: Developed, trained and tested physics-guided artificial neural networks. Interpreted results. Wrote manuscript.

- Mohammed Elhashimi: Contributed spray humidification data and assisted in development of spray humidification analytical model.
- Bahman Abbasi: Led the study and contributed to manuscript revisions.

TABLE OF CONTENTS

Page

TABLE OF CONTENTS (Continued)

Page

TABLE OF CONTENTS (Continued)

Page

LIST OF FIGURES

Figure Page

LIST OF FIGURES (Continued)

Figure Page

LIST OF FIGURES (Continued)

Figure Page

LIST OF TABLES

Table Page

CHAPTER ONE

Introduction

Hydraulic fracturing is the practice of injecting high pressure water and additives into the ground to break open rock formations and gain access to the oil and gas trapped within. The largest byproduct of this process is hydraulic fracturing wastewater. Hydraulic fracturing wastewater is difficult to effectively manage or treat due to the variability of its composition based on the age and location of the hydraulically fractured well, as well as the company that owns the well. In order to better understand the scope of this problem as well as existing solutions, a thorough literature review was conducted. The literature review includes the production, variable composition, management and treatment methods, and azeotropic contaminant removal of hydraulic fracturing wastewater. The ultimate goal of this research is to develop a modeling tool that can be applied to a number of hydraulic fracturing wastewater treatment technologies. In order to quantify the parameters critical to the successful operation of various existing wastewater treatment technologies, it was first necessary to conduct a literature review to identify the parameters these components have in common that apply to the larger process and application rather than the specific technology. It was also found that existing literature does not consider the possibility of water-based azeotropic contaminants being present in the wastewater and therefore review of treatment options specifically for azeotropic contaminants was also necessary. In order to optimize and control hydraulic fracturing wastewater treatment systems in real time, highly accurate and computationally efficient system models are required.

To evaluate the accuracy and cost of modeling techniques for wastewater treatment systems as well as their components, empirical modeling was used to study a single component that can be applied to wastewater treatment technologies. Low-pressure Venturi nozzles were selected as a case study both because of their relevance to wastewater treatment applications and because they are difficult to accurately model analytically. In the low-pressure Venturi nozzles, losses that would be negligible in the more common high-pressure thermal ejectors are critical to the performance of the low-pressure nozzles. Even when minor losses are included in the analytical model the error

is too high for the model to be useful. For these reasons low-pressure Venturi mixing nozzles were taken as a case study and several empirical models were developed to predict the suction ratio (a key parameter to control product water purity), or ratio of suction mass flow rate to motive mass flow rate, of the nozzles based on a parametric study of 109 cases. The empirical models can be used to inform the design of low-pressure Venturi nozzles if a specific suction ratio is desired, or to determine the suction ratio of a commercially available nozzle. Two analytical models were also used to calculate the suction ratio. While the empirical models have significantly lower error than the analytical models, neither is sufficient for real time modelling and control of wastewater treatment systems. To address this issue, artificial neural networks were developed for low-pressure Venturi mixing nozzles, as well as swirling demisters and spray humidification applications, which are also relevant to wastewater treatment technologies.

In order to further reduce the error and computational cost of the neural networks, physics-guided artificial neural network framework was developed and tested on the Venturi nozzle, swirling demister, and spray humidification applications. The novel physics-guided artificial neural network methodology combined traditional black box neural networks with analytical models such that the physics-guided network model is more accurate and less computationally intensive than either the black box neural network or CFD model. The physics-guided neural network model uses the result of the analytical model as an input parameter to improve the accuracy of the network. This physics-guided neural network framework has been proven and can be applied to complete wastewater treatment systems rather than individual components, with low error and low computational intensity, as soon as enough system data is available to train and test the network.

Three research goals were identified to evaluate the above-described work:

1. Identify common parameters among existing wastewater treatment methods such that a new model can be developed based on the common parameter space to accurately model hydraulic fracturing wastewater treatment for a number of technologies.

2. Develop empirical models for a component that is not well characterized analytically to provide a design guide for applications that need precise measurement or control of the mixing ratio, such as selective condensation of water from a muti-species gaseous flow.
3. Develop framework for physics-guided artificial neural networks and optimize changes in network performance between traditional black box and novel physics-guided artificial neural networks using various components relevant to a wide variety of wastewater treatment systems.

In order to address these three research goals, first a literature review was conducted to identify the parameter space for hydraulic fracturing wastewater treatment technologies. Once the parameter space had been identified, several modeling methods were used to model individual components used in wastewater treatment to help develop the framework for a versatile neural network model that can accurately model any thermally-driven hydraulic fracturing wastewater treatment technology.

In Chapter Two, literature review of hydraulic fracturing wastewater and associated management and treatment methods is presented. This work discusses the most common treatment methods for hydraulic fracturing wastewater: the application of existing desalination technologies to wastewater. Desalination technologies are not well suited to the treatment of hydraulic fracturing wastewater due to its variability and the presence of azeotropic contaminants. Methods for the removal of azeotropic contaminants from wastewater are also presented. Existing review articles primarily focused on qualitative description of parameters and processes. To realize the goal of this research a thorough analysis of the parameter space overlap between various thermal technologies was needed to remove technology-specific elements from the modeling framework and develop a versatile tool for hydraulic fracturing wastewater treatment, instead of one applicable to a narrow range of technologies. This manuscript is published in *Desalination & Water Treatment*.

In Chapter Three, the development of empirical models to describe the performance of small-scale, low-pressure Venturi mixing nozzles is presented. These models can be used to inform the design of low-pressure Venturi mixing nozzles, or alternatively determine the suction ratio, or ratio of suction mass flow rate to motive mass flow rate,

for a given nozzle geometry. A parametric study was conducted using experimentally validated CFD simulations and the results of the parametric study were used to develop empirical models of the nozzle performance. The most general empirical model, that considers all cases studied, predicts the suction ratio within 22%, as compared to an analytical model that predicts the suction ratio within 270%. This work resulted in a manuscript published in *Applied Mechanics*.

In Chapter Four, the framework for physics-guided artificial neural networks is developed and analyzed using three case studies across various wastewater treatment technologies: low-pressure Venturi mixing nozzles, swirling demisters, and spray humidification. In each case empirical models from existing literature were used to expand the data set used to train and test the networks. The physics-guided artificial neural networks use the same system input parameters as traditional black box neural networks plus an additional input: an initial guess for the output parameter of the network. This initial guess was generated using analytical models that are insufficiently accurate to be used as standalone models, with error between 20% for the swirling demister case and 617% for the spray humidification case. By including an initial guess as an input parameter, the error of the system can be reduced by up to 40% for a given network configuration, or the network size can be reduced by up to 60% for a given error value, as compared to traditional black box neural networks. The manuscript describing this work has been submitted to *Engineering Applications of Artificial Intelligence*.

In Chapter Five, the dissertation is summarized. Each of the three research goals is addressed. The error and computational intensity of the various modeling methods considered in this work are compared. Future work for the physics-guided artificial neural network framework, both to quantify the limitations and potential applications of this type of network, is outlined.

Nomenclature, acknowledgements (if applicable) and references are provided individually at the end of each chapter.

CHAPTER TWO

Reducing the Water Intensity of Hydraulic Fracturing: A Review of Treatment Technologies

Hannah O'Hern[1], Elnaz Nikooei[1], Xiang Zhang[1], Chris Hagen[1], Nicholas AuYeung[2], David Tew[3], Bahman Abbasi[1,*]

[1] School of Mechanical, Industrial, and Manufacturing Engineering, Oregon State University, Corvallis, OR 97331, USA,
[2] School of Chemical, Biological, and Environmental Engineering, Oregon State University, Corvallis, OR 97331, USA,
[3] US Department of Energy, Advanced Research Projects Agency-Energy, Washington, DC, 20585,
[*] Corresponding author

Desalination & Water Treatment

Volume 221, 2021, 121 – 138

https://doi.org/10.5004/dwt.2021.27026

Reducing the Water Intensity of Hydraulic Fracturing: A Review of Treatment Technologies

Abstract

A novel thermal treatment technology is presented that can separate multitudes of dissolved solids, volatile contaminants, and azeotropes from wastewater, and may be able to fill a gap that currently exists in hydraulic fracturing wastewater treatment technologies. The vast majority of wastewater treatment methods are tuned to extract only certain contaminants; however, it can be difficult to predict the composition of hydraulic fracturing wastewater. This introduces a major technical challenge to design a treatment system that is largely composition agnostic. The novel technology presented in this paper uses humidification-dehumidification in nozzle-demister assembly to separate clean water from dissolved solids, suspended solids, and various volatile compounds.

Several review papers already exist that discuss the difficulties and options around the treatment of hydraulic fracturing wastewater. These tend to focus on variations of existing desalination technologies which are adopted for hydraulic fracturing wastewater treatment. These reviews are also devoid of discussion of azeotrope removal from wastewater. This paper, in addition to discussing the difficulties and existing treatments for hydraulic fracturing wastewater, analyzes the treatment options for the separation of volatile contaminants and azeotropes, and illustrates the advantages of a thermal-based treatment. Treating hydraulic fracturing wastewater is different from treating seawater or other types of wastewater due to the higher concentration and variety of contaminants. The unique challenges as well as the necessity of treating hydraulic fracturing wastewater are explained. The relative merits of several existing treatment technologies are discussed. The existing literature on the topic lacks discussion of azeotropes in hydraulic fracturing wastewater as well as which technologies can be used to remove them. This paper addresses all of the above with particular focus on separation of contaminants and water-based azeotropes.

2.1 Introduction

Hydraulic fracturing is the practice of injecting high-pressure fluid into shale rock formations to break open the rock and gain access to the oil and gas trapped within.

This process, while less water intensive than conventional oil and gas extraction methods, still uses large volumes of fresh water per well [1–3]. Additionally, not all of the water used to fracture the well returns to the surface, thus the net water lost through this process may outweigh the low water intensity in terms of net impact on water resources [4]. Approximately 30 – 92% of the injected fluid remains in the formation [2,5,6]. Between 2005 and 2014, 9.4 billion cubic meters of water were used to hydraulically fracture wells in the United States [7]. Fracturing a single well uses anywhere from 7,000 to 21,000 m^3 of fresh water [2,6]. Further reducing the water intensity of oil and gas extraction methods is necessary to reduce the total water load of energy production—especially considering the fact that ~15% of global water consumption is used for energy production [8]. The reduction of water consumption for hydraulic fracturing should be reduced whenever possible, especially in arid regions where water scarcity is already an issue.

There has been a rapid increase in unconventional oil and gas development since the beginning of the millennium, particularly in the United States [2–4,7,9–12]. In 2018, there were 139,977 hydraulically fractured wells in the United States. This is 12,846 more wells than there were in 2017 and 131,492 more wells than there were in 2000 [13]. The largest byproduct of hydraulic fracturing is wastewater. Between 2004 and 2013, the annual wastewater production from hydraulic fracturing increased 570% in Pennsylvania [1]. Additionally, water use per unit length of well has increased in recent years [4]. Natural gas production is projected to increase by 45% by 2040 [9]. As natural gas production increases, so will the consumption of water used to hydraulically fracture wells and the associated production toxic wastewater—posing serious environmental and health threats [7,12,14,15].

The contaminants in hydraulic fracturing wastewater typically come from two sources: the chemicals added to the water used to frack the well, also called hydraulic fracturing fluid, and the water native to the rock formation, also called formation water (also known as connate water). Hydraulic fracturing fluid is typically about 90% clean water, 8% sand, and 2% other additives [16,17]. Additives to the hydraulic fracturing fluid typically include gelling agents, friction reducing polymers, corrosion and scale inhibitors, surfactants, acids, and biocides, all used to increase the efficiency of the

hydraulic fracturing process [1,18]. Table 2.1 summarizes common chemicals in hydraulic fracturing wastewater as well as their concentrations five days after the well was drilled. While there are any number of chemicals a company could use, there are about 60 that are commonly used in industry, and only about 12 chemicals used per well [18]. The actual chemicals added to the water vary from company to company and well to well. The chemicals in the injected fluid may return to the surface in wastewater, may remain in the formation, or may degrade [19]. Additionally, chemical reactions may take place between the additives and formation water which create compounds more toxic than the parent compounds [7]. In the well, the chemical additives are exposed to high temperatures, pressures, and salinities, as well as a range of pH levels [20,21]. The conditions in the well, or downhole conditions, are extremely variable and may even differ between wells in the same shale play [20]. Some common additives have been studied in downhole conditions to determine how the reaction mechanisms may differ from near-surface environment reactions. One of the most commonly used biocides in hydraulic fracturing is glutaraldehyde. The downhole reactions of glutaraldehyde were found to be a function of temperature, pH, and salinity [20]. Additionally downhole decomposition of some corrosion inhibitors has been shown to produce hydrogen sulfide gas [21]. Given the extreme and unpredictable nature of downhole well conditions it can be difficult to predict the downhole reactions of hydraulic fracturing additives [20].

Wastewater may contain salts, metals, metalloids, organics, or naturally occurring radioactive materials at various concentrations. The contaminants in the wastewater as well as their concentrations are a function of the additives in the hydraulic fracturing fluid, the local geology, and the time [3,7]. The salinity of the wastewater can vary from nearly that of fresh water to 14 times that of seawater, and the pH can be lower than that of produced water from oilfields or coalmine drainage [22,23].

Table 2.1: Most common components in hydraulic fracturing wastewater and their concentration in the wastewater 5 days after the well was fractured [24].

Compound	Boiling point (°C)	Density (g/ml)	Concentration 5 days (ppm)
Total dissolved solids (TDS)	-	-	94,000
Ammonia	-33	0.77	70
Benzene	80	0.89	625
Toluene	100	0.88	833
Ethylene glycol	197	1.11	29,700
2-Butoxy-ethanol	171	0.9	10,000
Other: chlorides, sulfates, Na, B, Sr, Ba, trace compounds			Chlorides + Na: 98,000

Wastewater is typically separated into two types: flowback water and produced water. Flowback water is the wastewater produced immediately after the well is drilled and is produced at a relatively high flowrate, up to 1000 m^3 per day. It typically has contaminants that are very similar to that of the hydraulic fracturing fluid. After the flowback period ends (~2 - 3 weeks), produced water is then recovered from the well for the remaining life of the well (~30 - 40 years) at a relatively low and constant flowrate, between 2 and 8 m^3 per day [25,26]. Produced water typically has characteristics similar to that of the brackish formation water, or water that was contained within the rock formation before the well was drilled, and therefore is more saline than the flowback water [1,27]. While flowback and produced waters are considered to be different by the oil and gas industry, they are both ultimately wastewater that will be disposed of or treated [7]. On average, produced water tends to be extremely saline with salt concentrations greater than 100,000 mg/L [28]. The most common salt in the wastewater is NaCl. The salt concentration tends to increase with time as the wastewater is in contact with the native brine for more extended periods of time. As the salt concentration increases, the concentration of naturally occurring radioactive material increases as well. The naturally occurring radioactive material is typically radium [16,29–33]. The change from flowback to produced wastewater is relevant to treatment because it demonstrates the temporal change in composition of the wastewater. A treatment that is well suited to the treatment of flowback water may not be suitable to treat produced water, or vice versa.

Hydraulic fracturing wastewater composition varies significantly [34]. Produced waters from the Marcellus (PA), Eagle Ford (TX), and Barnett (NM) shale plays were tested and the ten most common chemicals in produced waters were found to be sodium, potassium, lithium, magnesium, calcium, strontium, iron, silicon, sulfur, and phosphorus. However, even among the most common chemicals in produced water the concentration of the chemicals varies by orders of magnitude between plays [35]. Over 1000 organic compounds have been identified in wastewater samples [34]. Volatile organic compounds, such as toluene and benzene, have also been found in wastewater samples [36]. Volatile organic compounds are toxic and may cause health issues even in low concentrations if not properly removed and disposed of [37].

2.2 Hydraulic fracturing wastewater management

Due to the toxicity, high levels of salinity, total dissolved solids (TDS), and total suspended solids (TSS), proper management of hydraulic fracturing wastewater is difficult. The concentration of TDS tends to be much higher for wastewater produced by hydraulic fracturing as compared to other types of oil and gas production [38]. The range of TDS levels as well as its average level will vary based on local geology. For example, the Denver-Julesberg formation has TDS levels ranging from 20,000 to 65,000 mg/L, and the Bakken formation has values ranging from 150,000 to 300,000 mg/L [39]. Wastewater from the Marcellus formation in Pennsylvania has TDS levels ranging from 8,000 to 360,000 mg/L, with an average around 100,000 mg/L [6,25,27]. The suspended solids in the wastewater are largely made up of the sand used as proppant in the hydraulic fracturing fluid. TSS levels in wastewater range from 300 to 3,000 mg/L [40].

High salinity wastewater is not suitable to be treated by traditional wastewater treatment operations, among other reasons because the salt can harm the biological treatment processes that are common to municipal wastewater plants and therefore specialized methods of wastewater treatment are necessary [41]. About 95% of the wastewater produced in the United States is temporarily stored in surface pools before being transported to deep injection wells for disposal [42]. Deep injection disposal wells, also called Class II disposal wells, are geologically isolated from the hydraulic fracturing wells and are solely used for injection of wastewater, as shown in Figure 2.1.

Numerous production wells utilize the same disposal well. There are about 36,000 deep injection disposal wells in the United States, so the wastewater from a hydraulic fracturing well will be transported, sometimes across state lines, to a disposal well. Approximately 7.5 million cubic meters of wastewater are disposed of in deep injection wells every day in the United States [43].

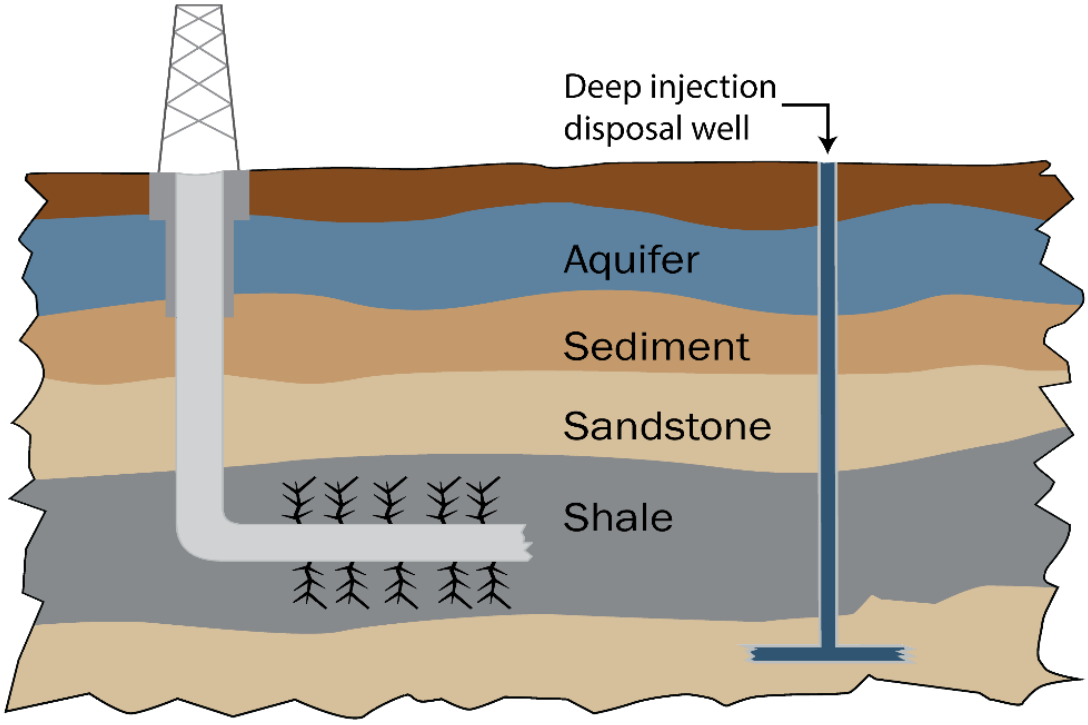

Figure 2.1: Schematic of a hydraulic fracturing well (left) and deep injection disposal well (right).

The annual cost associated with the transportation of hydraulic fracturing wastewater is estimated to have reached $2.1B in 2020 [10]. The transportation of wastewater to centralized disposal wells represents a significant expense for the industry, as well as an environmental risk. Approximately half of the wastewater produced over the lifetime of a well is produced in the first few weeks given the high flowrate of flowback water [44]. If a low cost on-site treatment approach was available, it would be more economical to treat wastewater where it is produced than at a central facility. Also, the on-site treatment of the wastewater may reduce many of the concerns about the management and potential risks of the wastewater [28]. Table 1.2 lists the approximate cost ranges of some disposal and treatment methods used in the industry. Such figures

tend to be proprietary information and are extremely difficult to find in publicly-accessible resources. Table 2.2 shows figures based on one source [45].

Table 2.2: Treatment cost for some existing approaches [45].

Disposal or treatment method	**Cost ($/m^3)**
Underground injection	10 – 16
Membrane-based	19 – 62
Ion exchange	13 – 50
Electro-coagulation	13 – 31
Chemical precipitation	19 – 31

Surface pools, transportation, and disposal wells all represent potential environmental and health risks. If the water seeps into the ground from a surface pool or leaks out of a disposal well, the contaminants can affect local ecosystems or water supplies. The most common sources of contamination from hydraulic fracturing wastewater are surface leaks and spills, illegal disposal, and inadequate treatment and discharge of wastewater [29,46]. Additionally, deep well injection has been shown to induce seismicity in the region of the disposal well [47–50]. In the central United States, where approximately 85% of all Class II injection wells are located, there has been an 804% increase in the number of earthquakes per year between 1973 – 2008 and 2009 – 2014 [48,51]. Fortunately, with the right approach, treatment and reuse can be an attractive alternative to surface storage and deep well injection.

The most common form of reuse is using wastewater as the hydraulic fracturing fluid for a new well. However, some treatment is still required. Without any treatment, wastewater would typically be unsuitable for fracturing new wells due to high concentrations of salt, hydrocarbon, grease, and biological matter [35]. Typically, the wastewater is filtered to remove the TSS and then mixed with fresh water before being used as hydraulic fracturing fluid [6]. While there are no uniform standards for the quality of the wastewater used to frack new wells, the water typically would not be reused when the TDS concentration is greater than 50,000 – 60,000 mg/L [3,17]. The treatment requirements vary based on what components are present in the wastewater, as well as the new well's geology and hydraulic fracturing company. This form of reuse is only feasible while new wells are being hydraulically fractured. When more

wastewater is being produced than can be reused to hydraulically fracture new wells, a new reuse or treatment option will be necessary [6,52].

Beneficial reuse of the wastewater could help alleviate water scarcity issues rather than adding to them; however, nearly all beneficial reuse applications require significant treatment. One of the only cases of untreated wastewater being used outside of the oil and gas industry is dust suppression. Some states, including North Dakota, South Dakota, Nebraska, Kansas, Wyoming, Michigan, Indiana, Ohio, New York, Pennsylvania, and West Virginia, allow untreated wastewater to be sprayed on roads for dust control [28,53–55]. Beneficial reuse of treated water would include agricultural irrigation or livestock watering. All of these applications have minimum water quality standards. Agricultural irrigation is the most common application for beneficial reuse for treated wastewater from other industries [56].

2.3 Hydraulic fracturing wastewater treatment

Treatment options for hydraulic fracturing wastewater often utilize well-established desalination technologies, such as reverse osmosis (RO), forward osmosis (FO), membrane distillation (MD), multistage flash distillation (MFD), multi-effect distillation (MED), and mechanical vapor compression (MVC) [57]. However, hydraulic fracturing wastewater and the seawater for which these technologies are optimized are very different. A desalination technology that works well for seawater treatment will not necessarily work well for wastewater treatment. The treatment of hydraulic fracturing wastewater poses unique challenges. Many technologies are limited by the TDS levels in the wastewater. Membrane based technologies (RO, FO, MD, etc.) also face the issue of fouling. Membrane processes rely on membranes that are specifically designed to work with a particular wastewater or separate specific contaminants. Hydraulic fracturing wastewater is highly variable and therefore it is difficult to design a membrane or draw solution that can treat all wastewaters. Additionally, azeotropic mixtures may exist in the wastewater which are mixtures that cannot be separated by simple distillation. One example is the binary azeotropic mixture of n-heptane and isoamyl alcohol in the chemical industry wastewater [58]. Another example is the wastewater from isopropanol industries. Such wastewater contains benzene and isopropanol which can form different azeotropes (i.e. binary or

ternary, and heterogeneous or homogenous) with water [59]. Most analyses of hydraulic fracturing wastewater are focused on organic compounds and further investigation is necessary in order to quantify the most common azeotropes in this kind of wastewater [19,34,35].

2.3.1 Membrane-driven technologies

Membrane-driven technologies have the benefit of successfully filtering suspended solids and volatiles, but have the drawbacks of membrane fouling and the fact that it is not feasible to tailor membranes and draw solutions to each hydraulic fracturing wastewater stream due to their high compositional variability. Osmotic backwashing cleaning via the circulation of deionized water on both sides of a membrane has been shown to effectively restore water flux through membranes that has been reduced by fouling [60–63]. Additionally, backwash using ultrafiltration permeate, reverse osmosis concentrate and permeate, nanofiltration permeate, and forward osmosis draw solution have been used to membrane reduce fouling due to hydraulic fracturing wastewater [64]. To alleviate fouling issues, membrane-driven technologies typically utilize pretreatment to slow the fouling of the membrane [65,66]. Additionally, membrane treatments may be used to reduce membrane fouling in place of pretreatment. Use of double skinned membranes and zwitterionic polymers has been shown to significantly reduce membrane fouling and maintain water flux through the membrane [67]. There has also been anti-fouling progress using superhydrophilic ceramic membranes that have been shown to maintain permeate flux for at least ten days [68].

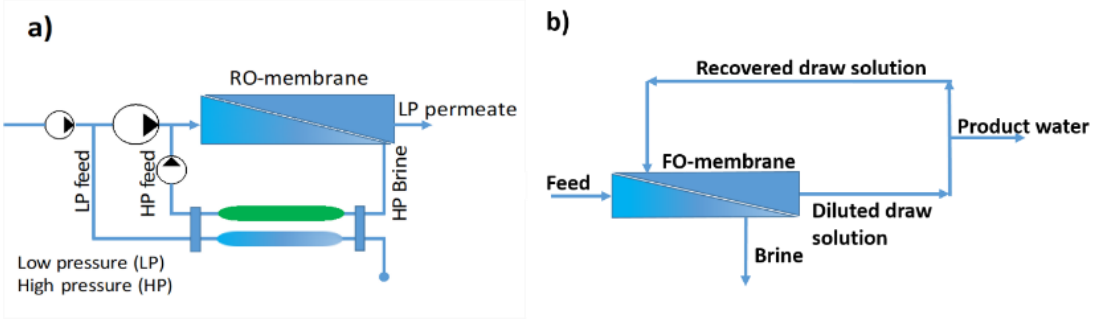

Figure 2.2: Typical schematic of common membrane driven treatment technologies: a) RO, b) FO [57].

2.3.1.1 Reverse osmosis for wastewater treatment

Reverse osmosis uses high pressure to force clean water through a semi-permeable membrane. Clean water is collected on one side of the membrane and concentrated brine effluent is collected on the other side. This process is shown in Figure 2.2a. However, for wastewater applications, this process is of limited applicability. Unfortunately, conventional RO is not economically attractive at TDS levels greater than 30,000 – 33,000 mg/L [69], and conventional RO is not capable of treating water with TDS levels in excess of 40,000 mg/L [10]. RO accounts for about 60% of the desalination of seawater and brackish water worldwide [70].

There are modifications to the traditional RO process that can increase the maximum treatable TDS level. Closed circuit desalination (CCD) increases the pressure on the feed side of the membrane with time, so as the concentration of the feed side increases the pressure used to overcome the osmotic pressure of the membrane also increases [71]. Given that hydraulic fracturing wastewater salinity also increases with time, the increase in pressure of CCD may help to treat the higher salinity produced water later in the life of the well. CCD RO was evaluated for hydraulic fracturing wastewater, and a TDS removal of 99.6% was obtained [72]. Additionally, a permeate side sweep, which uses fresh water to reduce the osmotic pressure gradient across the membrane, can be used. This is called osmotically assisted RO, which has been experimentally shown to increase the maximum TDS level to 100,000 mg/L – 140,000 mg/L [73]. Given the TDS limits, RO alone may be limited to a pre- or post-treatment, but when

modifications such as CCD or osmotic assistance are made to the process it may be suitable as a standalone treatment for hydraulic fracturing wastewater.

2.3.1.2 Forward osmosis for wastewater treatment

Forward osmosis utilizes a draw solution on one side of a semi-permeable membrane to draw clean water through the membrane, leaving a concentrated effluent. The water that permeates through the membrane mixes with the draw solution and must then be separated from the draw solution, as shown in Figure 2.2b. The limiting factor for this process is the concentration of the draw solution. The osmotic pressure across the membrane must push water to the draw solution, or more concentrated side of the membrane. If the wastewater is more concentrated than the draw solution, the FO will not purify water. There needs to be a draw solution that works for even the most contaminated wastewater. In order to maintain the concentration of the draw solution, another process, such as RO or distillation, must be used to separate the treated water from the draw solution [74,75]. For FO, the TDS limit of treatment is typically 70,000 mg/L, but can be as high as 200,000 mg/L depending on the membrane [3,6,74]. A drawback of FO is that it is a relatively slow process. In the absence of high pressure forcing fluid motion through the membrane, the water permeates through the membrane very slowly [66]. On the other hand, a significant advantage to FO is that it has been shown to be capable of producing treated water that meets surface discharge and drinking water standards [66,76,77].

Alternatively, if purity of the treated water is not critical, the draw solution and treated water may not need to be separated; this is called osmotic dilution mode. For this type of operation, there is no re-concentration of the draw solution, instead the dilute draw solution is the product of this process and new draw solution is constantly introduced to the system [78,79]. Osmotic dilution may be well suited to the treatment of hydraulic fracturing wastewater as the draw solution concentration will not decrease with time. Osmotic dilution FO has been applied to the treatment of oil and gas wastewater in the Haynesville shale formation via the Green Machine, developed by Hydration Technology Innovations (Albany, OR) and Bear Creek Services (Shreveport, LA) [66,80]. The Green Machine treats over 80% of the wastewater from any given well. This water has been internally reused to hydraulically fracture other wells [66].

2.3.1.3 Membrane distillation for wastewater treatment

Unlike other membrane separation processes, membrane distillation (MD) is a thermally-driven process and the driving force for each component to pass through the membrane pores is its partial pressure gradient in the vapor phase inside the pores due to the temperature difference across each pore [81]. The hydrophobic, microporous membrane prevents liquids or solutions from entering its pores due to the surface tension forces. In the MD process a liquid feed mixture at relatively high temperature, typically 60 – 90°C, will be in contact with one side of a porous membrane which separates the warm solution of feed mixture and the permeate that then enters into a cooling chamber [81]. The more volatile component moves as vapor phase, from the feed mixture to the permeate side of the membrane. At the permeate side this vapor is either condensed or convected away from the membrane module, depending on the MD configuration. As a result, the feed side will be concentrated. MD is a thermally-driven technology, but because it utilizes a membrane, it is susceptible to fouling [82]. However, because the membrane in MD is not a physical barrier to contaminants, rather a support for the vapor-liquid interface, membrane fouling is less of an issue than it is for other membrane technologies, like RO and FO [81]. When MD was tested with hydraulic fracturing wastewater, iron-based deposits formed on the membrane, but was shown to have negligible effects on the performance of the membrane [31].

MD has been used to treat wastewater from a number of industries, including textile and pharmaceutical, as well as wastewater containing heavy metals and wastewater containing sulfuric acid solutions [83–86]. One of the benefits of using MD as a hydraulic fracturing wastewater treatment is that it is not significantly affected by salinity [3,6]. Therefore, the temporal change in salinity of hydraulic fracturing wastewater would not significantly impact the operation of MD. This process is capable of treating wastewater with TDS levels up to 350,000 mg/L [65]. MD has been shown to outperform RO and evaporative crystallization for hydraulic fracturing wastewater treatment, with ion removal efficiencies above 99.9% [87]. Additionally, MD tends to operate at temperatures near those typical of produced water [3]. In some cases MD has been paired with other technologies, such as precipitative softening and walnut

shell filtration, to treat hydraulic fracturing wastewater with water recovery rates greater than 80% [88].

2.3.1.4 Other membrane technologies

RO, FO, and MD are by far the most common membrane driven treatment technologies, but there are a number of other, less common, membrane technologies that may be used for this application, at least as a pre- or post-treatment. Ultrafiltration (UF) and microfiltration (MF) are low pressure membrane-driven processes. Given the low pressure demand of these processes, they have a relatively small footprint which makes them suitable for on-site treatment [65]. UF & MF operate at pressures ranging from 0.5 to 5 bar [89]. UF & MF are rarely used as independent processes, but are commonly used as a pretreatment for RO, FO, or membrane distillation [90–92].

Electrodialysis is an electrically-driven membrane process that has been shown to treat wastewater with TDS levels, below 5,500 mg/L, to drinking or livestock watering quality, making it a promising post-treatment option for treatment processes not capable of reducing TDS levels so dramatically [93]. For example, electrodialysis could be used as a secondary treatment after RO or FO to increase the quality of the clean water.

2.3.2 Thermally-driven technologies

Thermally-driven technologies are better able to deal with high levels of salinity and avoid issues with membrane fouling or the need of specifically tailored membranes or draw solutions. However, due to the lack of a physical filter, these processes do not always remove volatiles. Evaporation or crystallization have been suggested as the only ways to successfully treat high salinity wastewater in a single process [5,94]. Additionally, for on-site hydraulic fracturing wastewater treatment applications, thermal processes can take advantage of otherwise waste thermal energy from the flared gas [95].

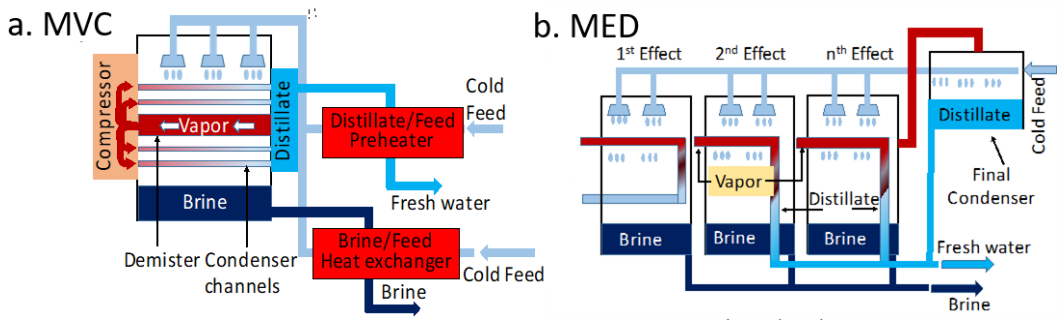

Figure 2.3: Schematic diagrams of common thermally-driven treatment technologies: a) MVC, b) MED [57].

2.3.2.1 Mechanical vapor compression for wastewater treatment

In a mechanical vapor compression (MVC) system, heat is transferred to the wastewater from superheated compressed vapor in a tube evaporator. The wastewater is sprayed over the tube evaporator and the steam is then mechanically compressed and the distillate is collected in condenser channels. The main demand of energy for this process is the electricity or mechanical energy required to compress the vapor [96]. The heat required to evaporate the wastewater, on one side of the tube evaporator is supplied by the condensation of the distillate on the other side of the tube evaporator [97]. Additionally, the hot condensate is used to preheat the incoming wastewater to increase the energy efficiency of the system. A schematic of an MVC system is shown in Figure 2.3a. The main advantages of MVC are that it does not require pre-treatment because it is not prone to fouling or clogging, and that it can treat wastewater with TDS levels up to 200,000 mg/L [3].

2.3.2.2 Multi-effect distillation for wastewater treatment

Multi-effect distillation (MED) is a process in which feed water is sprayed over a hot tube bank. Some of the water will evaporate and will move to the next effect where the clean steam will be used as the heat source for the tube bank. Concentrated brine will be collected at the bottom of the system. Some of the steam will condense inside the tubes and will be collected as clean product water. The number of times the steam is used as the heat source for a tube bank defines the number of effects, as the number of effects is limited by the temperature difference between the condensing temperature at the first effect and the condensing temperature at the last effect [98]. Each successive

effect will take place at a lower temperature and pressure. This process is shown in Figure 2.3b.

MED is one of the oldest desalination technologies and can effectively treat high salinity feeds [98–100]. MED has been tested as a hydraulic fracturing wastewater treatment only after significant pretreatment. The pretreatments were done to remove organics and oils from the wastewater prior to the MED process. The number of effects in MED is important to the operation of the process as the number of effects becomes a trade-off between the cost of the process and the quality of the treated water [101].

2.4 Azeotrope separation techniques

There are a number of reviews on the topic of hydraulic fracturing wastewater [1,3,7,11,12,17,29], however, these reviews do not mention the formation of azeotropic mixtures in hydraulic fracturing wastewater. Removing contaminants that form azeotropes in the wastewater requires specialized methods beyond desalination treatments adapted to hydraulic fracturing wastewater. Therefore, there is a gap in existing review literature on this particular type of contamination and its removal methods.

An azeotropic mixture is one in which the equilibrium compositions of the vapor and liquid phases are the same and do not change with simple distillation. Consequently, conventional distillation cannot be used to separate azeotropic constituents. Non-ideal behavior of some components in a mixture can yield azeotropic systems. If the components are dissimilar, repulsion forces are very strong, and activity coefficients are greater than unity, then minimum-boiling azeotropes can form. Alternatively, if the components are similar, attract each other, and activity coefficients are less than unity, then maximum-boiling azeotropes can form [102]. The separation techniques used for azeotropic separation can be divided into two main categories: enhanced distillation techniques and membrane processes; however, there are other emerging techniques which have been investigated in some studies but are not yet industrialized. Also, there are treatment systems which take advantage of the combination of multiple separation methods. The most significant distillation techniques suitable for azeotropic separation, which are discussed in later sections, include azeotropic distillation, extractive distillation, pressure swing distillation and fixed-bed adsorption distillation; while

suitable membrane processes include pervaporation, vapor permeation, membrane distillation and frictional diffusion.

2.4.1 Distillation

Azeotropic distillation and extractive distillation are techniques based on the addition of a third component called an entrainer that alters relative volatility of components of the original azeotropic mixture. In azeotropic distillation, this leads to the formation of a new azeotrope with properties that differ from the target compound and enables separation. According to the number of phases present in the new azeotrope mixture, the azeotropic distillation will be either homogeneous or heterogeneous [103].

Considering a binary azeotropic mixture as a reference, in heterogeneous azeotropic distillation, adding the entrainer will increase the volatility of one of the two components, leading to a mixture of two liquid phases after the vapor from overhead is condensed. In this case, the process will consist of two distillation columns and a decanter to separate the entrainer from the other component [104–106]. In homogeneous azeotrope separation, however, the overhead product is one liquid phase, so a liquid-liquid extraction column is needed after the first column to separate the overhead product from the entrainer [105]. In industrial applications of azeotropic distillation, it is more common to form a heterogeneous minimum temperature azeotrope. In this way one of the components and the entrainer will be carried to the overhead of the column and then a decanter is applied to separate the two liquid phases [104]. Jordi et al. [103] used Aspen Hysys to simulate azeotropic distillation for a binary mixture of 1-propanol and water at 101.3 kPa, using diisopropyl ether as the entrainer. They showed that it is an effective entrainer for 1-propanol dehydration. In an experimental study, Vicente et al. [107] studied different potential entrainers for ethanol dehydration in azeotropic distillation. They performed the experiments in a pilot scale azeotropic distillation column and showed that naphtha is an effective entrainer for such azeotopic separation. Puyun et al. [108] also proposed two azeotropic distillation processes for the separation of azeotropic mixture of 2,2,3,3-tetrafluoro-1-propanol and water, using chloroform and p-xylene as two potential entrainers. They showed their experimental results are in good agreement with those from the simulation.

2.4.2 Extractive distillation

The extractive distillation method is similar to azeotropic distillation in terms of adding a third component to the azeotropic mixture, but they are different processes. In azeotropic distillation, the entrainer is a more volatile component than the azeotropic solution. Therefore, it changes the volatility of one of the two components and will be taken from the overhead of the column along with that component. Adding the third component in azeotropic distillation forms a new azeotrope, however, in extractive distillation adding the third component (solvent agent) only increases the relative volatility and does not form an azeotrope with any of the components of the original mixture. The other important difference is that the solvent agent added into an extractive distillation process is a heavy substance with a high boiling point which will be recovered from the bottom of the second column; while in azeotrope distillation, the entrainer added to the separation process is a low boiling point substance that will be recovered from the top of the column. Azeotropic distillation, compared to extractive distillation, uses more energy to vaporize the entrainer at the top of the column [103,106,109].

In extractive distillation, a sufficient change of relative volatility is essential within the separated components when the solvent agent is added to the feed mixture. The solvent agent can be either solid salt, liquid solvent, a combination of solid salt and liquid, or ionic liquid. Selecting a suitable solvent is important to ensure effective and economical separation. Using solid salt as the solvent agent has the advantage of high separation ability; however, such salts be decomposed at high temperatures and can corrode the equipment. Liquid solvents may not have the same high separation capacity as solid salt, but are widely used due to the ease of their transport and recovery [110,111]. Extractive distillation using a mixture of solid salt and liquid solvent is a promising method for separation, since it integrates the advantages of solid salt and liquid solvent techniques, but it needs to be economically viable. Extractive distillation with ionic liquids has many advantages, including negligible vapor pressure (which means it does not pollute the top product of the column), as well as high thermal and chemical stability under the operating conditions of extractive distillation columns. However, distillation using liquids is not very common in industry due to material cost

[111]. Yong et al. [112] carried out some experiments to study the effect of deep eutectic solvents (DES) on the elimination of mixture's azeotropic point in an extractive distillation process. They used an ethanol-water system as it is a typical industrial azeotropic mixture and showed that adding ChCl/urea as the entrainer can increase the relative volatility of the mixture to more than 4.7 times and eliminate the azeotropic point [112]. In another study, Wang et al. [113] used the UNIQUAC model to investigate the separation of acetone and chloroform mixture by adding N-methyl-2-pyrrolidone (NMP) as the heavy entrainer in an extractive distillation column. They compared their results with those from previous works that used dimethyl sulfoxide or ethylene glycol as the entrainer to show that using NMP is more economic in separation of this maximum-boiling azeotropic mixture.

2.4.3 Pressure swing distillation

Another distillation technique for azeotrope separation is pressure swing distillation which takes advantage of the fact that the azeotrope point can be shifted by changing the pressure when the azeotropic mixture is pressure sensitive. In this way, a homogeneous azeotropic mixture whose azeotrope point changes with pressure can be separated. This method applies two distillation columns working at two different operating pressures: one at low pressure and the other at high pressure. Depending on the type of azeotrope (i.e. maximum boiling or minimum boiling) the products are collected from the top or bottom of the column [59,105,114,115]. Figure 2.4 shows a schematic of pressure swing distillation for a minimum boiling azeotropic mixture.

Yue et al. [59] studied the separation of a ternary mixture of benzene, isopropanol, and water. They compared the simulation results for two different techniques: pressure swing distillation and heterogeneous azeotropic distillation. The results from their study showed that total annual cost for pressure swing distillation is almost half of the combination of both techniques, so it is a more economic and energy efficient method. They also showed that pressure swing distillation is an effective method for wastewater treatment containing benzene and isopropanol. William L. [116] applied Aspen to simulate and optimize the separation of a binary mixture of methanol and trimethoxysilane in a pressure swing distillation process. The above mixture forms a maximum-boiling homogeneous azeotrope at 1 bar and 87.94°C when the

concentration of methanol reaches to 28.65 mol %. In this study, they showed the optimum operating condition for the low pressure and high pressure columns are 0.25 and 7 bar, respectively. Furthermore, Shisheng et al. [117] have explored various aspects of pressure swing distillation, especially the application of this method in azeotrope separation, and published their review study in 2017.

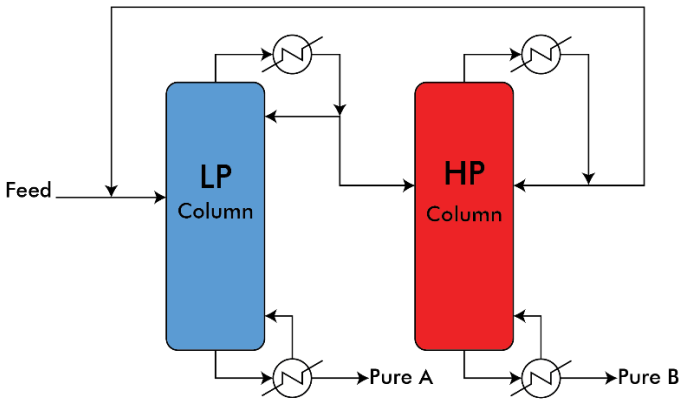

Figure 2.4: Schematic of pressure swing distillation for a minimum boiling azeotropic mixture.

There are other distillation techniques that are applicable for azeotrope separation, such as fixed-bed adsorption distillation which applies molecular sieves as active packing material in a packed-bed distillation column instead of the conventional inert packing materials. Molecular sieves can alter the vapor-liquid equilibrium of feed components and improve the relative volatility to help azeotropic mixture separation [118]. An azeotrope dividing wall column is another enhanced distillation column technique useful in azeotrope separation. The dividing wall column reduces the number of required columns by installing a partition wall inside the column which leads to a significant reduction in energy consumption and capital cost.

2.4.4 Membrane distillation for azeotrope separation

Conventional distillation and membrane distillation both depend on vapor-liquid equilibrium as the basis for separation. However, the most significant difference between these processes is the feed water temperature. Membrane distillation does not require heating the feed to its boiling temperature, which is necessary for conventional distillation. Moreover, the target components to be separated can have similar boiling points or form azeotropes. There are four different configurations developed to perform

membrane distillation: direct contact membrane distillation (DCMD), air gap membrane distillation (AGMD), sweeping gas membrane distillation (SGMD), and vacuum membrane distillation (VMD). They differ in the way in which the vapor is condensed and/or removed from the membrane distillation module. Sarita et al. [119] carried out experimental studies on the separation of HCl–water azeotropic mixture (20.2 wt% HCl) using air gap membrane distillation. Specifically, they investigated the effects of parameters such as feed temperature, air gap widths and selectivity on the permeation and total flux. Their experimental results also showed there is an increase in permeate flux by decreasing air gap thickness and increasing temperature at the air gap. They showed that 31 wt% is the maximum concentration level of HCl achievable at 45°C of feed temperature. They also developed heat and mass transfer correlations for this separation process [119]. Hong et al. [120] introduced a methodology for designing and optimizing a membrane-assisted distillation process for dehydrating ethanol which is a common example of aqueous azeotrope dehydration in industry. They showed that enriching the ethanol up to 99.6 wt% is achievable by using their methodology to define the optimum hybrid configuration. More information can be found in [121].

2.4.5 Pervaporation

Membrane-based processes are cleaner than conventional distillation because they require less energy and do not need additional chemicals. Pervaporation is an effective membrane technique for azeotropic separation. Unlike distillation, it is not limited by the thermodynamic vapor–liquid equilibrium. In distillation, separation is based on the difference in relative volatilities of the components. However, in pervaporation the driving force for separation is the difference in chemical activity and diffusion rate of the components into a membrane [122,123]. Pervaporation is an energy efficient process compared to most conventional separation methods such as distillation because only the latent heat of minor component that permeates within the membrane must be supplied. Also, pervaporation units often have small footprints and do not require entrainers [123,124]. Nitin et al. [122] built up an experimental setup to study the pervaporation separation of two azeotropic mixtures: ethanol/water and acetonitrile/water. They performed experiments to investigate the effects of feed

temperature and solution concentration on the separation process. They also carried out experiments for two different membranes: poly vinyl alcohol (PVA) and PVA-poly ether sulfone (PES). Results from their experiments revealed that the flux of both membranes increases by increasing the feed temperature and concentration. They showed for both binary systems, using PVA-PES membrane in pervaporation leads to a higher flux [122]. Pervaporation has been proven to be one of the most promising techniques for azeotrope separation. However, choosing a suitable membrane is crucial, as it affects the efficiency of the separation. In this regard, Yee et al. [124] have accomplished a review study on recent development of membranes in pervaporation processes.

2.4.6 Vapor permeation

Vapor permeation is similar to pervaporation, except that in vapor permeation the feed is a gaseous as opposed to a liquid mixture. In the vapor permeation process, the feed temperature and the driving force do not reduce within the vapor permeation module, so there is no need for a heat exchanger after each module. A vacuum is often needed on the permeate side to run the process at lower pressures which leads to lower condensation temperatures. Consequently, it has high operating costs due to the need for low operating pressure and is usually not used as a standalone separation unit. In many applications, because of high operating costs of the pervaporation technique, a more economical way is to use pervaporation or vapor permeation only to break the azeotropes and then couple that with a secondary separation process such as distillation columns [125,126]. Petr et al. [127] carried out experiments to compare pervaporation and vapor permeation techniques with different membranes. They examined the separation of an azeotropic mixture of dimethyl carbonate and methanol, and asserted that vapor permeation using PIM-1 membranes is the most selective membrane-based technique in removing the dimethyl carbonate from this azeotropic mixture.

2.4.7 Frictional diffusion

In 2007, Marcel at al. [128] introduced a novel separation technique for azeotropic mixtures. They claimed that by using a gas that has a higher binary diffusive friction with one of the two components of a binary azeotropic mixture, diffusion of the gas leads to the separation. They modeled this concept and performed the experiments in a

shell and tube module with a counter current configuration similar to what is shown in Figure 2.5. In order to prevent the mixing of feed mixture with the enhancer gas (sweep gas), they applied a porous barrier. Using CO_2 as the enhancer gas for the separation of ethanol/water mixture, they performed the experiments and provided results to support this novel concept which they named frictional diffusion [128]. Frictional diffusion (also called friction difference or FricDiff) is based on the difference in diffusion rates of the constituents of a gas or vapor mixture when they diffuse through an enhancer gas. In this separation technique, flow of the feed mixture and that of enhancer gas are separated by a porous barrier. The feed mixture passes through this nonselective barrier and gasses diffuse due to the concentration difference of the components on each side. For example, heavier components in the feed mixture have lower diffusion rates as they have larger molecular weights. So they have more friction with the sweep gas. This leads to enrichment of the target product either on the feed or sweep side. One of the advantages of this separation process is low energy consumption and absence of hazardous solvents [106,126]. However, pressure drop across the porous barrier should be minimized as it causes convective mass transfer and adversely affects the separation. Breuer et al. were another group who examined using FricDiff for the separation of an azeotropic mixture of 2-propanol and water. They studied the effects of operating conditions and the porous barrier on the separation process using a detailed numerical model [126].

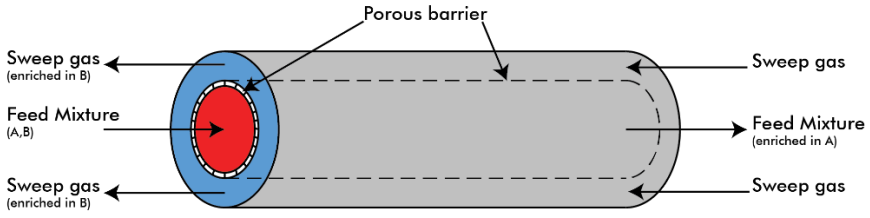

Figure 2.5: Schematic of frictional diffusion.

Table 2.3 shows a summary of separation techniques that can be useful in azeotrope separation.

Table 2.3: Separation techniques applicable for azeotrope separation.

Separation Processes			Description	Advantages	Drawbacks	Ref
Distillation	**Azeotropic distillation (AD)**		A third component (entrainer) is added to the mixture. The entrainer is more volatile than the azeotropic solution and increases the volatility of one of the two components, facilitating the separation.	• Well understood process • Abundant theoretical and practical knowledge	• Energy intensive • Large column diameter • More difficult control • Need for a secondary distillation of the entrainer	[103–105,107,109,114,115,129,130]
	Azeotrope dividing wall column (A-DWC)		Only requires one column for separation. This leads to energy savings and significantly reduces the capital and operating cost.	• Low capital cost	• High actual steam cost due to combining two reboilers into one	[131,132]
	Extractive distillation (ED)	**with solid salt**	A third component (separating agent) is used to change relative volatility of the components and overcome the azeotrope. For binary feed, one pure component exits as the top product of first column and the other component plus solvent agent accumulates at the bottom and can be separated in a secondary distillation column.	• High separation ability	• Corrosion	[110,111,133–137]
		with liquid solvent		• Easy operation • No problems of dissolution, reuse and transport	• High consumption of energy in case of large solvent ratio • Impurities in the top product because of volatile solvents	
		with a mixture of solid salt and liquid solvent		• Easy operation • High separation ability	• Impurities in the top product because of volatile solvents • Corrosion and salt decomposition at higher temperature • Impurities of solvent in the products	
		with ionic liquid		• Easy operation • High separation ability • Negligible vapor pressure at room temperature (i.e. lower loss of solvent and no impurities in the top product)	• High cost • Impurities of solvent in the products • Large energy consumption and capital investment	

Separation Processes		Description	Advantages	Drawbacks	Ref
			• Operating at a wide temperature range	• Difficulty of controlling the process due to the use of a third components • Need for a secondary distillation of the auxiliary solvent	
Distillation Processes	**Pressure swing distillation (PSD)**	It takes advantage of the sensitivity of the azeotrope point to pressure variation in order to accomplish the separation in a two-column process operating at different pressures.	• Low contamination in the product due to the absence of a third component	• Complexity of operation and process control • Decomposition of heat-sensitive components with increasing pressure • Higher operating cost in case of using a vacuum pressure	[59,102,117,138–140, 141]
	Fixed-bed adsorption distillation (FAD)	Molecular sieves or ion-exchange resins are used as separating agents. The molecular sieves alter the vapor-liquid equilibrium of the mixture's components.	• Environmentally friendly • No extra organic solution • No solvent loss	• Difficulty to regenerate the molecular sieves • Lower separation effect than the separating agent used in the extractive distillation	[118,123]
Membrane Processes	**Pervaporation (PV)**	It is a combination of two mechanisms: permeation and evaporation. Components of a liquid mixture permeate through a membrane and evaporate into the other side. It is useful in azeotropic separation, because it is based on the difference in sorption and diffusion of the components, not the relative volatility.	• Small footprint • Environmentally friendly • Simplicity and flexibility • Low energy consumption • Independent of relative volatility, so suitable for azeotrope separation • No additional impurities in the final product	• High capital cost • Relatively low permeate fluxes (i.e. large membrane areas) • Low condensation temperatures (i.e. high operating costs) • Need for integration with conventional separation units	[122–124,142]
	Vapor permeation (VP)	It is similar to the pervaporation, except that in vapor permeation the feed is a mixture of vapors or vapor and gas.	• Simple operation and control • Reliable performance and high flexibility	• Rather expensive • Relatively low permeate fluxes (i.e. large membrane areas)	[125,127]

Separation Processes		Description	Advantages	Drawbacks	Ref
			• High product purity (no contamination by entrainer) • Small footprint	• Low condensation temperatures (i.e. high operating costs) • Need for integration with conventional separation units	
	Membrane distillation (MD)	It is based on thermal gradient across a porous membrane that only passes the vapors. Nonvolatile components remain on the feed side; so there will be neither solid nor nonvolatile components in the product.	• Relatively low cost and low energy consumption • Large vapor-liquid interface area per unit volume compared with conventional distillation • Possible under mild operating conditions (i.e. not necessary to increase feed temperature to its boiling point.)	• Low permeate flux • Relatively small thermal efficiency in DCMD configuration	[120,121,143]
	Frictional diffusion (FricDiff)	It is based on differences in diffusive velocities of the feed components when diffusing through a sweep gas.	• Relatively low energy consumption and absence of hazardous solvents	• Need to avoid pressure drop across the porous barrier (it causes convective mass transfer and adversely affects the separation).	[106,126,128]

2.5 Humidification-dehumidification nozzle-demister

We are developing a new wastewater treatment technology which uses humidification-dehumidification in a subsonic swirling nozzle combined with an in-line demister to reclaim clean water from wastewater (US Patent Application 62882970). The method takes advantage of a widely-observed trend in water azeotropes as well as the thermodynamics of the humid streams to efficiently separate and selectively condense water vapor. The technology is largely insensitive of the composition of the feed wastewater. It can be containerized and mobilized from site to site with minimal mounting and dismounting time and expense. Supersonic swirling nozzle-demisting is used in the oil and gas industry to dehydrate natural gas after extraction [144]. By taking advantage of the same principles of operation, but at subsonic velocities, the nozzle-demister will treat hydraulic fracturing wastewater while utilizing technology that is already familiar to the oil and gas industry.

2.5.1 Azeotrope separation

The prevalent method of separation is to break an azeotrope by introducing a compound that forms a stronger azeotrope with one/some of the constituents, as previously discussed. However, this approach is not practical for hydraulic fracturing wastewater due to the vast variety of chemicals and azeotropes. The new treatment approach, which avoids this limitation, relies on two observations:

1. Hundreds of water azeotropes have been documented, and in a large majority of cases the saturation temperature deviates significantly from that of water (Figure 2.6). Our process will operate narrowly around the saturation point of water such that azeotropes with saturation temperatures that are different from that of water are separated from the treated water. This will be accomplished by heating the wastewater to nominally 1°C above the saturation temperature of water and then cooling the vapor to nominally 1°C below the saturation temperature, as discussed further below. If the process is controlled within ±1°C of water's saturation temperature, only 2.5% of azeotropes may remain; some of which have not been reported in hydraulic fracturing wastewater and some are innocuous, such as butyric acid-water.

2. Hydraulic fracturing wastewater is by-and-large made of dissolved solids and low-volatility compounds. Many of these contaminants are likely to be present in

concentrations which are orders of magnitude smaller than their respective azeotropic mixtures with water. As little as 2% of all contaminants may evaporate and even fewer form a water-based azeotrope. Furthermore, in that 2%, the mass ratio of water in the azeotrope is relatively small; in almost half of its azeotropes, water makes up less than 30% of the total mass. This means that the vast majority of water is not engaged in an azeotrope and is recoverable.

Figure 2.6 shows the saturation temperature of 280 common azeotropes versus the water ratio in each azeotrope. The saturation temperature of water is shown as a red line. In the new treatment, first the wastewater will be heated to 1°C above the saturation temperature of water. The waste vapor will contain all the azeotropes shown in the red box. The azeotropes in the white box will remain in the wastewater tank. Then, the vapor will be cooled to 1°C below the saturation temperature of water. Only the azeotropes in the narrow blue band will condense with the clean water. Thus, by carefully controlling the temperature of the process, 98% of potential azeotropes can be separated from the treated water.

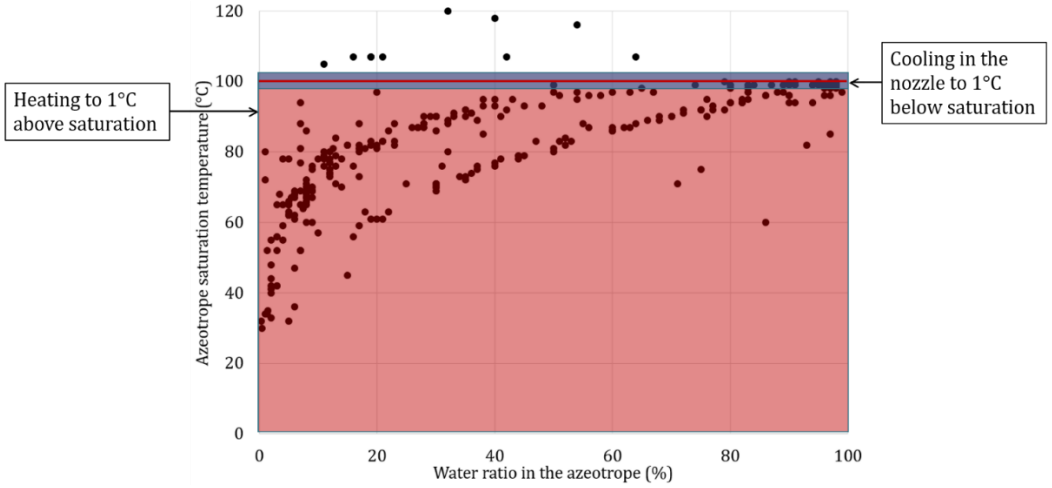

Figure 2.6: Saturation temperature vs. water mass ratio for 280 common binary and ternary water azeotropes, raw data extracted from [145,146].

2.5.2 Operation

The process schematic is shown in Figure 2.7. Dry air is drawn into the nozzle, shown as point 0 in Figure 2.7, and is heated via low-grade heat. Next, the fast-moving hot air comes into contact with a vortex generator (labeled as point 1) which swirls the incoming stream. Then, wastewater vapor enters the nozzle (point 2) and mixes with the air (point 3), the wastewater vapor is at a temperature 1°C above the saturation temperature of water. The humid air mixture, at point 3, continues

through the converging nozzle. As the velocity of the air increases due to the reduction in cross-sectional area, the temperature of the air will decrease as the thermal energy is converted to kinetic energy. As the temperature drops to the saturation point, clean water will condense out of the humid air. As the water condenses, the latent heat of condensation is released and rejected to a jacket heat exchanger with cold feed wastewater flowing over the nozzle. The jacket heat exchanger allows the temperature in the nozzle to be maintained at 1°C below the saturation temperature despite the latent heat of condensation being released. The flowrate of cold feed wastewater through the jacket heat exchanger can be adjusted in order to control the temperature. As the water condenses into suspended droplets, the flow becomes misty. The swirling motion pushes the droplets to the periphery of the nozzle where the clean water is collected by an in-line demister (point 5). The dry air and gaseous contaminants pass through the demister and flow through a diffuser to reduce the velocity and increase the temperature of the flow (points 7 & 8), thus allowing more energy to be recouped from the waste stream via heat exchangers. Both the clean water and contaminants flow through heat exchangers in the wastewater pool before collection (point 9). Heat is also added to the wastewater pool (point 13) to generate the waste vapor that is the feed stream entering the nozzle. All points and what they indicate in the nozzle-demister are shown in Table 2.4. Based on the energy consumption of the treatment our process is projected to treat hydraulic fracturing wastewater at a cost of $\$7/m^3$.

Component-level testing has proven the concept of the treatment system. The nozzle uses the Venturi effect to suck the wastewater vapor into the nozzle. Experimental-validated simulations have shown that the nozzle can achieve a suction ratio of air to steam ranging from 5 to 1 up to 1 to 1, which is ideal for the humidity in the nozzle before condensation. In-house experiments on azeotrope separation have shown that over 95% of the azeotropes can successfully be separated from the clean water. Additionally, the demister has been proven collect 99% of the clean water. Details of these results are outside the scope of this article and will be the subjects of upcoming publications.

The control of the system is critical to the quality of the resulting treated water. If the temperature in the nozzle is controlled within ±1°C, then only 2.5% of potential contaminants would remain in the treated water. Controlling the temperature within to that level of accuracy is complicated by the thermal mass and inertia as well as

variability in the fluid composition, thus making traditional control insufficient for this system. The temperature in the nozzle will be controlled using a digital twin. A physics-based model of the system will be paired with real-time experimental data to create a digital twin that will use machine learning to predict the performance of the nozzle, as well as the temperature. The predictions from the digital twin will then be used to adjust the operation of the system to maintain a temperature of 1°C above the saturation temperature of water.

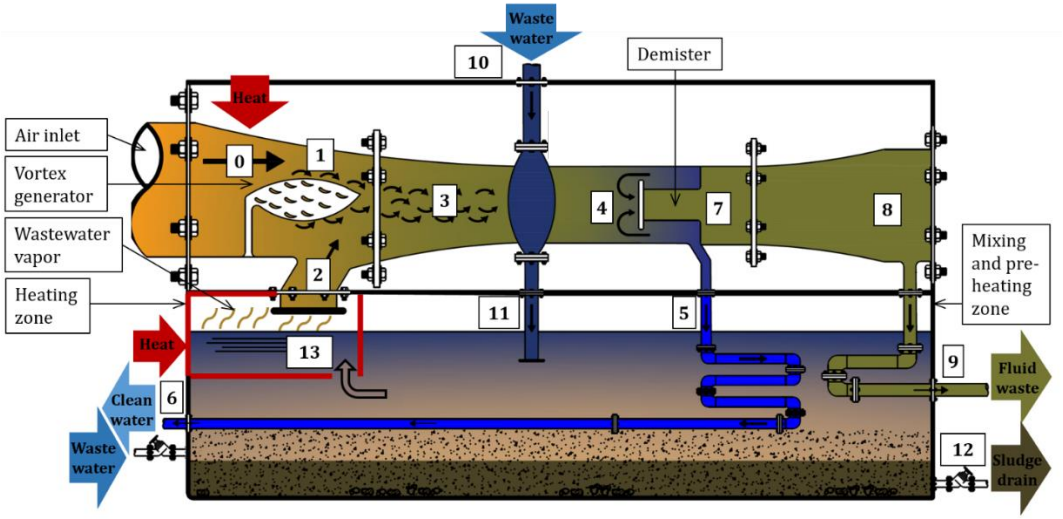

Figure 2.7: Schematic of the thermally-actuated nozzle-demister. Locations marked by numbers are explained in Table 2.4.

Table 2.4: Explanation of points marked in Figure 2.7

Point in Figure 2.7	**Location in Nozzle-Demister**
0	Air inlet to nozzle
1	Swirl generator
2	Waste steam inlet to nozzle
3	Converging section of nozzle
4	Inlet to in-line demister
5	Clean water separation from demister
6	Clean water outlet
7	Outlet of demister
8	Diverging section of nozzle
9	Fluid waste outlet
10	Wastewater inlet to jacket heat exchanger
11	Wastewater outlet from jacket heat exchanger to settling tank
12	Sludge outlet from settling tank
13	Heating zone

2.6 Conclusions

Although membrane-driven technologies have the advantage of filtering out suspended solids and volatiles, the TDS limits for membrane technologies are significantly lower than those of thermally-driven technologies. Additionally, vaporization has been suggested as the best way to treat wastewater. Of the thermally-driven technologies, membrane distillation is capable of dealing with the highest TDS levels; however, the use of a membrane in this process makes it susceptible to fouling. Additionally, few treatment processes are capable of removing azeotropes from the hydraulic fracturing wastewater. Membrane distillation is the main common treatment technology that separates azeotropes. A humidification-dehumidification nozzle-demister process that is not susceptible to fouling or clogging was described. This process has the advantage of high TDS limits and azeotrope separation. The next steps for the new design are fabrication and experimental validation. Component validation has been completed. Thermal-based processes show promise for treating the highly variable and toxic hydraulic fracturing wastewater, and a process that does not require pretreatment or fouling treatment would be ideal. Given the difficulties of hydraulic fracturing wastewater treatment, a hybrid or novel treatment system may be best suited as treatment methods.

Acknowledgements

This work is supported by the US Department of Energy, Advanced Research Projects Agency – Energy (ARPA-E) award number DE-0001000. Results of this work do not necessarily reflect the views of the Department of Energy. The intellectual property related to our thermally-actuated nozzle-demister process is protected under US patent application number is US62882970.

Nomenclature

TSS	Total suspended solids
TDS	Total dissolved solids
RO	Reverse osmosis
FO	Forward osmosis
MD	Membrane distillation
MFD	Multistage flash distillation
MED	Multi-effect distillation
MVC	Mechanical vapor compression
CCD	Closed circuit desalination
UF	Ultrafiltration
MF	Microfiltration
DES	Deep eutectic solvents

NMP	N-methyl-2-pyrrolidone
DCMD	Direct contact membrane distillation
AGMD	Air gap membrane distillation
SGMD	Sweeping gas membrane distillation
VMD	Vacuum membrane distillation
PVA	Poly vinyl alcohol
PES	Poly ether sulfone
AD	Azeotropic distillation
A-DWC	Azeotropic dividing wall column
ED	Extractive distillation
PSD	Pressure swing distillation
FAS	Fixed-bed adsorption distillation
PV	Pervaporation
VP	Vapor permeation

References

1. B.D. Lutz, A.N. Lewis, M.W. Doyle, Generation, transport, and disposal of wastewater associated with Marcellus Shale gas development, Water Resour. Res. 49 (2013) 647–656.

2. R.B. Jackson, A. Vengosh, J.W. Carey, R.J. Davies, T.H. Darrah, F.O. Sullivan, P. Gabrielle, The Environmental Costs and Benefits of Fracking, Annu. Rev. 39 (2014) 327–362.

3. J.M. Estrada, R. Bhamidimarri, A review of the issues and treatment options for wastewater from shale gas extraction by hydraulic fracturing, Fuel. 182 (2016) 292–303.

4. A.J. Kondash, N.E. Lauer, A. Vengosh, The intensification of the water footprint of hydraulic fracturing, Sci. Adv. 4 (2018).

5. O. Olsson, D. Weichgrebe, K.H. Rosenwinkel, Hydraulic fracturing wastewater in Germany: Composition, treatment, concerns, Environ. Earth Sci. 70 (2013) 3895–3906.

6. D.L. Shaffer, L.H. Arias Chavez, M. Ben-Sasson, S. Romero-Vargas Castrillón, N.Y. Yip, M. Elimelech, Desalination and reuse of high-salinity shale gas produced water: Drivers, technologies, and future directions, Environ. Sci. Technol. 47 (2013) 9569–9583.

7. D.S. Alessi, A. Zolfaghari, S. Kletke, J. Gehman, D.M. Allen, G.G. Goss, Comparative analysis of hydraulic fracturing wastewater practices in unconventional shale development: Water sourcing, treatment and disposal practices, Can. Water Resour. J. 42 (2017) 105–121.

8. US Energy Information Administration, Annual Energy Outlook, Washington, D.C. (2017).

9. G.A. Gagnon, W. Krkosek, L. Anderson, E. McBean, M. Mohseni, M. Bazri, I. Mauro, Impacts of hydraulic fracturing on water quality, a review of literature, regulatory frameworks and an analysis of information gaps, Environ. Rev. 24 (2015) 122–131.

10. T.L.S. Silva, S. Morales-Torres, S. Castro-Silva, J.L. Figueiredo, A.M.T. Silva, An overview on exploration and environmental impact of unconventional gas sources and treatment options for produced water, J. Environ. Manage. 200 (2017) 511–529.

11. A. Kondash, A. Vengosh, Water Footprint of Hydraulic Fracturing, Environ. Sci. Technol. Lett. 2 (2015) 276–280.

12. C. Notte, D.M. Allen, J. Gehman, D.S. Alessi, G.G. Goss, Comparative analysis of hydraulic fracturing wastewater practices in unconventional shale developments: Regulatory regimes, Can. Water Resour. J. 42 (2017) 122–137.

13. The Distribution of U.S. Oil and Natural Gas Wells by Production Rate, Washington, D.C., 2019.

14. J.E. Johnston, E. Werder, D. Sebastian, Wastewater disposal wells, fracking, and environmental injustice in Southern Texas, Am. J. Public Health. 106 (2016) 1–7.

15. M.P.J.A. Annevelink, J.A.J. Meesters, A.. Hendricks, Environmental contaminantion due to shale gas development, Sci. Total Environ. 48 (2016) 431–438.

16. I. Ferrer, E.M. Thurman, Chemical constituents and analytical approaches for hydraulic fracturing waters, Trends Environ. Anal. Chem. 5 (2015) 18–25.

17. Y. Sun, D. Wang, D. Tsang, L. Wang, Y.S. Ok, Y. Feng, A critical review of risks, characteristics, and treatment strategies for potentially toxic elements in wastewater from shale gas extraction, Environ. Int. 125 (2019) 452–469.

18. FracFocus – National Hydraulic Fracturing Chemical Disclosure Registry, Ground Water Protection Council, Oklahoma City, OK. https://www.fracfocus.org/ (2019).

19. W.T. Stringfellow, M. Kay, J.K. Domen, W.L. Sandelin, C. Varadharajan, P.D. Jordan, M.T. Reagan, H. Cooley, M.G. Heberger, J.T. Birkholzer, Identifying

chemicals of concern in hydraulic fracturing fl uids used for oil production, Environ. Pollut. 220 (2017) 413–420.

20. G.A. Kahrilas, J. Blotevogel, E.R. Corrin, T. Borch, Downhole Transformation of the Hydraulic Fracturing Fluid Biocide Glutaraldehyde: Implications for Flowback and Produced Water Quality, Environ. Sci. Technol. 50 (2016) 11414–11423.

21. J.J. Marrugo-hernandez, R. Prinsloo, J. Fischer, R.A. Marriott, Downhole chemical degradation of corrosion inhibitors commonly used in shale gas fracturing and stimulation, Environ. Sci. Technol. 50 (2016) 11414–11423.

22. F.-R. Ahmadun, A. Pendashteh, L. Chuah Abdullah, D. Radiah Awang Biak, S. Siavash Madaeni, Z. Zainal Abidin, Review of technologies for oil and gas produced water treatment, J. Hazard. Mater. 170 (2009) 530–551.

23. L.G. Faksness, P.G. Grini, P.S. Daling, Partitioning of semi-soluble organic compounds between the water phase and oil droplets in produced water, Mar. Pollut. Bull. 48 (2004) 731–742.

24. EPA, Comparison of hydraulic fracturing fluids composition with produced formation water following fracturing - implications for fate and transport, Hydraulic Fracturing Technical Workshop 3 - Contaminant Identification, Transformation & Transport, Environmental Protection Agency, United States, 2016.

25. K.B. Gregory, R.D. Vidic, D.A. Dzombak, Water management challenges associated with the production of shale gas by hydraulic fracturing, Elements. 7 (2011) 181–186.

26. J. Broderick, K. Anderson, R. Wood, P. Gilbert, M. Sharmina, A. Footitt, S. Glynn, F. Nicholls, Shale gas: an updated assessment of environmental and climate change impacts. A report commissions by the Co-operative and undertaken by researchers at the Tyndall Centre, University of Manchester, Manchester, UK, 2011.

27. E. Barbot, N.S. Vidic, K.B. Gregory, R.D. Vidic, Spatial and temporal correlation of water quality parameters of produced waters from Devonian-age shale following hydraulic fracturing, Environ. Sci. Technol. 47 (2013) 2562–2569.

28. B.G. Rahm, J.T. Bates, L.R. Bertoia, A.E. Galford, D.A. Yoxtheimer, S.J. Riha, Wastewater management and Marcellus Shale gas development: Trends, drivers, and planning implications, J. Environ. Manage. 120 (2013) 105–113.

29. A. Vengosh, R.B. Jackson, N. Warner, T.H. Darrah, A. Kondash, A critical review of the risks to water resources from unconventional shale gas development and hydraulic fracturing in the United States, Environ. Sci. Technol. 48 (2014) 8334–8348.

30. T. Zhang, K. Gregory, R.W. Hammack, R.D. Vidic, Co-precipitation of Radium with Barium and Strontium Sulfate and Its Impact on the Fate of Radium during Treatment of Produced Water from Unconventional Gas Extraction, Environ. Sci. Technol. 48 (2014) 4596–4603.

31. O. Lokare, S. Tavakkoli, S. Wadekar, V. Khanna, R.D. Vidic, Fouling in direct contact membrane distillation of produced water from unconventional gas extraction, J. Memb. Sci. 524 (2017) 493–501.

32. E.C. Chapman, R.C. Capo, B.W. Stewart, C.S. Kirby, R.W. Hammack, K.T. Schroeder, H.M. Edenborn, Geochemical and Strontium Isotope Characterization of Produced Waters from Marcellus Shale Natural Gas Extraction, Environ. Sci. Technol. 46 (2012) 3545–3553.

33. T.D. Hayes, B.F. Severin, Characterization of flowback waters from the Marcellus and Barnett shale regions, in: Barnett Appalach. Shale Water Manag. Reuse Technol. RPSEA, Houston, TX. 2012.

34. J.L. Luek, M. Gonsior, Organic compounds in hydraulic fracturing fluids and wastewaters: A review, Water Res. 123 (2017) 536–548.

35. S.J. Maguire-boyle, A.R. Barron, Organic compounds in producced waters from shale gas wells, Environ. Sci. Process Impacts. 16 (2014) 22372248.

36. D.M. Akob, I.M. Cozzarelli, D.S. Dunlap, E.L. Rowan, M.M. Lorah, Organic and inorganic composition and microbiology of produced waters from Pennsylvania shale gas wells, Appl. Geochemistry. 60 (2015) 116–125.

37. E.G. Elliott, A.S. Ettinger, B.P. Leaderer, M.B. Bracken, N.C. Deziel, A systematic evaluation of chemicals in hydraulic-fracturing fl uids and wastewater for reproductive and developmental toxicity, J. Od Expo. Sci. Evironmental Epidemiol. 27 (2017) 90–99.

38. M.S. Gay, S. Oliver, S. Fletcher, N. Meyer, S. Gross, Water management in shale gas plays, IHS Walter White Pap., Indian Health Service, Rockville, MD. (2012).

39. P. Boschee, Produced and flowback water recycling and reuse, Oil Gas Facil. 3 (2014) 16–21.

40. Q. Jiang, J. Rentschler, R. Perrone, K. Liu, Application of ceramic membrane and ion-exchange for the treatment of the flowback water from Marcellus shale gas production, J. Memb. Sci. 431 (2013) 55–61.

41. B.A. Beckman, A. Ambulkar, A. Umble, D. Rosso, J. Husband, J. Cleary, J. Sandino, M. Goldblatt, R. Horres, R. Neufeld, R. Mau, S. Jeynayagam, Considerations for Accepting Fracking Wastewater at Water Resource Recovery Facilities, Water Environ. Fed., Alexandria, VA. (2014) 1–4.

42. C.E. Clark, J.A. Veil, Produced Water Volumes and Management Practices in the United States, Technical Report, US Department of Energy, Department of Scientific and Technical Information. Washington D.C. (2009).

43. EPA, Underground Injection Control (UIC), US Environ. Prot. Agency., Washington D.C. (2019).

44. Hydraulic Fracturing Study Technical Workshop #4 Water Resources Management, Environmental Protection Agency, Washington D.C. (2011).

45. M. Schantz, Produced and flowback water treatment from fracking, in: Unconv. Oil Gas Symp., Oil & Gas Journal, Lexington, KY., 2014.

46. S. Entrekin, M. Evans-White, B. Johnson, E. Hagenbuch, Rapid expansion of natural gas development poses a threat to surface waters, Front. Ecol. Environ. 9 (2011) 503–511.

47. W.L. Ellsworth, Injection-Induced Earthquakes, Science (80-.). 341 (2013) 1–8.

48. M. Weingarten, S. Ge, J.W. Godt, B.A. Bekins, J.L. Rubinstein, High-rate injection is associated with the increase in U.S. mid-continent seismicity, Science (80-.). 348 (2015) 1336–1340.

49. M.C. Ryan, D. Alessi, A.B. Mahani, A. Cahill, J. Cherry, D. Eaton, R. Evans, N. Farah, A. Fernandes, O. Forde, P. Humez, S. Kletke, B. Ladd, J. Lemieux, B. Mayer, K.U. Mayer, J. Molson, L. Muehlenbachs, A. Nowamooz, B. Parker, Subsurface Impacts of Hydraulic Fracturing : Contamination, Seismic Sensitivity, and Groundwater Use and Demand Management, Can. Water Netw. Waterloo, ON. (2015) 138.

50. S. Horton, Disposal of hydrofracking waste fluid by injection into subsurface aquifers triggers earthquake swarm in central Arkansas with potential for damaging earthquake, Seismol. Res. Lett. 83 (2012) 250–260.

51. J.L. Rubinstein, A.B. Mahani, Myths and Facts on Wastewater Injection , Hydraulic Fracturing , Enhanced Oil Recovery , and Induced Seismicity, Seasmological Soc. Am. 86 (2015) 1060–1067.

52. R.D. Vidic, S.L. Brantley, J.M. Vandenbossche, D. Yoxtheimer, J.D. Abad, Impact of shale gas development on regional water quality, Science (80-.). 340 (2013).

53. K. Ferrar, D. Michanowicz, C. Christen, N. Mulcahy, S. Malone, R. Sharma, Assessment of Effluent Contaminants from Three Facilities Discharging Marcellus Shale Wastewater to Surface Waters in Pennsylvania, Environ. Sci. Technol. 47 (2013) 3472–3481.

54. N. Warner, C. Christie, R.B. Jackson, A. Vengosh, Impacts of Shale Gas Wastewater Disposal on Water Quality in Western Pennsylvania, Environ. Sci. Technol. 47 (2013) 11849–11857.

55. N. Warner, Environmental and Human Health Impacts of Spreading Oil and Gas Wastewater on Roads, Environ. Sci. Technol. 52 (2018) 7081–7091.

56. EPA, Guidelines for Water Reuse, Washington D.C. (2012).

57. S. Ahmadvand, B. Abbasi, B. Azarfar, M. Elhashimi, Looking Beyond Energy Efficiency: An Applied Review of Water Desalination Technologies and an Introduction to Capillary-Driven Desalination, Water. 11 (2019) 696.

58. Y. Wang, H. Zhang, X. Yang, Y. Shen, Z. Chen, P. Cui, L. Wang, F. Meng, Y. Ma, J. Gao, Insight into separation of azeotrope in wastewater to achieve cleaner production by extractive distillation and pressure-swing distillation based on phase equilibrium, J. Clean. Prod. 276 (2020) 124213.

59. Y. Cui, X. Shi, C. Guang, Z. Zhang, C. Wang, C. Wang, Comparison of pressure-swing distillation and heterogeneous azeotropic distillation for recovering benzene and isopropanol from wastewater, Process Saf. Environ. Prot. 122 (2019) 1–12.

60. A. Achilli, T.Y. Cath, E.A. Marchand, A.E. Childress, The forward osmosis membrane bioreactor: A low fouling alternative to MBR processes, Desalination. 239 (2009) 10–21.

61. R. Holloway, A.E. Childress, K. Dennett, T.Y. Cath, Forward osmosis for concentration of anaerobic digester centrate, Water Res. 41 (2007) 4005–4014.

62. A. Sagiv, N. Avraham, C. Dosoretz, R. Semiat, Osmotic backwash mechanism of reverse osmosis membranes, J. Memb. Sci. 322 (2008) 225–233.

63. A. Sagiv, R. Semiat, Parameters affecting backwash variables of RO membranes, Desalination. 261 (2010) 347–353.

64. H. Chang, T. Li, B. Liu, C. Chen, Q. He, J.C. Crittenden, Smart ultrafiltration membrane fouling control as desalination pretreatment of shale gas fracturing wastewater: The effects of backwash water, Environ. Int. 130 (2019) 104869.

65. H. Chang, T. Li, B. Liu, R.D. Vidic, M. Elimelech, J.C. Crittenden, Potential and implemented membrane-based technologies for the treatment and reuse of flowback and produced water from shale gas and oil plays : A review, Desalination. 455 (2019) 34–57.

66. K.L. Hickenbottom, N.T. Hancock, N.R. Hutchings, E.W. Appleton, E.G. Beaudry, P. Xu, T.Y. Cath, Forward osmosis treatment of drilling mud and fracturing wastewater from oil and gas operations, Desalination. 312 (2013) 60–66.

67. C.S. Ong, B. Al-anzi, W.J. Lau, P.S. Goh, G.S. Lai, Anti-Fouling Double-Skinned Forward Osmosis Membrane with Zwitterionic Brush for Oily Wastewater Treatment, Sci. Rep. 7 (2017) 1–11.

68. S.J. Maguire-boyle, E.H. Joseph, T.J. Ainscough, D.L. Oatley-, A.A. Alabdulkarem, S.F. Al-mojil, A.R. Barron, Superhydrophilic Functionalization of Microfiltration Ceramic Membranes Enables Separation of Hydrocarbons from Frac and Produced Water, Sci. Rep. 7 (2017) 12267.

69. H.R. Acharya, C. Henderson, H. Wang, Cost Effective Recovery of Low-TDS Frac Flowback Water for Re-use, U.S. Department of Energy, Washington, D.C., 2011.

70. R. Bouchrit, A. Boubakri, A. Hafiane, S.A.-T. Bouguecha, Direct contact membrane distillation; capability to treat hyper-saline solution, Desalination. 376 (2015) 117–129.

71. A. Efraty, R.N. Barak, Z. Gal, Closed circuit desalination - a new low energy high recovery technology without energy recovery, Desalin. Water Treat. 31 (2011) 95–101.

72. S.M. Riley, D.C. Ahoor, K. Oetjen, T.Y. Cath, Closed circuit desalination of O & G produced water : An evaluation of NF / RO performance and integrity, Desalination. 442 (2018) 51–61.

73. T.V. Bartholomew, L. Mey, J.T. Arena, N.S. Siefert, M.S. Mauter, Osmostically assisted reverse osmosis for high salinity bring treatment, Desalination. 421 (2017) 3–11.

74. B.D. Coday, P. Xu, E.G. Beaudry, J. Herron, K. Lampi, N.T. Hancock, T.Y. Cath, The sweet spot of forward osmosis: Treatment of produced water, drilling wastewater, and other complex and difficult liquid streams, Desalination. 333 (2014) 23–35.

75. L. Chekli, S. Phuntsho, J. Eun, J. Kim, J. Young, J. Choi, S. Kim, J. Ha, S. Hong, J. Sohn, H.K. Shon, Engineering advance A comprehensive review of hybrid forward osmosis systems: Performance, applications and future prospects, J. Memb. Sci. 497 (2016) 430–449.

76. R.L. Mcginnis, N.T. Hancock, M.S. Nowosielski-Slepowron, Pilot demonstration of the NH3/CO2 forward osmosis desalination process on high salinity brines, Desalination. 312 (2013) 67–74.

77. X. Li, B. Zhao, Z. Wang, M. Xie, J. Song, L. Nghiem, T. He, C. Yang, C. Li, G. Chen, Water reclamation from shale gas drilling flow-back fluid using a novel forward osmosis-vacuum membrane distillation hybrid system, Water Sci. Technol. 69 (2014) 1036–1044.

78. T.Y. Cath, N.T. Hancock, C.D. Lundin, C. Hoppe-jones, J.E. Drewes, A multi-barrier osmotic dilution process for simultaneous desalination and purification of impaired water, J. Memb. Sci. 362 (2010) 417–426.

79. N.T. Hancock, N.D. Black, T.Y. Cath, A comparative life cycle assessment of hybrid osmotic dilution desalination and established seawater desalination and wastewater reclamation processes, Water Res. 46 (2011) 1145–1154.

80. HTI, Oil Wastewater Treatment & Gas Wastewater Treatment: Lead Story, Hydration Technology Innovations, Albany, OR. (2011).

81. K. Lawson, D. Lloyd, Membrane Distillation, J. Memb. Sci. 124 (1997) 1–25.

82. L.D. Tijing, Y. Chul, J. Choi, S. Lee, S. Kim, H. Kyong, Fouling and its control in membrane distillation — A review, J. Memb. Sci. 475 (2015) 215–244.

83. V. Calabro, E. Drioli, F. Matera, Membrane distillation in the textile wastewater treatment, Desalination. 83 (1991) 209–224.

84. Y. Wu, Y. Kong, J. Liu, J. Zhang, J. Xu, An experimental study on membrane distillation: Crystallization for treating waste water in taurine production, Desalination. 80 (1991) 235–224.

85. P.P. Zolotarev, V.V. Ugrozov, I. Volkina, V. Nikulin, Treatment of waste water for removing heavy metals by membrane distillation, J. Hazard. Mater. 78 (1994) 77–82.

86. M. Tomaszewska, Concentration of the extraction fluid from sulfuric acid treatment of phosphogypsum by membrane distillation, J. Memb. Sci. 78 (1993) 277–282.

87. E. Jang, S. Jeong, E. Chung, Application of three different water treatment technologies to shale gas produced water, Geosystem Eng. 20 (2017) 104–110.

88. Z. Zhang, X. Du, K. Carlson, C. Robbins, T. Tong, Effective treatment of shale oil and gas produced water by membrane distillation coupled with precipitative softening and walnut shell filtration, Desalination. 454 (2019) 82–90.

89. M. Mulder, Basic Principles of Membrane Technologies, Kluwer Academic Publishers, New York, NY. 1996.

90. F.-X. Kong, Z.-P. Wang, Z. Ji, J.-F. Chen, C.-M. Guo, G.-D. Sun, Y.F. Xie, Organic fouling of membrane distillation for shale gas fracturing flowback water desalination: a special interest in the feed properties by pretreatment, Environ. Sci. Water Res. Technol. 5 (2019) 1339–1348.

91. A. Carrero-parren, V.C. Onishi, R. Salcedo-d, E.S. Fraga, J.A. Caballero, J.A. Reyes-labarta, Optimal Pretreatment System of Flowback Water from Shale Gas Production, Ind. Eng. Chem. Res. 56 (2017) 4386–4398.

92. P. Tang, B. Liu, Y. Zhang, H. Chang, P. Zhou, M. Feng, Sustainable reuse of shale gas wastewater by pre-ozonation with ultra filtration-reverse osmosis, Chem. Eng. J. 392 (2020) 123743.

93. T. Sirivedhin, J. McCue, L. Dallbauman, Reclaiming produced water for benficial use: salt removal by electrodialysis, J. Memb. Sci. 243 (2004) 335–343.

94. M.E. Blauch, R.R. Myers, T. Moore, B.A. Lipinski, N.A. Houston, Marcellus shale post-frac flowback waters - where is all the salt coming from and what are its implications?, SPE East. Reg. Meet. (2009).

95. Y.R. Glazer, J.B. Kjellsson, K.T. Sanders, M.E. Webber, Potential for Using Energy from Flared Gas for On-Site Hydraulic Fracturing Wastewater Treatment in Texas, Environ. Sci. Technol. Lett. 1 (2014) 300–304.

96. R. Bahar, M.N.A. Hawlader, L.S. Woei, Performance evaluation of a mechanical vapor compression desalination system, Desalination. 166 (2004) 123–127.

97. H. Aybar, Analysis of a mechanical vapor compression desalination system, Desalination. 142 (2002) 181–186.

98. M. Al-Shammiri, M. Safar, Multi-effect distillation plants: state of the art, Desalination. 126 (1999) 45–59.

99. G. Raluy, L. Serra, J. Uche, Life cycle assessment of MSF, MED and RO desalination technologies, Energy. 31 (2006) 2361–2372.

100. A. Ophir, F. Lokiec, Advanced MED process for most economical sea water desalination, Desalination. 182 (2005) 187–198.

101. D. Zhao, J. Xue, S. Li, H. Sun, Q. Zhang, Theoretical analyses of thermal and economical aspects of multi-effect distillation desalination dealing with high salinity wastewater, Desalination. 273 (2011) 292–298.

102. W.L. Luyben, Pressure-Swing Distillation for Minimum- and Maximum-Boiling Homogeneous Azeotropes, Ind. Eng. Chem. Res. 51 (2012) 1–6.

103. J. Pla-Franco, E. Lladosa, S. Loras, J.B. Montón, Azeotropic distillation for 1-propanol dehydration with diisopropyl ether as entrainer: Equilibrium data and process simulation, Sep. Purif. Technol. 212 (2019) 692–698.

104. I.L. Chien, B.Y. Yu, Z.J. Ai, R. Elyas, C.L. Chen, Design of Azeotropic Distillation Systems, Chem. Eng. Process Simul. 355, Elsevier, Amsterdam, NL. (2017).

105. A.A. Kiss, Distillation | Extractive Distillation, Ref. Modul. Chem. Mol. Sci. Chem. Eng. Elsevier, Amsterdam, NL. (2013) 0–24.

106. A. Selvi, L. Schoon, P. Jansens, A. Bardow, Purity versus recovery in FricDiff separations for feed-side and sweep-side products, Sep. Purif. Technol. 76 (2010) 95–103.

107. V. Gomis, R. Pedraza, M.D. Saquete, A. Font, J. García-cano, Ethanol dehydration via azeotropic distillation with gasoline fraction mixtures as entrainers: A pilot-scale study with industrially produced bioethanol and naphta, Fuel Process. Technol. 140 (2015) 198–204.

108. P. Shi, Y. Gao, J. Wu, D. Xu, J. Gao, X. Ma, Y. Wang, Separation of azeotrope (2,2,3,3-tetrafluoro-1-propanol + water): Isobaric vapour-liquid phase equilibrium measurements and azeotropic distillation, J. Chem. Thermodyn. 115 (2017) 19–26.

109. J. Li, Z. Lei, Z. Ding, C. Li, B. Chen, Azeotropic distillation: A review of mathematical models, Sep. Purif. Rev. 34 (2005) 87–129.

110. Y. Ma, P. Cui, Y. Wang, Z. Zhu, Y. Wang, J. Gao, A review of extractive distillation from an azeotropic phenomenon for dynamic control, Chinese J. Chem. Eng. 27 (2019) 1510–1522.

111. Z. Lei, C. Li, B. Chen, Extractive Distillation: A Review, Sep. Purif. Rev. 32 (2003) 121–213.

112. Y. Peng, X. Lu, B. Liu, J. Zhu, Separation of azeotropic mixtures (ethanol and water) enhanced by deep eutectic solvents, Fluid Phase Equilib. 448 (2017) 128–134.

113. Y.H. Wang, I.L. Chien, Unique Design Considerations for Maximum-Boiling Azeotropic Systems via Extractive Distillation: Acetone/Chloroform Separation, Ind. Eng. Chem. Res. 57 (2018) 12884–12894.

114. W.L. Luyben, I.L. Chien, Design and control of distillation systems for separating azeotropes, John Wiley & Sons, Hoboken, NJ. 2011.

115. M. Skiborowski, A. Harwardt, W. Marquart, Conceptual design of azeotropic distillation processes, in: Distillation, Academic Press, Cambridge, MA. 2014: pp. 305–355.

116. W.L. Luyben, Methanol/trimethoxysilane azeotrope separation using pressure-swing distillation, Ind. Eng. Chem. Res. 53 (2014) 5590–5597.

117. S. Liang, Y. Cao, X. Liu, X. Li, Y. Zhao, Y. Wang, Y. Wang, Insight into pressure-swing distillation from azeotropic phenomenon to dynamic control, Chem. Eng. Res. Des. 117 (2016) 318–335.

118. Z. Lei, B. Chen, Z. Ding, Adsorption Dsitillation, in: Spec. Distill. Process., Elsevier, Amsterdam, NL. 2005.

119. S. Kalla, S. Upadhyaya, K. Singh, R. Baghel, Development of heat and mass transfer correlations and recovery calculation for HCl–water azeotropic separation using air gap membrane distillation, Chem. Pap. 73 (2019) 2449–2460.

120. H. Li, C. Guo, H. Guo, C. Yu, X. Li, X. Gao, Methodology for design of vapor permeation membrane-assisted distillation processes for aqueous azeotrope dehydration, J. Memb. Sci. 579 (2019) 318–328.

121. Z. Lei, B. Chen, Z. Ding, Membrane Distillation, in: Spec. Distill. Process., Elsevier, Amsterdam, NL. 2005.

122. N.G. Kanse, S.D. Dawande, B.D. Prashant, Effect of Feed Temperature and Solution Concentration on Pervaporation for separation of Azeotrpoic Mixtures, Mater. Today Proc. 5 (2018) 3541–3550.

123. J.P.G. Villaluenga, A review on the separation of benzene / cyclohexane mixtures by pervaporation processes, J. Memb. Sci. 169 (2000) 159–174.

124. Y.K. Ong, G. Min, N. Lieu, Y. Pan, J. Zuo, S.P. Nunes, T. Chung, Recent membrane development for pervaporation processes, Prog. Polym. Sci. 57 (2016) 1–31.

125. W. Kujawski, Application of Pervaporation and Vapor Permeation in Environmental Protection, Polish J. Environ. Stud. 9 (2000) 13–26.

126. B. Breure, E.A.J.F. Peters, P.J.A.M. Kerkhof, Separation of azeotropic mixtures of alcohols and water with FricDiff, Sep. Purif. Technol. 62 (2008) 349–362.

127. P. Číhal, O. Vopička, T. Durďáková, P.M. Budd, W. Harrison, K. Friess, Pervaporation and vapour permeation of methanol – dimethyl carbonate mixtures through PIM-1 membranes, Sep. Purif. Technol. 217 (2019) 206–214.

128. M. Geboers, P. Kerkhof, P. Lipman, F. Peters, FricDiff : A novel separation concept, Sep. Purif. Technol. 56 (2007) 47–52.

129. W. Arlt, Azeotropic distillation, in: Distillation, Academic Press, Cambridger, MA., 2014: pp. 247–259.

130. H.R. Mortaheb, H. Kosuge, Simulation and optimization of heterogeneous azeotropic distillation process with a rate-based model, Chem. Eng. Process. Process Intensif. 43 (2004) 317–326.

131. Y.C. Wu, H.Y. Lee, H.P. Huang, I.L. Chien, Energy-saving dividing-wall column design and control for heterogeneous azeotropic distillation systems, Ind. Eng. Chem. Res. 53 (2014) 1537–1552.

132. M. Aurangzeb, A.K. Jana, Double-partitioned dividing wall column for a multicomponent azeotropic system, Sep. Purif. Technol. 219 (2019) 33–46.

133. M. Seiler, D. Kohler, W. Arlt, Hyperbranched polymers: new selective solvents for extractive distillation and solvent extraction, Sep. Purif. Technol. 29 (2002) 245–263.

134. B. Chen, Z. Lei, Q. Li, C. Li, Application of CAMD in Separating Hydrocarbons by Extractive Distillation, AIChE J. 51 (2005) 3114–3121.

135. K.G. Joback, Computer Aided Molecular Design (CAMD): Designing Better Chemical Products, Molecular Knowledge Systems Inc., Bedford, NH.

136. V. Gerbaud, I. Rodriguez-donis, L. Hegely, P. Lang, F. Denes, X. You, Review of extractive distillation. Process design, operation, optimization and control, Chem. Eng. Res. Des. 141 (2018) 229–271.

137. S. Sun, L. Lü, A. Yang, S. Wei, W. Shen, Extractive distillation: Advances in conceptual design, solvent selection, and separation strategies, Chinese J. Chem. Eng. 27 (2019) 1247–1256.

138. Q. Zhang, M. Liu, W. Li, C. Li, A. Zeng, Heat-integrated triple-column pressure-swing distillation process with multi-recycle streams for the separation of ternary azeotropic mixture of acetonitrile / methanol / benzene, Sep. Purif. Technol. 211 (2019) 40–53.

139. J.P. Knapp, M.F. Doherty, A New Pressure-Swing-Distillation Process for Separating Homogeneous Azeotropic Mixtures, Ind. Eng. Chem. Res. (1992) 346–357.

140. J. Bonet, M. Galan, J. Costa, R. Thery, X. Meyer, M. Meyer, J. Reneaume, Pressure optimisation of an original system of pressure swing with a reactive column, Institution of Chemical Engineers Symposium Series 152., Rugby, Warwickshire, (2006) 344–352.

141. M. Skiborowski, A. Harwardt, W. Marquardt, Chapter 8 - Conceptual Design of Azeotropic Distillation Processes, Elsevier Inc., Amsterdam, NL. 2014.

142. Y.T. Ong, K.F. Yee, Y.K. Cheng, S.H. Tan, A review on the use and stability of supported liquid membranes in the pervaporation process, Sep. Purif. Rev. 43 (2014) 62–88.

143. E. Drioli, A. Ali, F. Macedonio, Membrane distillation: Recent developments and perspectives, Desalination. 356 (2015) 56–84.

144. A. Karimi, M.A. Abdi, Selective dehydration of high-pressure natural gas using supersonic nozzles, Chem. Eng. Process. Process Intensif. 48 (2009) 560–568.

145. W. Haynes, CRC Handbook of Chemistry and Physics, CRC Press, Boca Raton, FL. 2015.

146. J. Speight, Lange's Handbook of Chemistry, McGraw-Hill, New York, NY. 2005.

CHAPTER THREE

A Design Method for Low-Pressure Venturi Nozzles

Hannah O'Hern, Timothy Murphy, Xiang Zhang, James Liburdy, Bahman Abbasi*

School of Mechanical, Industrial, and Manufacturing Engineering, Oregon State University, Corvallis, OR 97331, USA,
* Corresponding author

Applied Mechanics
Volume 3, Issue 2, 2022, 390 – 411
https://doi.org/10.3390/applmech3020024

A Design Method for Low-Pressure Venturi Nozzles

Abstract

The purpose of this work is to provide empirical design models for low-pressure, subsonic Venturi nozzles. Experimentally validated simulations were used to determine the effect of nozzle geometry and operating conditions on the suction ratio (ratio of suction mass flow rate to motive mass flow rate) of low-pressure, subsonic Venturi nozzles, over a wide range of geometries and operating conditions, through a parametric study. The results of the parametric study were used to develop seven empirical models, each with a different range of applicability or calculating a different indicator of nozzle performance (i.e., suction ratio, momentum ratio, or dynamic pressure ratio), of the Venturi nozzles using a constrained multi-variable global optimization method. Of the seven empirical models, the best models were found to be those for low- (less than one) and high-suction ratios (greater than one), with mean absolute percentage errors of 5% and 18%, respectively. These empirical models provide a design tool for subsonic, low-pressure Venturi nozzles that is more than an order of magnitude more accurate than a governing equation approach or conventional flow head calculations. These newly-developed empirical models can be applied for initial nozzle design when precise suction ratios are required.

3.1 Introduction

Venturi nozzles use a fast-moving motive fluid stream to entrain a nearly quiescent suction fluid (Figure 3.1). In a Venturi nozzle, the motive stream is accelerated by flowing through a converging section, with the highest velocity achieved at the throat of the nozzle. The high velocity of the motive fluid creates a region of low static pressure and therefore a pressure difference between the motive fluid at the throat of the nozzle and the suction fluid. The pressure difference draws the suction flow into the nozzle, where the suction and motive streams mix before leaving the nozzle outlet. Thermal ejectors can be used to achieve the same suction and mixing but have a few more internal parts and are typically in the supersonic regime.

Venturi nozzles and ejectors are used in many industries due to their energy efficiency and lack of moving parts [1,2]. The use of such nozzles allows for two streams to mix while only using a compressor to move one of the streams, thus reducing the necessary energy input to operate a system. Venturi mixing nozzles

are used in irrigation and fertilization both to spread water and to mix fertilizers and other chemicals into the water using the Venturi effect [3,4]. The concentration of dissolved oxygen in water has also been increased utilizing high-pressure Venturi nozzles [5]. High-pressure or supersonic Venturi nozzles are also utilized in refrigeration and chiller applications [6–9]. Variable geometry nozzles have been studied for the application of variable load cooling, where the geometry of the nozzle can be changed as the cooling demand changes [10–12]. Bio-gas injection studies have also utilized Venturi nozzles to enhance mixing [13]. Venturi nozzles can also be used for vacuum generation in industrial applications such as vacuum-assisted brakes, powder ejection, the development of end-of-arm tools for robotic applications, and aerospace applications [14–16].

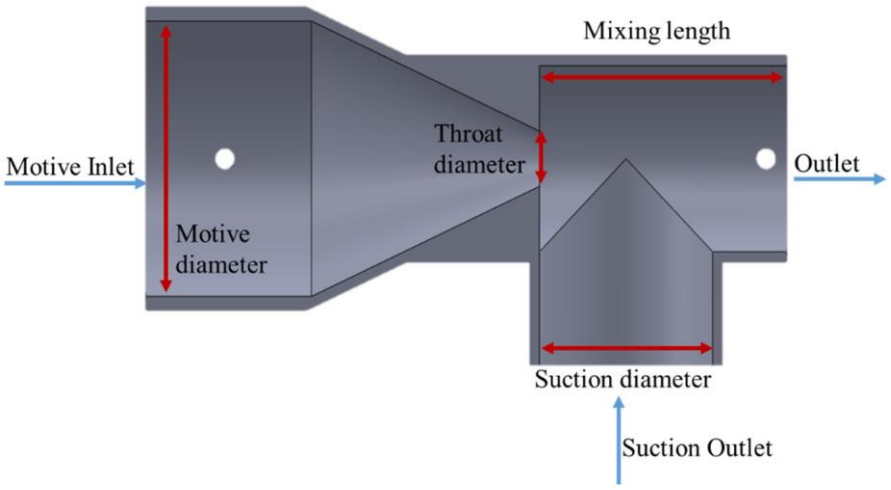

Figure 3.1: Cross-section of representative nozzle with key geometric parameters identified.

Due to their widespread use, the performance and operation of these supersonic ejectors and high-pressure Venturi nozzles have been studied extensively. In particular, steam ejector geometry has been thoroughly studied from a first-principles basis, as waste steam from industrial processes may be made usable again once entrained in the nozzle [17–20]. Steam ejectors have been studied utilizing CFD methods as well as experimental methods [21–23].

There has been significant effort to model the behavior of high-pressure Venturi nozzles and supersonic thermal ejectors. Keenan and Neumann developed a one-dimensional theory based on gas dynamics to design ejectors [24]. Other first-principal analyses have considered gas dynamics for adiabatic ideal gas air mixing

and the Bernoulli equation for incompressible fluid mixing to model the nozzle behavior [3,7]. Additionally, second law analysis has been used to define ejector efficiency with reference to a reversible ejector, and it was found that if the motive and suction fluids are the same fluid, the reversible entrainment ratio efficiency and exergetic efficiency are nearly the same value [25]. Other studies utilized CFD to determine the effect of geometric features such as the throat shape, diffuser presence and angle, and motive inlet shape and diameter, showing that mixing length, diffuser angle, and effective throat area are all critical parameters to nozzle performance [8,9,12,26,27]. Additionally, the effect of adding swirl vanes to the nozzle diffuser to enhance the turbulent kinetic energy has been studied [28]. Cavitation in high-pressure Venturi nozzles has been found to further accelerate the flow and suppress turbulent velocity fluctuations [29,30]. For Venturi nozzles with incompressible flow, the effect of the injection angle for the suction fluid has been studied and a correlation for jet trajectory developed with standard error of 0.27 [31]. The effect of the ratio of the length to diameter of the mixing chamber has been studied for both supersonic and subsonic cases indicating that as the length to diameter ratio of the mixing chamber increases, the suction flow rate will first increase and then decrease [32,33].

Only a few studies have considered subsonic ejectors, and those studies typically only consider the case with air as both the motive and suction fluid [2,12,34]. For subsonic air-to-air Venturi mixing nozzles, the effect of the angle of the diverging section of the nozzle has been considered and found to be optimal between 4° and 14° [2,33,35]. The angle at which the suction stream meets the motive stream also impacts the performance of the nozzle. It was found that a larger angle leads to better penetration of the suction stream into the motive stream [31]. Additionally, any bend or flow separation in the nozzle will degrade the performance of the nozzle [31]. Predicting the suction flow rate of an arbitrary nozzle is still not well quantified.

This literature review shows that certain geometric features such as diffuser angle and throat design have been studied for supersonic or high-pressure Venturi nozzles. However, similar studies of subsonic, low-pressure Venturi nozzles are lacking. This work fills this gap by creating a design guide for such nozzles. The purpose of this work is to analyze subsonic, low-pressure Venturi mixing nozzles in order to characterize their performance and optimum geometry, and to develop

empirical models of Venturi nozzle performance can be used to determine the suction flow rate and inform the design of subsonic, low- pressure Venturi nozzles. If the suction flow rate of a particular nozzle is known, there have been multiple studies demonstrating the effect the addition of a diffuser will have on that flow rate [2,12,33,35].

There are many possible applications for low-pressure, subsonic Venturi nozzles, such as wastewater treatment. In this application, such Venturi nozzles can be used to accelerate air on the motive side and entrain wastewater steam on the suction side. In order to successfully separate clean water from contaminants in wastewater, the humidity of the air needs to be carefully controlled, which can be achieved by carefully controlling the ratio of suction flow rate to motive flow rate. Supersonic or high-pressure Venturi nozzles would be inappropriate for this application because supersonic nozzles would operate at temperatures too low for water treatment and high-pressure nozzles would increase the condensation rate of steam, potentially allowing steam to condense before it is separated from contaminants. Using a low-pressure, subsonic nozzle is an energy efficient way to control the humidity of air in some wastewater treatment applications [25,36,37]. Many other chemical and pharmaceutical processes also use such nozzles and would benefit from the ability to precisely control gas phase mixtures.

In subsonic Venturi nozzles, the suction flow rate is a function of the low pressure developed, and therefore, the high velocity at the throat of the nozzle. The velocity and pressure at the throat are dictated by the geometry of the nozzle and the motive stream flow rate. The static pressure at the suction inlet also influences the suction flow rate: increased pressure at the suction inlet leads to a larger pressure difference between the inlet and the throat and thus increases the suction flow rate. In this study, the effect of four different geometric parameters (Figure 3.1) on the suction flow rate are studied: the motive diameter (30–50 mm); the throat diameter (8–16 mm); the diameter through which the suction stream enters the nozzle, or the suction diameter (15–27 mm); and the distance between the throat and outlet of the nozzle, or the mixing length (30–80 mm).

Despite the relative simplicity of the Venturi nozzle and how well known the Venturi effect is, it is not straightforward to calculate the suction flow rate of these nozzles. The Bernoulli equation can be used to determine velocity from a known pressure drop but is not applicable to these nozzles because of the mixing of the

motive and suction streams. Gas dynamics relationships could be used to determine the low pressure at the throat of the nozzle based on the Mach number, but the Bernoulli equation or Darcy–Weisbach equation, which do not account for mixing, would still be needed to determine the suction flow rate from the calculated pressure difference. Alternatively, energy head loss calculations could be used to determine the outlet flow rate, and therefore the suction flow rate, based on a known pressure drop and major and minor losses across the entire nozzle; however, charts and empirical equations for the friction factor are based on constant cross section pipes or ducts and it is therefore difficult to accurately determine for nozzles with variable cross sections. Sample calculations for using governing equations and head loss to determine the suction flow rate were performed and are presented in Section 2.3.

In this paper, we present an empirical model or correlation that can be used as a design guide for low-pressure, subsonic Venturi nozzles for cases of air and air mixing, as well as air and steam mixing. Low-pressure, subsonic Venturi nozzles without diffusers were investigated experimentally, analytically, and numerically. The results of these investigations are combined into empirical models for the suction ratio as a function of the dimensionless groups formed from the geometric parameters, operating conditions, and fluid properties. The empirical model for suction ratio can be used to inform the design of Venturi nozzles given a desired suction ratio. This work allows one to determine the suction ratio of a Venturi nozzle based on known geometry and operating conditions.

3.2 Simulation and experimental validation methodology

Fifteen different Venturi nozzles were designed and simulated in ANSYS Fluent [38] to determine the effect of the geometry and operating conditions on the suction flow rate, with a total of 109 case studies considered. The geometries were simulated with different suction inlet pressures and motive mass flow inlet boundary conditions. In all cases, it was assumed that the outlet of the nozzle was at ambient pressure. The simulations were experimentally validated by measuring the pressure drop in the nozzles from the motive inlet to the outlet as a function of the motive mass flow rate and geometry. The results of those experiments were used to validate the simulations of the nozzles. In this study, the motive stream was air and the suction stream was either air or steam. The experimental setups and simulations are described in the following sections.

3.2.1 Air mixing experiment

In order to determine the mass flow rate suctioned into a nozzle by the Venturi effect, several Venturi mixing nozzles were designed in SolidWorks© and 3D printed on a MakerBot Replicator+, using CPE+ material. Figure 3.1 shows the internal geometry of one Venturi mixing nozzle. All geometries considered have the same basic shape as shown in Figure 3.1, with different motive diameters, throat diameters, suction inlet diameters, and mixing lengths.

The goal of these experiments was to determine the pressure drop across different Venturi nozzles as the motive mass flow rate was varied and to use the measured pressure drop to validate CFD simulations used to determine model boundary flow conditions. To achieve this goal, an experimental setup, shown in Figure 3.2, was developed. The air mass flow rate into the motive inlet of the nozzle was controlled using a pressure regulator (1) and measured using an Endress + Hauser Promass I Coriolis flow meter, with an instrument uncertainty of ±0.5% of the reading (2). The motive mass flow rate was varied from 1 g/s to 5 g/s. The outlet of the nozzle was open to ambient pressure. This experiment was conducted with two different suction inlet conditions. The first was with the suction inlet open to ambient and the second was with the suction inlet sealed such that there could be no flow into the nozzle from the suction inlet. The motive pressure drop (dP) across the nozzle (3) was measured for both cases using a Setra 230 differential pressure transducer with a full scale of 1 psi and an instrument uncertainty of ±0.25% of full scale or 14 Pa. The motive pressure drop was used as a proxy measurement for the suction flow rate because when a flow meter was attached to either the suction inlet or outlet of the nozzle to directly measure the suction flow rate, a pressure drop was introduced in the system such that there was no suction flow. There were 36 experimental data points without suction and 36 data points with suction for the air and air mixing experiment. Table 3.1 shows the nozzles and motive mass flow rates tested for each nozzle. Each experiment was repeated three times.

3.2.2 Air and steam mixing experiment

In order to determine the suction flow rate with steam as the suction fluid, a similar procedure was used to measure the motive pressure drop as a proxy measurement for the suction flow rate because a direct measurement of the suction flow rate adds an additional pressure drop on the suction side and changes the suction flow rate.

The experimental design is shown in Figure 3.3. The setup is similar to the previous experimental design, but with a few additional components. To supply air flow to the motive inlet, air was fed through a pressure regulator (1), into a Endress + Hauser Promass I Coriolis flow meter (2) and then an Omega AHPF-121 inline heater (4) that was controlled by an ITC-100VH PID (3). The pressure regulator (1) was adjusted until the desired air motive flow rate was read on the Coriolis flow meter (2). This allowed the mass flow rate of air to be measured, and the temperature of the air to be increased just before entering the nozzle to minimize condensation in the nozzle. An industrial 12 kW SteamSpa steam generator (9) was used to supply steam to the suction inlet. The steam generator produces a single source of steam, which is then split into two hoses (7 and 8) upon leaving the generator. The first of these hoses (7) was connected to the suction inlet of the nozzle (6), while the second (8) was directed away from the experimental setup to serve as a bypass for the steam not entering the nozzle. The opening of the second hose (8) was restricted using a clamp so that constant pressure could be maintained at the suction inlet as the motive flow varied between experiments.

Table 3.1: Air mixing experimental test matrix.

Nozzle Name /Code	**Motive Diameter (m)**	**Throat Diameter (m)**	**Suction Diameter (m)**	**Mixing Length (m)**	**Motive Mass Flow Rate (g/s)**	**Suction Inlet Condition**
T1	0.04	0.012	0.027	0.0385	1–5	Sealed and Open
LR3	0.04	0.016	0.027	0.08	1–5	Sealed and Open
AR5	0.04	0.016	0.0175	0.0385	1–5	Sealed and Open

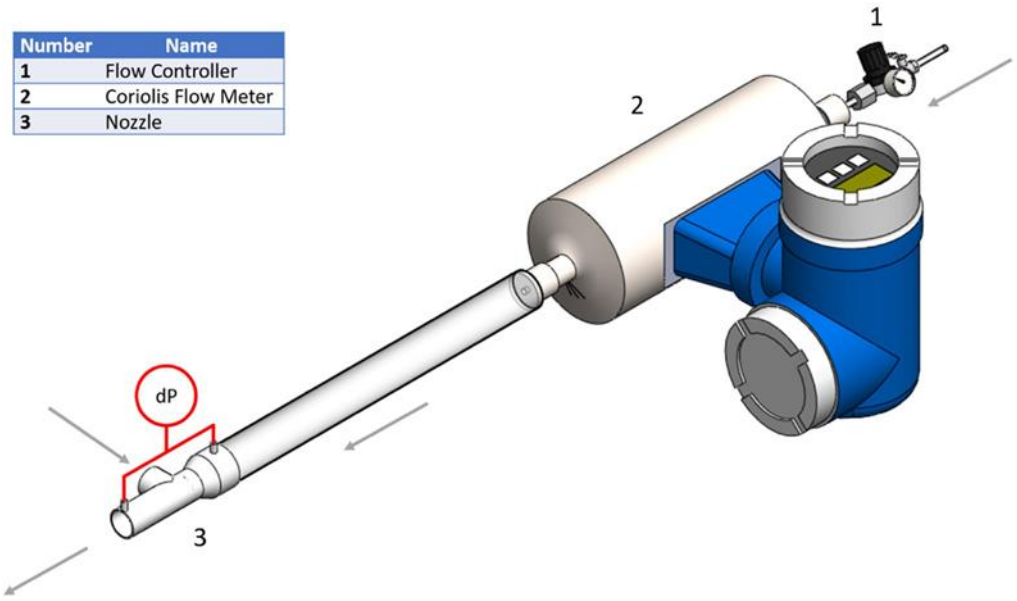

Figure 3.2: Air mixing experimental setup schematic.

Instrumentation locations can be seen in Figure 3.3, represented by dP for the motive pressure drop, P for the gage static suction pressure, and T for the thermocouple at the motive inlet to measure the air temperature. One Setra 230 differential pressure transducer with a full scale of 5 psi was used to measure the motive pressure drop from the motive inlet to the outlet. A second Setra 230 differential pressure transducer with a full scale of 1 psi was connected to the steam inlet, with the other side open to ambient, to read the gage static pressure at that location. Air temperature was held constant at 105°C to ensure it was above the saturation temperature of the steam to avoid phase change in the nozzle. Air mass flowrates were varied between 1.5 and 4.5 g/s. The T1 and T3 nozzles were tested, the geometric details of these nozzles are shown in Table 3.1, with a total of 11 data points. Each test was repeated three times.

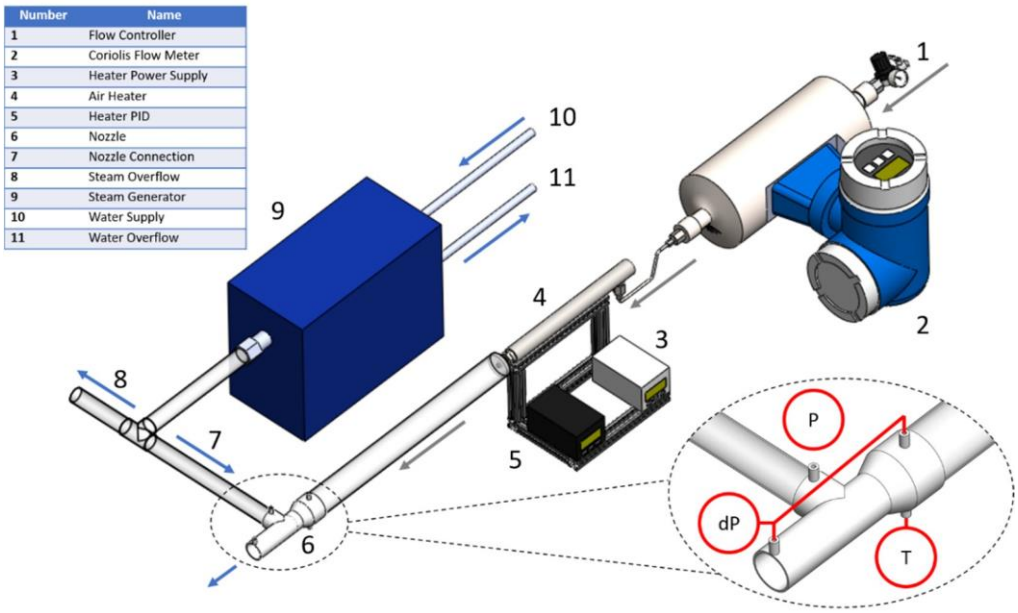

Figure 3.3: Steam mixing experimental setup schematic.

For these experiments, the sources of uncertainty were the Coriolis flow meter, the differential pressure transducers, and the thermocouple. The mass flow rate was measured using an Endress + Hauser Promass I Coriolis flow meter with an instrument uncertainty of ±0.5% of the reading. The suction inlet pressure (9) was measured using a Setra 230 differential pressure transducer with a full scale of 1 psi and an instrument uncertainty of ±0.25% of full scale or 14 Pa. The motive inlet pressure drop (10) was measured using a Setra 230 differential pressure transducer with a full scale of 5 psi and an instrument uncertainty of ±0.25% of full scale or 70 Pa. The type k thermocouple used to measure the air temperature had an instrument uncertainty of ±2.2°C.

3.2.3 Air mixing determination and validation

CFD simulations were used as a tool to determine the suction flow rate from the measured pressure drop, such that the simulations, once validated, could provide the basis for the empirical model development. ANSYS Fluent 19.2 [38] was used for all CFD simulations. The geometries and boundary conditions from the experiment were used to determine the suction mass flow rate for each experimental case.

For each simulation case, the motive flow rate, motive pressure drop across the nozzle, and static pressure at the suction inlet were known from the experiments. For the case with no suction, the suction inlet was defined as a wall rather than an

inlet in simulation so no flow could cross the boundary. For the case with suction, the suction inlet was open to ambient conditions and thus the suction inlet gage static pressure was set to zero. The motive inlet was defined as a mass flow inlet boundary. The nozzle outlet was to open ambient conditions in all cases, so the outlet boundary condition was defined to be zero gage static pressure. The energy model and realizable k-ε turbulence model were the only models used. The simulations were steady, to mimic the steady state measurements of the experiments. A pressure-based solver with a second-order discretization scheme was used for each simulation. The SIMPLE pressure-velocity coupling algorithm was also used for each simulation. Additionally, the ambient pressure condition was set to match the ambient pressure of the experiments (88 kPa). Each simulation was considered to be converged when all residuals had values less than 0.0001 for air mixing and 0.001 for air and steam mixing. The measured motive pressure drop from experiments was compared to the simulated motive pressure drop from CFD to validate each simulation. Three nozzles were tested for each suction condition.

Symmetry was used so only half of the fluid body (Figure 3.1) was meshed and simulated. In the simulations, the symmetrical half of the nozzle fluid body was meshed, using a 3D linear mesh, and mesh size was reduced (increasing resolution) until residuals were less than 0.0001 and the predicted suction mass flow rate varied by less than 0.2% from one mesh to the next, indicating that the primary result of interest from the simulation was independent of the mesh. The results of the mesh independence study are shown in Figure 3.4. Table 3.2 shows the grid refinement study and discretization error with a fine-grid convergence index (CGI_{fine}[21]) of 5.5% and 0.7% for two critical parameters [39].

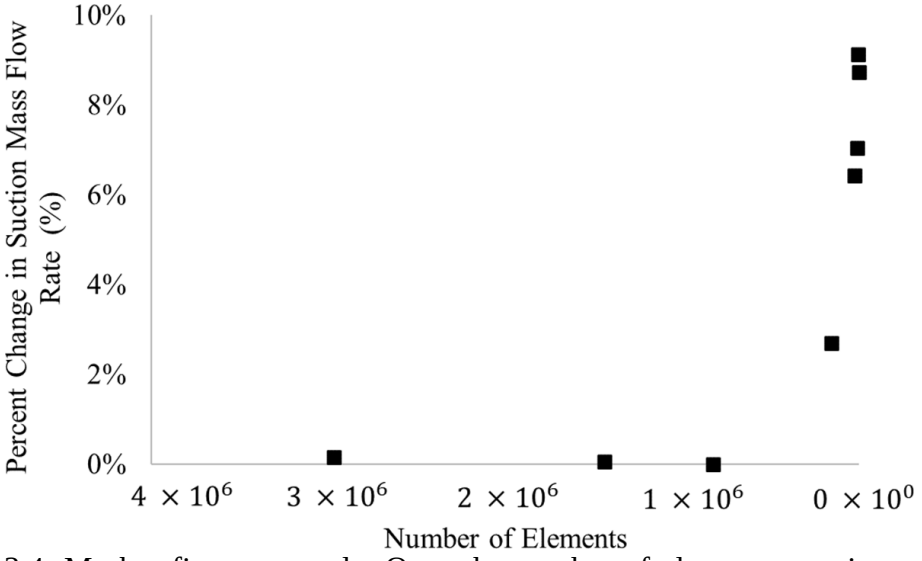

Figure 3.4: Mesh refinement study. Once the number of elements was increased past 828,360, there was effectively no change in the result and mesh independence was reached.

Table 3.2: Grid refinement study and discretization error.

Grid Specifications	**Number of Cells: Case I: 4,702,076, Case II: 1,439,997, Case III:828,620**	$r_{21} = 1.48$ $r_{32} = 1.20$
Physical Parameter (φ)	**Suction Mass Flow Rate (kg/s)**	**Motive Pressure Drop (Pa)**
$\varphi\ in$ Case I	0.004325	8980.95
$\varphi\ in$ Case II	0.004489	9020.66
$\varphi\ in$ Case III	0.004617	9151.77
$\varphi_2 - \varphi_1$	1.64×10^{-4}	39.71
$\varphi_3 - \varphi_2$	1.28×10^{-4}	31.11
p	1.59	1.56
φ_{ext}^{21}	0.00414	8934.04
φ_{ext}^{32}	0.00411	8926.41
e^{21}	3.8%	0.4%
e^{32}	2.8%	0.3%
e_{ext}^{21}	4.6%	0.5%
e_{ext}^{32}	9.2%	1.1%
GCI_{fine}^{21}	5.5%	0.7%

Figures 3.5 and 3.6 show the experimental results for the closed and open suction inlet, respectively, for each tested nozzle compared to the simulation result. For all motive flow rates and suction conditions, the experimental and simulated results for motive mass flow rate agree to within 10%. The no suction case has a mean absolute percentage error of 7.5% and a root mean square error of 8.4%. The suction case

has a mean absolute percentage error of 5.7% and a root mean square error of 6.5%. The error was calculated as the difference between the experimental and simulated pressure drop. Based on the 10% agreement between the simulation and experiments, the simulations were considered to be validated. From the validated simulation, the suction mass flow rate can be found.

Table 3.3: Summary of nozzle geometries in parametric study. The AR code refers to the area ratio being varied while all other geometric parameters were held constant. Similarly, the LR, T, and S codes refer to varying the length ratio, throat diameter, and suction inlet diameter, respectively.

Name/Code	Motive Diameter (m)	Throat Diameter (m)	Suction Diameter (m)	Mixing Length (m)
D2	0.04	0.016	0.027	0.0385
AR1	0.05	0.016	0.027	0.0482
AR2	0.05	0.016	0.02	0.0482
AR3	0.03	0.016	0.027	0.0289
AR4	0.05	0.016	0.0175	0.0482
AR5 *	0.04	0.016	0.0175	0.0385
AR6	0.035	0.016	0.015	0.0337
LR1	0.04	0.016	0.027	0.03
LR2	0.04	0.016	0.027	0.06
LR3 *	0.04	0.016	0.027	0.08
T1 *	0.04	0.012	0.027	0.0385
T2	0.04	0.01	0.027	0.0385
T3 *	0.04	0.008	0.027	0.0385
S1	0.04	0.016	0.015	0.0385
S2	0.04	0.016	0.02	0.0385

Asterisks denote a geometry that was experimentally validated.

3.2.4 Air and steam mixing determination and validation

For the steam simulation validation, the same procedure was followed as described above for air mixing. For the case of steam mixing, the suction inlet was at a pressure above ambient due to steam entering the nozzle at that location. For these simulations the multi-species model was used with ideal gas air and steam. With the exception of changing the suction inlet boundary condition to be steam above ambient pressure and using the Fluent multi-species model, all other boundary conditions, meshes, and models were the same as for the air mixing tests. The simulations were considered to be converged when the residuals reached 0.001. As shown in Figure 3.7, the experimental and simulation results agree within 11%, with a mean absolute error of 10.5% and a root mean square error of 10.6% for each

steam mixing case, and therefore the simulation is considered to be validated. For all cases, the experimental data had a lower motive pressure drop than the simulation predicted. This could be due to the fact that phase change was neglected in the simulations, but there was a small amount of condensation in the nozzle during each experiment.

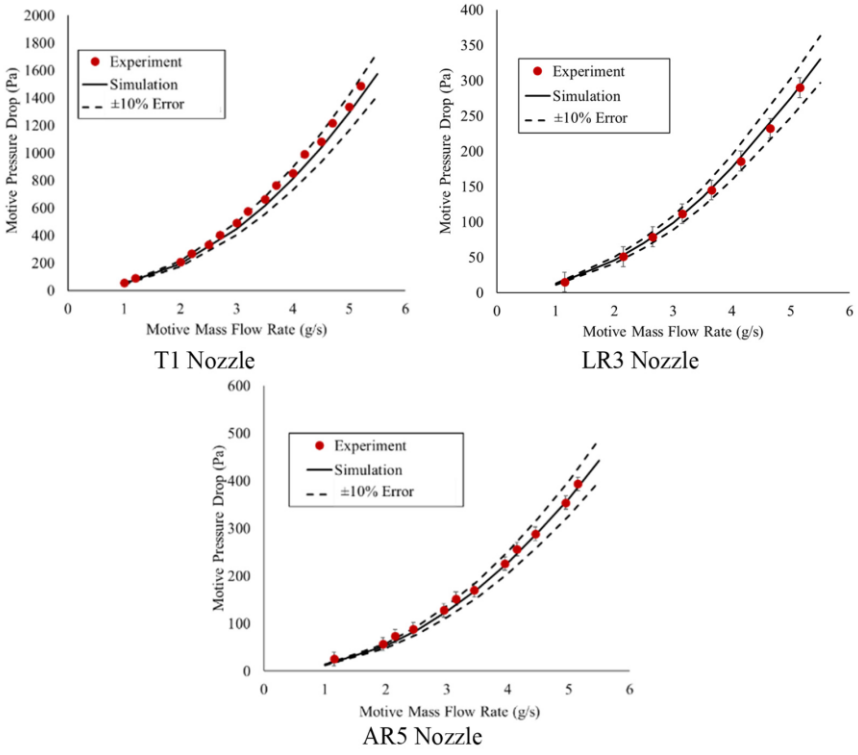

Figure 3.5: Motive pressure drop (Pa) vs. motive mass flow rate (g/s) for nozzle tests with no suction. See Table 3.3 for nozzle geometry details. For the T1 geometry, the uncertainty bars are smaller than the experimental marker used.

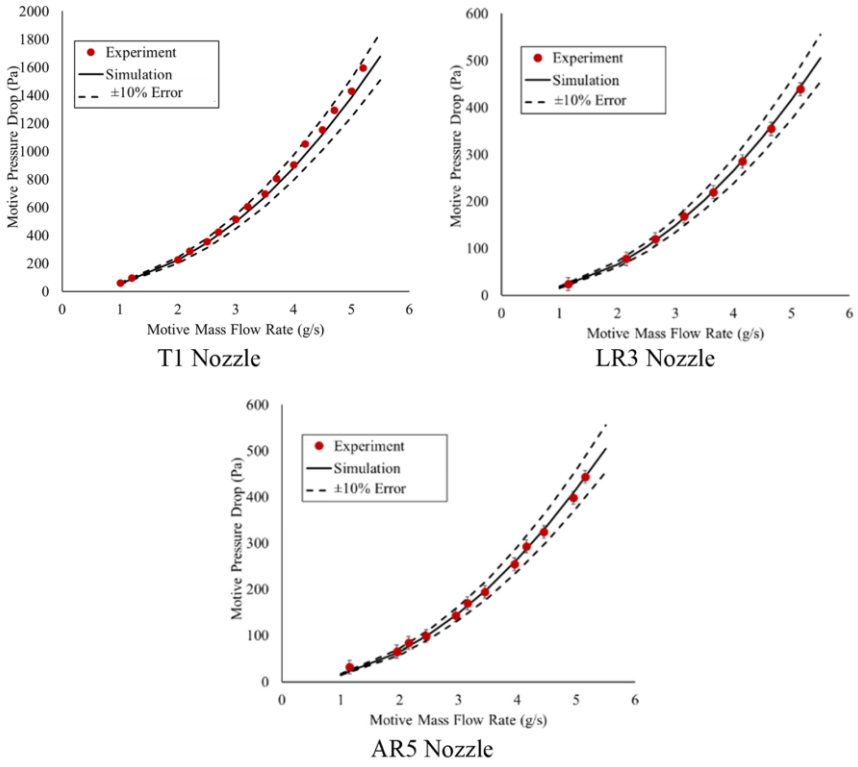

Figure 3.6: Motive pressure drop (Pa) vs. motive mass flow rate (g/s) for air mixing tests. See Table 3.3 for nozzle geometry details. For the T1 geometry, the uncertainty bars are smaller than the experimental marker used.

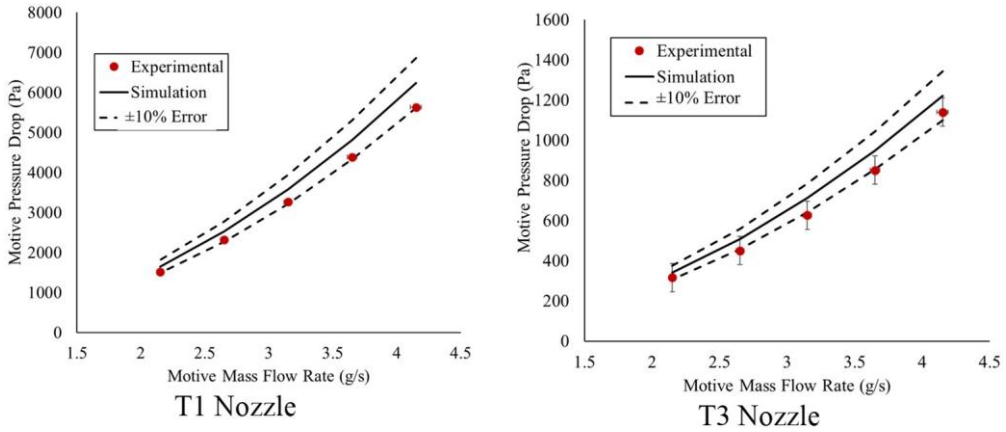

Figure 3.7: Motive pressure drop (Pa) vs. motive mass flow rate (g/s) for steam tests. See Table 3.3 for nozzle geometry details.

In summary, both the air mixing as well as the air and steam mixing cases are validated with a maximum error of 10.6%, and therefore the simulations were considered to be validated and trusted moving forward with a parametric study and correlation development.

3.3 Governing equations and flow head calculations

As previously discussed, some applications, such as water treatment, require precise knowledge of the suction flow rate, or suction ratio, in order to successfully operate. Unfortunately, the suction ratio of the nozzles can be difficult to accurately determine using flow design calculations. As an example, here governing equation calculations and energy head loss calculations are used to calculate the suction flow rate and compared to the suction flow rate from the validated simulations [40].

The governing equation calculation approach was evaluated based on the continuity (Equation 3.1), conservation of energy (Equation 3.2), and conservation of momentum (Equation 3.3) equations. For this analysis, a control volume that crosses the throat, suction inlet, and outlet of each nozzle was considered. For air and air mixing, Equation 3.6 was used to determine the enthalpy of the outlet stream. For air and steam mixing, where the psychrometrics of the humid air must be considered, Equations 3.6 – 3.9 were used to determine the relative humidity and thus the enthalpy of the outlet humid stream. For both cases, Equations 3.4 and 3.5 were used to determine the densities of the air at the throat and outlet stream. Alternatively, a flow head loss method based on the head form of the energy equation could be used to calculate the suction mass flow rate based on the major and minor losses in each nozzle; however, it was found that the head loss method is less accurate than the governing equation approach, as shown in Figure 3.8.

Figure 3.8 shows the suction mass flow rate as determined by the governing equations and validated simulations versus the motive mass flow rate for each experimental data point. On average, the governing equations predict the suction mass flow rate with a 270% error. This method is insufficiently accurate to determine the suction mass flow rate of the low-pressure Venturi nozzles considered in this study. A different method is necessary to precisely calculate the suction mass flow rate of these nozzles, and thus inform the design of the nozzles. The empirical models presented in Section 3.6 of this paper allow for precise calculation of the suction ratio and therefore suction mass flow rate.

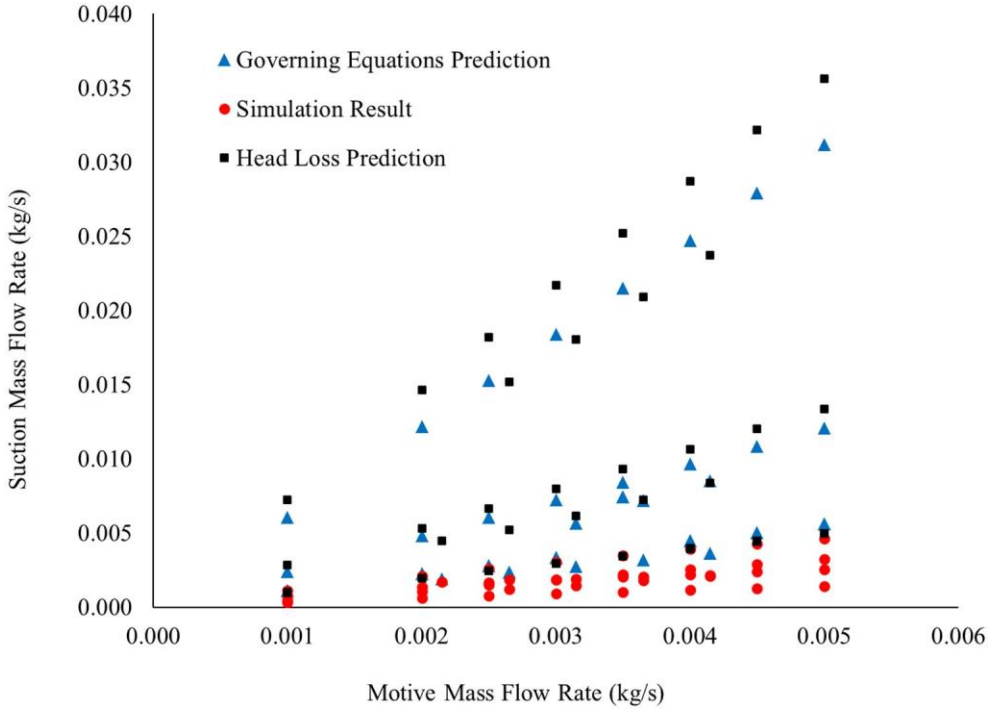

Figure 3.8. Head loss predicted suction mass flow rate, governing equations predicted suction mass flow rate, and validated simulation suction mass flow rate vs. motive mass flow rate. The suction mass flow rate predicted by the governing equations method is 270% higher than the simulation result. The suction mass flow rate predicted by the head loss method is approximately 380% higher than the mass flow rate from the validated simulation. The simulation has an average error of 8% relative to the experimental data.

$$\dot{m}_m + \dot{m}_s = \dot{m}_o \tag{3.1}$$

$$\dot{m}_m \left(h_t + \frac{1}{2}V_t^2\right) + \dot{m}_s \left(h_s + \frac{1}{2}V_s^2\right) = (\dot{m}_o)\left(h_o + \frac{1}{2}V_o^2\right) \tag{3.2}$$

$$P_{t_{gage}} A_m = \dot{m}_o V_o - \dot{m}_m V_t - \dot{m}_s V_s \tag{3.3}$$

$$\rho_t = f(P_t, T_{ambient}) \tag{3.4}$$

$$\rho_o = \frac{\dot{m}_m \rho_t + \dot{m}_s \rho_s}{\dot{m}_m + \dot{m}_s} \tag{3.5}$$

$$h_{o_{air}} = f(\rho_o, P_o) \tag{3.6}$$

$$h_{o_{steam}} = f(T_o, P_o) \tag{3.7}$$

$$\omega = {\dot{m}_{s_{steam}}}\Big/{\dot{m}_m} \tag{3.8}$$

$$h_o = h_{o_{air}} + \omega h_{o_{steam}} \quad (3.9)$$

3.4 Parametric study

In order to determine the suction mass flow rate for different nozzles, a parametric study was completed in using the validated CFD simulations. Fifteen different geometries with varying motive inlet diameters, throat diameters, suction inlet diameters, and mixing lengths were simulated with varying boundary conditions. All geometries are given in Table 3.3. Geometries were chosen to provide a range of values for each of the selected geometrical parameters: motive diameter, throat diameter, suction diameter, and mixing length. Each parameter was varied to provide at least four different values. These values were chosen such that the average of each geometric parameter provides a fixed suction ratio to keep the ratio of steam to air below the carrying capacity of water in air for the majority of steam mixing cases. It was confirmed that flow in each geometry remains subsonic and incompressible for all relevant conditions prior to including the geometry in the parametric study.

All flow conditions are shown in the simulation test matrix in Table 3.4. The motive inlet was defined to be a mass flow inlet with a flow rate of either 5.2 or 20.8 g/s. These flow rates were chosen because 20.8 g/s is the desired flow rate for one application of these nozzles and 5.2 g/s was selected to provide a lower range of suction ratios [33]. The motive inlet fluid was ideal gas air for all cases. The suction inlet boundary condition was a pressure inlet with a static gage pressure of either 10 Pa, 100 Pa, or 500 Pa. The suction fluid was either ideal gas air or steam. For all cases, the nozzle outlet boundary condition was defined to be 0 Pa gage. Every combination of geometry and boundary conditions summed to 109 different cases considered in the parametric study. For each case, the suction mass flow rate and dimensionless suction ratio, or ratio of suction mass flow rate to motive mass flow rate, were calculated.

Table 3.4: Test matrix for parametric study. A total of 109 cases were studied. The AR code refers to the area ratio being varied while all other geometric parameters were held constant. Similarly, the LR, T, and S codes refer to varying the length ratio, throat diameter, and suction inlet diameter, respectively.

Name/Code	Motive Flow Rate (g/s)	Suction Static Pressure (Pa)	Suction Fluid
D2	20.8	10,100,500	Air, Steam
	5.2	10,500	Air, Steam
AR1	20.8	10,100,500	Air, Steam
AR2	20.8	10,100,500	Air, Steam
AR3	20.8	10,100,500	Air, Steam
AR4	20.8	10,100,500	Air, Steam
AR5	20.8	10,100,500	Air, Steam
AR6	20.8	10,100,500	Air, Steam
LR1	20.8	10,100,500	Air, Steam
	5.2	10,500	Air, Steam
LR2	20.8	10,100,500	Air, Steam
LR3	20.8	10,100,500	Air, Steam
	5.2	10,500	Air, Steam
T1	20.8	10,100,500	Air, Steam
	5.2	10,500	Air, Steam
T2	20.8	10,100,500	Air, Steam
T3	20.8	10,100,500	Air, Steam
	5.2	10,100,500	Air, Steam
S1	20.8	10,100,500	Air, Steam
	5.2	100	Air, Steam
S2	20.8	10,100,500	Air, Steam
	5.2	100	Air, Steam

3.5 Empirical model formulation

In order to develop a model for the suction ratio as a function of the geometry and operating conditions, the form of the model must first be determined. The suction mass flow rate ($\dot{m}_s$) was taken to be a function of the motive mass flow rate ($\dot{m}_m$), the motive inlet area (A_m), the throat diameter (D_t), the suction inlet diameter (D_s), the mixing length (L), the motive fluid density (ρ_m), the suction fluid kinematic viscosity (ν_s), the motive fluid viscosity (μ_m), and the gage static pressure at the suction inlet (P_{static}) (Equation 3.10). Consequently, the functional form for the suction mass flow rate becomes:

$$\dot{m}_s = f(\dot{m}_m, A_m, D_t, D_s, L, \rho_m, \nu_s, \mu_m, P_{static}) \tag{3.10}$$

The Buckingham Pi Theorem was used to determine the dimensionless groups that define this system as:

$$\frac{\dot{m}_s}{\dot{m}_m} = \mathbb{C}\left[\left(\frac{A_m}{A_t}\right)^a \left(\frac{L}{D_s}\right)^b \left(\frac{\dot{m}_m}{\mu_m D_t}\right)^c \left(\frac{\nu_s}{\nu_m}\right)^d \left(\frac{P_{static} D_t^4 \rho_m \pi^2}{8 \dot{m}_m{}^2}\right)^e\right] \qquad (3.11)$$

The third independent dimensionless group on the right side of the above expression ($\frac{\dot{m}_m}{\mu_m D_t}$) is the Reynolds number at the throat of the nozzle. The last independent dimensionless group ($\frac{P_{static} D_t^4 \rho_m \pi^2}{8 \dot{m}_m{}^2}$) is the ratio of the gage static pressure at the suction inlet to the dynamic pressure at the throat. Using these definitions, Equation 3.11 can be written as:

$$\frac{\dot{m}_s}{\dot{m}_m} = \mathbb{C}\left[\left(\frac{A_m}{A_t}\right)^a \left(\frac{L}{D_s}\right)^b \left(Re_{motive,throat}\right)^c \left(\frac{\nu_s}{\nu_m}\right)^d \left(\frac{P_{static,suction}}{P_{dynamic,throat}}\right)^e\right] \qquad (3.12)$$

The coefficient and exponents of the correlation were determined using a multi-variable global optimization code in Python. The global constrained minimization algorithm determined the best fit for the coefficient and exponents of the correlation based on the 109 parametric study cases, using the Levenberg–Marquardt scheme [41,42].

3.6 Results

Seven different empirical models were developed and evaluated to determine which parameters are most important to prediction of nozzle performance, and to find which empirical model is best able to predict the nozzle performance. Details of each empirical model are given below. Every empirical model considered, as well as their errors and ranges of applicability are summarized in Table 3.5 in order to provide a design reference for Venturi nozzles.

3.6.1 Suction ratio models

Comparing the suction ratio predicted by the empirical model (Equation 3.17 in Table 3.5) to the suction ratio determined using the validated simulations, the empirical model predicts the suction ratio with a mean absolute percentage error of 22% and a root mean square error of 27%. Figure 3.9 shows the suction ratio predicted by the global correlation compared to the suction ratio determined by the validated simulations. In Figure 3.9, the red circles indicate the correlation prediction for air mixing cases and the blue squares indicate the prediction for steam mixing. The solid black line indicates what the suction ratio should be to have 0%

error with the simulated suction ratio, and the dashed lines show ±10% and ±20% of the simulated value. Both air mixing and steam mixing cases are equally well predicted by the global correlation. If the correlation is developed considering only the air mixing cases (Equation 3.18) or only considering the air and steam mixing cases (Equation 3.19), the correlation becomes slightly more accurate but not significantly so, as shown in Table 3.5. Instead, the error in the global correlation comes from two flow regimes being predicted by the same correlation; there is a clear discrepancy in Figure 3.9 at the simulated suction ratio of one. Cases with low suction ratios, less than one, are relatively well predicted with a mean absolute percentage error of 20% while cases with high suction ratios, greater than one, are relatively poorly predicted with a mean absolute percentage error of 43%.

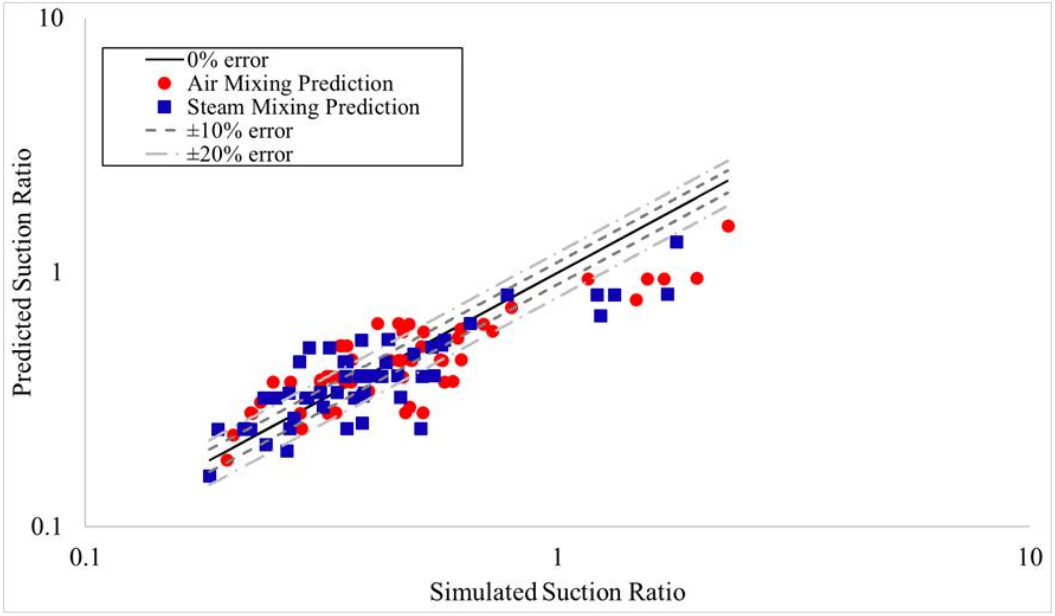

Figure 3.9: Suction ratio predicted by global suction ratio correlation vs. suction ratio from validated simulation.

The increase in mean absolute percentage error for the high suction ratio cases indicates that the correlation does not well predict the behavior of the mixing nozzles for those cases. Each of the high suction ratio cases has a low Reynolds number and a high-pressure ratio. This indicates that the high suction ratio cases may be driven more by the applied static pressure at the suction inlet than the Venturi effect from the motive mass flow rate and throat diameter. Additionally, the low suction ratio cases all have a relatively high Reynolds number and a relatively low pressure ratio. If the low and high suction ratio cases are considered

to be driven by different phenomena, inertia and pressure, respectively, then it may be better to model each regime separately.

If only the low suction ratio cases are considered in the optimization, the result is Equation 3.20, given in Table 3.5. The low suction ratio correlation predicts the suction ratio with a mean absolute percentage error of 18%, and a root mean square error of 22% as shown in Figure 3.10.

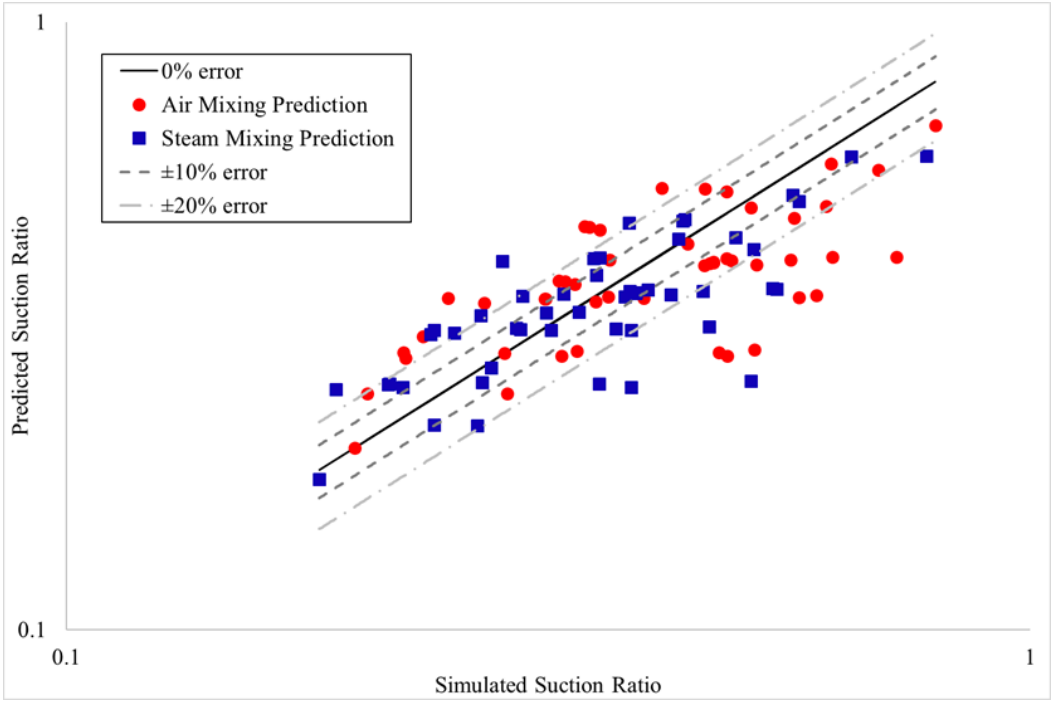

Figure 3.10: Suction ratio predicted by low suction ratio correlation vs. suction ratio from validated simulation.

If only the high suction ratio cases are considered in the optimization, the result is Equation 3.21. The high suction ratio correlation predicts the suction ratio with a mean absolute percentage error of 5%, and a root mean square error of 6%, as shown in Figure 3.11. Separating the global correlation including both high and low suction ratios into one correlation for low suction ratio and one correlation for high suction ratio allows for more accurately informed decisions about the design of a Venturi nozzle geometry, assuming that the desired suction ratio can be identified as either high or low. Figure 3.12 shows the suction ratio predicted by the low and high suction ratios on one plot, with the correlation used for each suction ratio range.

A sensitivity analysis was conducted by increasing then decreasing the value of each dimensionless group by 10% compared to the original value and calculating the maximum relative error, mean absolute percentage error, and root mean square

error for each case. The sensitivity analysis revealed that the area ratio $\left(\frac{A_m}{A_t}\right)$ had the largest impact on the error of each correlation of all the dimensionless groups, followed by the kinematic viscosity ratio $\left(\frac{\nu_s}{\nu_m}\right)$ and then the Reynolds number $\left(\frac{\dot{m}_m}{\mu_m D_t}\right)$. Comparing the effect of each dimensionless group between the low and high suction ratio cases, it was found that the geometry has a larger impact on the suction ratio for the low suction ratio cases than the high suction ratio cases. The high suction ratio cases are more dependent on operating conditions than the geometry of the nozzle. These results support the hypothesis that the suction flow for high suction ratio cases is largely driven by the applied static pressure at the suction inlet, while the low suction ratio cases are more dependent on geometry because they are truly Venturi driven flow and the area ratio is critical to the performance.

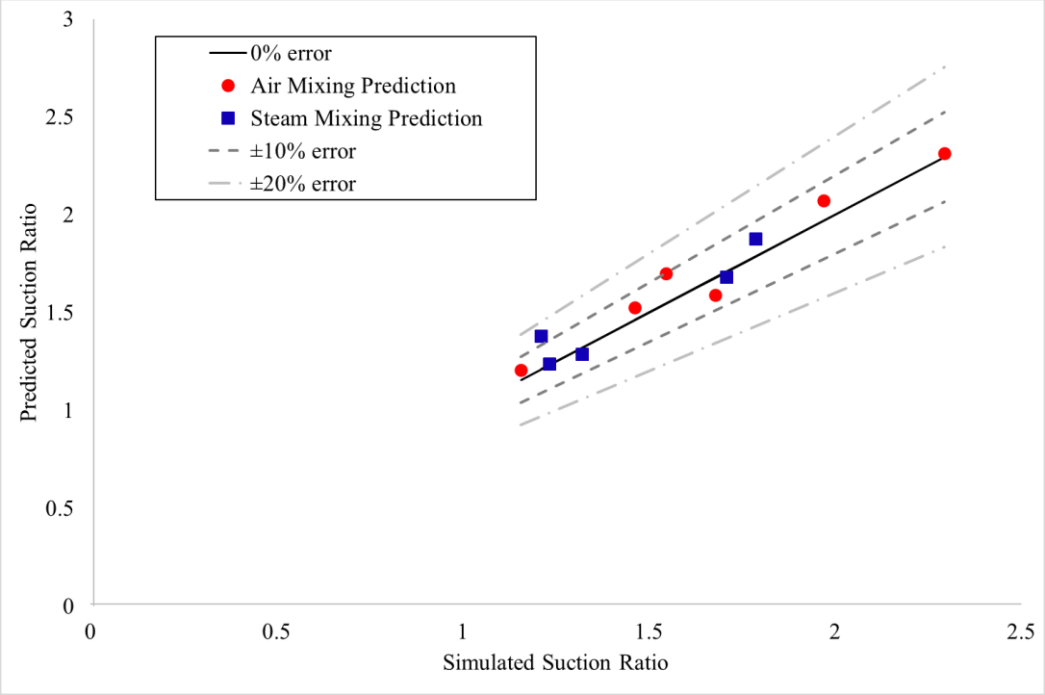

Figure 3.11: Suction ratio predicted by the high suction ratio correlation vs. the suction ratio from the validated simulation.

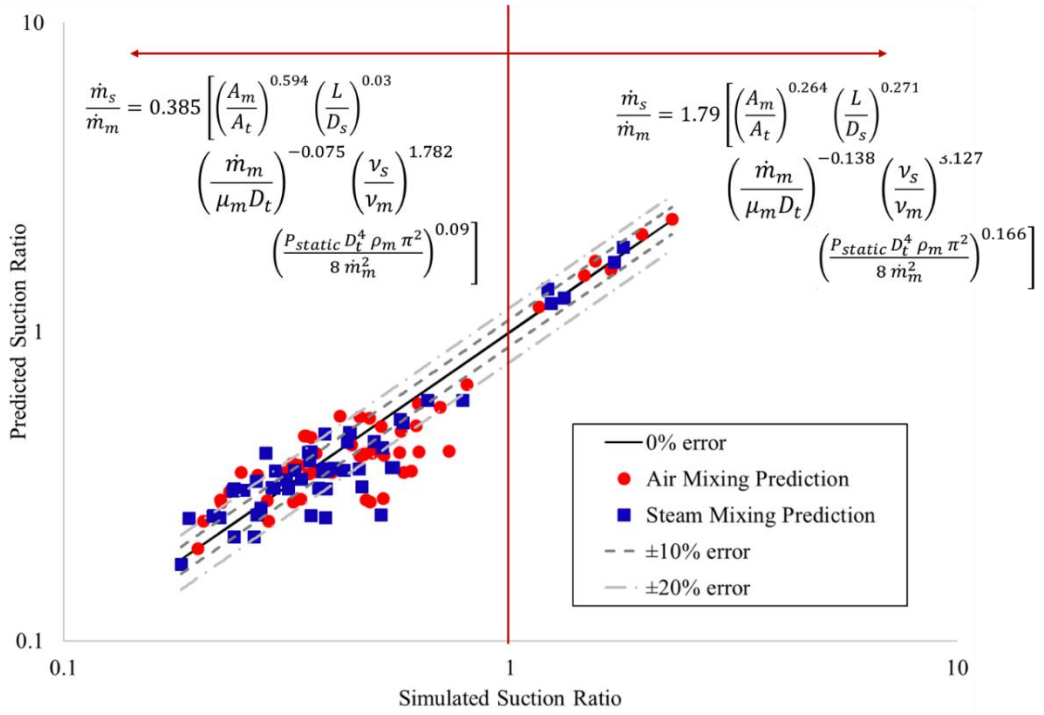

Figure 3.12: Suction ratio predicted by low and high suction ratio correlations vs. the suction ratio from the validated simulation.

3.6.2 Momentum ratio and dynamic pressure ratio models

Given the apparent dependence of the global suction ratio correlation on pressure, two alternative empirical models were evaluated: momentum ratio and dynamic pressure ratio. For these models, either the momentum ratio or the dynamic pressure ratio is predicted by the global correlation, instead of the suction ratio. For each of these cases, the form of the correlation can be determined, again, using the Buckingham Pi Theorem.

For the momentum ratio, the suction momentum term ($\rho_s \dot{m}_s$) was considered to be a function of the motive mass flow rate ($\dot{m}_m$), the motive inlet area (A_m), the throat diameter (D_t), the suction inlet diameter (D_s), the mixing length (L), the motive fluid density (ρ_m), the motive fluid viscosity (μ_m), and the gage static pressure at the suction inlet (P_{static}), which, when non-dimensionalized, yields the following:

$$\rho_s \dot{m}_s = f(\dot{m}_m, A_m, D_t, L, D_s, \mu_m, \rho_m, \nu_s, P_{static}) \tag{3.13}$$

$$\frac{\rho_s\,\dot{m}_s}{\rho_m \dot{m}_m} = \mathbb{C}\left[\left(\frac{A_m}{A_t}\right)^a \left(\frac{L}{D_s}\right)^b \left(\frac{\dot{m}_m}{\mu_m\,D_t}\right)^c \left(\frac{\nu_s}{\nu_m}\right)^d \left(\frac{P_{static}\,D_t^4\,\rho_m\,\pi^2}{8\,\dot{m}_m{}^2}\right)^e\right] \tag{3.14}$$

When the momentum ratio correlation is optimized, it yields Equation 3.22, also given in Table 3.5. The resulting correlation yields a mean absolute percentage error

of 28%, and a root mean square error of 36% when compared to the validated simulations.

For the dynamic pressure ratio, the suction dynamic pressure ($8\,\dot{m}_m{}^2/(D_t^4\rho_s\pi^2)$) was considered to be a function of the motive mass flow rate ($\dot{m}_m$), the motive inlet area (A_m), the throat diameter (D_t), the mixing length (L), the motive fluid density (ρ_m), the motive fluid viscosity (μ_m), and the gage static pressure at the suction inlet (P_{static}), yielding Equation 3.15 below, which when non-dimensionalized gives Equation 3.16. The coefficient and exponents determined using the global optimization are shown in Equation 3.23. The global dynamic pressure ratio has a mean absolute percentage error of 48%, and a root mean square error of 56%. In Equation 3.16, the mixing length is nondimensionalized using the throat diameter, rather than the suction inlet diameter as in the suction ratio and momentum ratio models because the suction diameter is on the independent side of the equation, but the remaining terms are identical to those of the previously discussed correlations.

$$\frac{8\dot{m}_s}{D_S^4\rho_s\pi^2} = f(\dot{m}_m, A_m, D_t, L, \mu_m, \rho_m, \nu_s, P_{static}) \tag{3.15}$$

$$\frac{\dot{m}_s D_t^4 \rho_m}{\dot{m}_m D_s^4 \rho_s} = \mathbb{C}\left[\left(\frac{A_m}{A_t}\right)^a \left(\frac{L}{D_t}\right)^b \left(\frac{\dot{m}_m}{\mu_m D_t}\right)^c \left(\frac{\nu_s}{\nu_m}\right)^d \left(\frac{P_{static}\, D_t^4\, \rho_m\, \pi^2}{8\,\dot{m}_m^2}\right)^e\right] \tag{3.16}$$

Table 3.5: Summary of proposed empirical models, ranges of applicability, mean absolute percentage error (MAPE), and root mean square error (RSME).

	Empirical Model	MAPE	RSME	Applicability	Equation
Global suction ratio	$\frac{\dot{m}_s}{\dot{m}_m} = 3.88\left[\left(\frac{A_m}{A_t}\right)^{0.734}\left(\frac{L}{D_s}\right)^{0.006}\left(\frac{\dot{m}_m}{\mu_m D_t}\right)^{-0.288}\left(\frac{\nu_s}{\nu_m}\right)^{2.17}\left(\frac{P_{static}\, D_t^4\, \rho_m\, \pi^2}{8\, \dot{m}_m^2}\right)^{0.123}\right]$	22%	27%	$0.183 \leq \frac{\dot{m}_s}{\dot{m}_m} \leq 2.294$ $20{,}690 \leq Re_t \leq 165{,}521$ $0.0001 \leq \frac{P_{static}}{P_{dynamic}} \leq 1.319$ Air mixing, air and steam mixing	(3.17)
Air only suction ratio	$\frac{\dot{m}_s}{\dot{m}_m} = 12.7\left[\left(\frac{A_m}{A_t}\right)^{0.785}\left(\frac{L}{D_s}\right)^{-0.134}\left(\frac{\dot{m}_m}{\mu_m D_t}\right)^{-0.396}\left(\frac{P_{static}\, D_t^4\, \rho_m\, \pi^2}{8\, \dot{m}_m^2}\right)^{0.12}\right]$	22%	26%	$0.199 \leq \frac{\dot{m}_s}{\dot{m}_m} \leq 2.294$ $20{,}690 \leq Re_t \leq 165{,}521$ $0.0001 \leq \frac{P_{static}}{P_{dynamic}} \leq 1.319$ Air mixing	(3.18)
Steam only suction ratio	$\frac{\dot{m}_s}{\dot{m}_m} = 1.5\left[\left(\frac{A_m}{A_t}\right)^{0.688}\left(\frac{L}{D_s}\right)^{0.147}\left(\frac{\dot{m}_m}{\mu_m D_t}\right)^{-0.214}\left(\frac{P_{static}\, D_t^4\, \rho_m\, \pi^2}{8\, \dot{m}_m^2}\right)^{0.124}\right]$	20%	25%	$0.183 \leq \frac{\dot{m}_s}{\dot{m}_m} \leq 1.787$ $20{,}690 \leq Re_t \leq 165{,}521$ $0.0001 \leq \frac{P_{static}}{P_{dynamic}} \leq 1.319$ Air and steam mixing	(3.19)

	Empirical Model	MAPE	RSME	Applicability	Equation
Low suction ratio (suction ratio less than one)	$\frac{\dot{m}_s}{\dot{m}_m} = 0.385\left[\left(\frac{A_m}{A_t}\right)^{0.594}\left(\frac{L}{D_s}\right)^{0.03}\left(\frac{\dot{m}_m}{\mu_m D_t}\right)^{-0.075}\left(\frac{\nu_s}{\nu_m}\right)^{1.782}\left(\frac{P_{static}\, D_t^4\, \rho_m\, \pi^2}{8\, \dot{m}_m^2}\right)^{0.09}\right]$	18%	22%	$0.183 \le \frac{\dot{m}_s}{\dot{m}_m} \le 0.797$ $20{,}690 \le Re_t \le 165{,}521$ $0.0001 \le \frac{P_{static}}{P_{dynamic}} \le 0.0825$ Air mixing, air and steam mixing	(3.20)
High suction ratio (suction ratio greater than one)	$\frac{\dot{m}_s}{\dot{m}_m} = 1.79\left[\left(\frac{A_m}{A_t}\right)^{0.624}\left(\frac{L}{D_s}\right)^{0.271}\left(\frac{\dot{m}_m}{\mu_m D_t}\right)^{-0.138}\left(\frac{\nu_s}{\nu_m}\right)^{3.127}\left(\frac{P_{static}\, D_t^4\, \rho_m\, \pi^2}{8\, \dot{m}_m^2}\right)^{0.166}\right]$	5%	6%	$1.157 \le \frac{\dot{m}_s}{\dot{m}_m} \le 2.294$ $20{,}690 \le Re_t \le 41{,}380$ $0.00165 \le \frac{P_{static}}{P_{dynamic}} \le 1.319$ Air mixing, air and steam mixing	(3.21)
Momentum Ratio	$\frac{\rho_s \dot{m}_s}{\rho_m \dot{m}_m} = 3.88\left[\left(\frac{A_m}{A_t}\right)^{0.734}\left(\frac{L}{D_s}\right)^{0.006}\left(\frac{\dot{m}_m}{\mu_m D_t}\right)^{-0.288}\left(\frac{\nu_s}{\nu_m}\right)^{3.17}\left(\frac{P_{static}\, D_t^4\, \rho_m\, \pi^2}{8\, \dot{m}_m^2}\right)^{0.123}\right]$	28%	36%	$0.115 \le \frac{\rho_s \dot{m}_s}{\rho_m \dot{m}_m} \le 2.294$ $20{,}690 \le Re_t \le 165{,}521$ $0.0001 \le \frac{P_{static}}{P_{dynamic}} \le 1.319$ Air mixing, air and steam mixing	(3.22)

	Empirical Model	MAPE	RSME	Applicability	Equation
Dynamic pressure ratio	$\frac{\dot{m}_s D_t^4 \rho_m}{\dot{m}_m D_s^4 \rho_s} = 8.58 \left[\left(\frac{A_m}{A_t}\right)^{-0.626} \left(\frac{L}{D_t}\right)^{1.121} \left(\frac{\dot{m}_m}{\mu_m D_t}\right)^{-0.407} \left(\frac{\nu_s}{\nu_m}\right)^{0.081} \left(\frac{P_{static}\, D_t^4\, \rho_m\, \pi^2}{8\, \dot{m}_m^2}\right)^{0.364} \right]$	48%	56%	$0.00250 \leq \frac{\dot{m}_s{}^2 D_t^4 \rho_m}{\dot{m}_m{}^2 D_s^4 \rho_s} \leq 3.130$ $20{,}690 \leq Re_t \leq 165{,}521$ $0.0001 \leq \frac{P_{static}}{P_{dynamic}} \leq 1.319$ Air mixing, air and steam mixing	(3.23)

3.6.3 Venturi nozzle design guide

Based on the results presented in Section 3.6.2, the suction ratio models (Equations 3.17 – 3.23) can be used to determine the flow rate of a suction fluid into a low-pressure, subsonic Venturi nozzle. There are many commercially available Venturi nozzles [43–46]; however, for subsonic nozzles, it can be difficult to determine which nozzle to select or what suction flow rate to expect from a particular nozzle.

If a particular suction ratio is desired for an application of a subsonic, low-pressure Venturi nozzle, one could find several commercially available nozzle options and plug those geometries into the suction ratio empirical models from Section 3.6.2, along with some operating conditions from the application, and find the geometry that is best suited to deliver the desired suction ratio. Additionally, one could use the empirical models to design a geometry that is ensured to deliver the desired suction ratio, rather than using a commercially available option.

As an example, for a humidification–dehumidification water treatment system, a specific suction ratio of 0.33 may be desired to ensure a maximum amount of water is treated without oversaturating the holding capacity of the air. Given this known suction ratio, the other parameters in the empirical model can be adjusted to inform the design of the nozzle. It is assumed that the ratio of kinematic viscosities is known, and therefore the adjustable dimensionless groups are the area ratio, length ratio, Reynolds number, and pressure ratio. To begin, choose an assumed throat diameter as the throat diameter appears in three of the five dimensionless groups in the suction ratio empirical correlation. Once the throat diameter has been assumed, select a motive mass flow rate. The motive mass flow rate can be calculated if there is a desired velocity in the system after the nozzle, otherwise an approximate value may be assumed. Based on these two selected parameters, the Reynolds number is known as well as the dynamic pressure at the throat of the nozzle. Next, the static pressure at the suction inlet can be determined so the pressure ratio may be fully defined. The static pressure at the suction inlet may be easily defined if the suction inlet is open to ambient pressure. In the case of the humidification–dehumidification example, the pressure is expected to be slightly above ambient pressure as steam is generated in a closed system with the suction inlet being the only opening. Once the Reynold number and pressure ratio terms have been

defined, the remaining terms are only a function of geometry. Next, the motive area can be defined as the area ratio is more impactful than the length ratio. Finally, the length ratio can be defined. This term may be determined by other constraints such as a given suction inlet diameter necessary to connect to another component or a given mixing length to ensure the mixed fluids exit the nozzle at a certain location. Based on these assumptions, an approximate suction ratio can be determined from the empirical models and each parameter adjusted iteratively until the desired suction ratio is achieved. As discussed in Section 3.3, using a head loss calculation to estimate of the suction ratio would yield a suction ratio much too high. Therefore, use of the correlations developed here and presented in Table 3.5 is recommended for design of low-pressure, subsonic Venturi nozzles.

3.7 Conclusions

A study on the effect of geometry and operating conditions on the suction ratio of low-pressure, subsonic Venturi mixing nozzles was conducted. An ANSYS CFD model of the Venturi nozzle mixing was experimentally validated, and then used to calculated nozzle performance over a wide range of geometries and operating conditions. Governing equation calculations and flow head calculations were also used to determine the suction ratio of the experimentally tested nozzles and was found to be very inaccurate in these cases. To determine the suction ratio more accurately, seven potential empirical models were developed to examine the effect of different thermophysical parameters on the suction ratio and identify the parameters most critical to accurate prediction. The foundation for each of the empirical models is the results of a parametric study of nozzle geometry and operating conditions.

The empirical models for suction ratio are more accurate than the empirical models for either momentum ratio or dynamic pressure ratio. For the five suction ratio models developed, the average mean absolute percentage error is 17%. Separating the flow into high-suction ratio and low-suction ratio regimes had the largest impact on the error of the models indicating that the regime change is the most critical aspect of nozzle operation. Based on these results, any of the presented suction ratio empirical models (global, air only, air and steam mixing only, high-suction ratio, or low-suction ratio) can be used to determine the suction ratio of a low-pressure, subsonic Venturi nozzle

within 22%, or a more specific model may be used if the application of the nozzle (low-suction ratio, air only mixing, etc.) with reduced error.

This work can be used to inform the design of low-pressure, subsonic Venturi nozzles for many applications. The suction ratio empirical models are, on average, 34-foldmore accurate than the flow head loss approach. The suction ratio empirical models can be used to determine the suction ratio or nozzle design when precise mixing is required for a given application.

While the correlations proposed in this study provide a good initial design, it will be advantageous to have a secondary tool for a more accurate nozzle design. To that end, these correlations can be used as the basis for physics-guided machine learning algorithms to serve as a more accurate secondary tool for detailed nozzle design and analysis. The authors are in the process of developing such a design tool. The results will be evaluated and published in a follow-up article.

Funding: This research was funded by US Department of Energy, Advanced Research Projects Agency—Energy (ARPA-E) award number DE-AR-0001000.

Acknowledgments: The authors thank ARPA-E for their support of this research.

Nomenclature

dP	Differential pressure drop (Pa)
$\dot{m}$	Mass flow rate (kg/s)
h	Specific enthalpy (J/kg)
V	Velocity (m/s)
P	Pressure (Pa)
A	Area (m^2)
T	Temperature (K)
ρ	Density (kg/m^3)
ω	Humidity ratio
D	Diameter (m)
L	Mixing length (m)
μ	Dynamic viscosity (kg/m·s)
ν	Kinematic viscosity (m^2/s)
Re	Reynolds number
Subscripts	
m	Motive
s	Suction
o	Outlet

References

1. Ariafar, K. Performance evaluation of a model thermocompressor using computational fluid dynamics. Int. J. Mech. 2012, 6, 35–42.

2. Meakhail, T.A.; Zien, Y.; Elsallak, M.; Abdelhady, S. Experimental study of the effect of some geometric variables and number of nozzles on the performance of a subsonic air—Air ejector. Proc. Inst. Mech. Eng. 2008, 222, 809–818.

3. Manzano, J.; Palau, C.V.; Moreira de Azevedo, B.; do Bomfim, G.V.; Vasconcelos, D.V. Characterization and selection method of Venturi injectors for pressurized irrigation. Rev. Ciência Agronômica 2018, 49, 201–210.

4. Bilalis, D.; Karkanis, A.; Savvas, D.; Kontopoulou, C.-K.; Efthimiadou, A. Effects of fertilization and salinity on weed flora in common bean (‘Phaseolus vulgaris’ L.) grown following organic or conventional cultural practices. Aust. J. Crop Sci. 2014, 8, 178–182.

5. Okzan, F.; Ozturk, M.; Baylar, A. Experimental investigations of air and liquid injection by venturi tubes. Water Environ. J. 2006, 20, 114–122.

6. Little, A.B.; Garimella, S. A critical review linking ejector flow phenomena with component- and system-level performance. Int. J. Refrig. 2016, 70, 243–268.

7. Little, A.B.; Bartosiewicz, Y.; Garimella, S. Visualization and validation of ejector flow field with computational and first-principal analysis. J. Fluids Eng. 2015, 137, 1107.

8. Lin, C.; Cai, W.; Li, Y.; Hu, Y.; Giridharan, K. Numerical investigation of geometry parameters for pressure recovery of an adjustable ejector in multi-evaporator refrigeration system. Appl. Therm. Eng. 2013, 61, 649–656.

9. Varga, S.; Oliveira, A.C.; Ma, X.; Omer, S.A.; Zhang, W.; Riffat, S.B. Experimental and numerical analysis of a variable area ratio steam ejector. Int. J. Refrig. 2011, 34, 1668–1675.

10. Sun, D.-W. Variable geometry ejectors and their applications in ejector refrigeration systems. Energy 1996, 10, 919–929.

11. Huang, B.J.; Hu, S.S.; Le, S.H. Development of an ejector cooling system with thermal pumping effect. Int. J. Refrig. 2006, 29, 476–484.

12. Li, X.; Wang, T.; Day, B. Numerical analysis of the performance of a thermal ejector is a steam evaporator. Appl. Therm. Eng. 2010, 30, 2708–2717.

13. Bora, B.J.; Debnath, B.K.; Gupta, N.; Saha, U.K.; Sahoo, N. Investigation on the flow behaviour of a venturi type gas mixer designed for dual fuel diesel engines. Int. J. Emerg. Technol. Adv. Eng. 2013, 3, 202–209.

14. Papadakis, E.; Raptopoulos, F.; Koskinopoulou, M.; Maniadakis, M. On the use of vacuum technology for applied robotic systems. In Proceedings of the 2020 6th International Conference on Mechatronics and Robotics Engineering (ICMRE), Barcelona, Spain, 12–15 February 2020; pp. 73–77.

15. Rodrigues, A.; Camargo, E.; Ciolfi, M. Venturi Tube Application to Improve the Vacuum Assistance for Brake Systems; SAE International: Warrendale, PA, USA, 2013.

16. Xu, J.; Liu, X.; Pang, M. Numerical and experimental studies on transport properties of powder ejector based on double venturi effect. Vacuum 2016, 134, 92–98.

17. Kroll, E.A. The design of jet pumps. Chem. Eng. Prog. 1947, 1, 21–24.

18. Eames, I.W. A new prescription for the design of supersonic jet pumps: The constant rate of momentum change method. Appl. Therm. Eng. 2002, 22, 121–131.

19. Hoggarth, M.L. The design and performance of high-pressure injectors and gas jet boosters. Proc. Inst. Mech. Eng. 1970, 185, 755–766.

20. Munday, J.T.; Bagster, D.F. A new theory applied to steam jet refrigeration. Ind. Eng. Chem. Process Des. Dev. 1997, 16, 442–449.

21. Riffat, S.B.; Everitt, P. Experimental and CFD modeling of an ejector system for vehicle air conditioning. J. Inst. Energy 1999, 72, 41–47.

22. Bartosiewicz, Y.; Aidoun, Z.; Desevaux, P.; Mercadier, Y. Numerical and experimental investigations on supersonic ejectors. Int. J. Heat Fluid Flow 2005, 1, 56–70.

23. Fu, W.; Liu, Z.; Li, Y.; Wu, H.; Tang, Y. Numerical study for the influences of primary steam nozzle distance and mixing chamber throat diameter on steam ejector performance. Int. J. Therm. Sci. 2018, 132, 509–516.

24. Keenan, J.H.; Neumann, E.P. A simple air ejector. ASME J. Appl. Mech. 1942, 62, 75–81.

25. McGovern, R.K.; Narayan, G.P.; Lienhard V, J.H. Analysis of reversible ejectors and definition of an ejector efficiency. Int. J. Therm. Sci. 2012, 54, 153–166.

26. Yang, X.; Long, X.; Yao, X. Numerical investigation on the mixing process in a steam ejector with different nozzle structures. Int. J. Therm. Sci. 2012, 56, 95–106.

27. Ouzzane, M.; Aidoun, Z. Model development and numerical procedure for detailed ejector analysis and design. Appl. Therm. Eng. 2003, 23, 2337–2351.

28. Shin, D.H.; Gim, Y.; Sohn, D.K.; Ko, H.S. Development of venturi-tube with spiral-shaped fin for water treatment. J. Fluids Eng. 2019, 141, 051303.

29. Rudolf, P.; Hudec, M.; Stefan, D. Numerical and experimental investigation of the cavitating flow within venturi tube. J. Fluids Eng. 2019, 141, 1101.

30. Frankel, S. Large eddy simulation of turbulent-cavitation interactions in a venturi nozzle. J. Fluids Eng. 2010, 132, 121301.

31. Sundararaj, S.; Selladurai, V. Numerical and experimental study on jet trajectories and mixing behavior of venturi-jet. J. Fluids Eng. 2010, 132, 101104.

32. Chen, W.; Chong, D.; Yan, J.; Liu, J. The numerical analysis of the effect of geometrical factors on natural gas ejector performance. Appl. Therm. Eng. 2013, 59, 21–29.

33. Hu, J.; Cao, X.; He, H.; Meng, Z.; Ding, M. Numerical optimization on the geometrical factors of subsonic air-air ejector. In Proceedings of the 9th International Symposium on Symbiotic Nuclear Power Systems for 21st Century, Harbin, China, 9–11 July 2018.

34. Maqsood, A. A study of subsonic air-air ejectors with short bent mixing tubes. Diss. Abstr. Int. 2008, 69, 1911.

35. Vaclav, D. Air to air ejector with various divergent mixing chambers. Appl. Mech. Mater. 2014, 493, 50–55.

36. O'Hern, H.; Nikooei, N.; Zhang, X.; Hagen, C.; AuYeung, N.; Tew, D.; Abbasi, B. Reducing the water intensity of hydraulic fracturing: A review of treatment technologies. Desalin. Water Treat. 2021, 221, 121–138.

37. Abbasi, B.; Zhang, X.; O'Hern, H.; Nikooei, E. Method and System for Purifying Contaminated Water. U.S. Patent Application No. 16/985,043, 4 August 2020.

38. Ansys Academic Research Fluent, Release 19.2. Ansys, Canonsburg, PA, USA. Available online: https://www.ansys.com/ academic (accessed on 18 November 2021).

39. Celik, I.B.; Ghia, U.; Roache, P.J.; Freitas, C.J. Procedure for estimation and reporting of uncertainty due to discretization in CFD applications. J. Fluids Eng. 2008, 130, 078001.

40. Cengel, Y.A.; Cimbala, J.M. Fluid Mechanics, Fundamentals and Applications; McGraw-Hill: New York City, NY, USA, 2014.

41. Transtrum, M.K.; Sethna, J.P. Improvements to the Levenberg-Marquardt algorithm for nonlinear least-squares minimization. arXiv 2012, arXiv:1201.5885.

42. Elhashimi, M.; Zhang, X.; Abbasi, B. Empirical prediction of saline water atomization pressure loss and spray phase change using local flow pressure analysis. Desalination 2021, 514, 115156.

43. McMaster-Carr. Available online: https://www.mcmaster.com/venturi/water-aspirator-pumps/ (accessed on 18 November 2021).

44. McMaster-Carr. Available online: https://www.mcmaster.com/venturi/fixed-flow-air-powered-vacuum-pumps-7/ (accessed on 18 November 2021).

45. Steel Venturi Style Pneumatic Air Blower. Grainger, Lakeforest, IL, USA. Available online: https://www.grainger.com/product/ ALLEGRO-Steel-Venturi-Style-Pneumatic-3TCK2 (accessed on 18 November 2021).

46. Aluminum Venturi Nozzle For Blow Gun M 12x1.25 (MT). Tameson, Eindhoven, The Netherlands. Available online: https://tameson.com/pneumatics/air-tools/air-nozzles/venturi/aluminum-venturi-nozzle-for-blow-gun-m-12x1p25-mt.
html?id_currency=4 (accessed on 18 November 2021).

CHAPTER FOUR

Physics-Guided Artificial Neural Networks to Reduce Network Architecture in Multi-Species Mixing Thermal Transport Applications

Hannah O'Hern, Mohammed Elhashimi, Bahman Abbasi*

School of Mechanical, Industrial, and Manufacturing Engineering, Oregon State University, Corvallis, OR 97331, USA,
* Corresponding author

Engineering Applications of Artificial Intelligence

Submitted for peer review

Physics-Guided Artificial Neural Networks to Reduce Network Architecture in Multi-Species Mixing Thermal Transport Applications

Abstract

Artificial neural networks are commonly used in place of traditional hard-computing methods to model the performance of complex systems. When using an artificial neural network, the choice of input parameters and network size are critical to the accuracy of the network as well as its computational intensity. In this work a physics-guided artificial neural network is developed that uses an initial guess of system performance, generated from traditional physics hard-computing models, as one of the input parameters to the network. The physics-guided artificial neural network methodology is applied to three applications of multi-species mixing: gas phase mixing in a Venturi nozzle, air and water flow in a swirling demister , and spray humidification in an airblast atomizer. The physics-guided neural networks are shown to have lower error than a traditional black box network for the same applications and data with smaller network architecture. The physics-guided artificial neural networks discussed in this study can be used to reduce the network error by up to 40%, or reduce the network architecture, or computational intensity, by up to 60% for the same value of error, as compared to traditional black box networks.

4.1 Introduction

Neural networks are commonly used to increase the accuracy of analysis where multiple disciplines of science intersect [1 – 4]. In wastewater treatment applications, the combination of phase change, heat transfer, and fluid dynamics makes system operation very difficult to model accurately using traditional analyses [1, 5].

Artificial neural networks (ANNs) are often used for function approximation because the network will learn the inherent relationships between the input and output parameters without the need for assumptions or rules or relationships that may be unknown or difficult to model [3, 4]. In this way Artificial Intelligence (AI) soft-computing may be better able to solve complex problems than traditional hard-computing based on conservation laws or differential equations [1]. Additionally, ANNs can use noisy or incomplete data sets and can adapt to changes in parameters

through continuous learning [1, 3, 6 – 8]. ANNs are capable of universal approximation or, in other words, can approximate any measurable function to an acceptable level of accuracy [9].

ANNs are composed of three or more layers: one input layer, one or more hidden layers, and one output layer. Each layer is made up of some number of neurons. Each neuron is connected to every neuron in the preceding layer and following layer. The connection between any two neurons has an associated weight. The input layer functions to define the parameter space for the problem and to read in the system data. The output layer corresponds to the unknowns of the system. The neurons in each hidden layer sum the product of the weight and neuron value from the previous layer then pass that summed value through an activation function (Equation 4.1)

$$y = f\left(\sum_{i=1}^{n} w_i x_i\right) \tag{4.1}$$

where *y* is the output value of a given neuron, *f* is the activation function of that neuron, *x* is the input from each of the *n* neurons in the previous layer, and *w* is the weight associated with each of the *n* connections between the given neuron and each neuron in the previous layer. The activation function introduces non-linearity into the networks, allowing ANNs to solve non-linear problems. Additionally, the activation function determines whether a specific neuron "fires." If the sum of the product of input values and weights results in a small value, the activation function will output a very weak output signal. Conversely, if the sum of the products of the inputs and weights is large, the activation function will output a strong signal [1]. The most common activation functions are sigmoid, rectified linear, and hyperbolic tangent. The result of the activation function is the value of the neuron and is fed to the next hidden layer or output layer. Representative neural networks are shown in Figures 4.3, 4.7, and 4.11.

Before the network is trained the weight of each connection is arbitrary. During training, the output layer is calculated using the initial arbitrary weights of the network and the output is compared to a target value of the output. A method called error back-propagation is then used to adjust the weights in the network until a minimum error value is reached. This process is repeated multiple times with the entire training data

set until an acceptable error is attained. During training, the network is tested using data separate from the training data (data the network hasn't seen before) to ensure that the network can predict unknown data as well as the training data. Typically, 70% of a data set is used for training and 30% for testing [1, 3, 4, 6, 10].

AI algorithms are becoming increasingly common in the analysis and optimization of many thermal systems, including energy systems and water treatment technologies. AI is well suited to these types of applications due to their complex nature [11]. In energy systems, ANNs have been applied to many hybrid energy systems, again due to their complex nature, including hybrid photovoltaic (PV) and wind, hybrid PV and thermal solar, and PV-diesel and PV-wind-diesel systems [2]. A geothermal based-organic Rankine cycle with solar system and a geothermal-energy-aided absorption-refrigeration system have both utilized ANNs to predict system performance [10, 12]. ANNs have also been applied to prediction and optimization of energy management in grid and microgrid scales [2]. There are also many applications of ANNs to PV systems for weather and load forecasting as well as system performance [6, 8, 13 – 15]. ANNs have also been used to determine the thermodynamic properties of refrigerants [16, 17]. The most common AI algorithms applied to wastewater treatment are ANNs [18]. ANNs have been used in conjunction with support vector machine and gene expression programming models to predict the presence of trihalomethanes in chlorinated waters and were able to model the non-linear nature of the data with root mean square errors between 3.63 and 4.05 [19]. For an application of removing starch from starchy water using a hydrophilic membrane, ANNs were compared to adaptive neuro-fuzzy interference systems and radial basis functions and all models were found to give similar results for the membrane permeate flux, with the best results obtained with four hidden layers [20]. The effect of four different parameters (flow rate, feed concentration, reaction temperature, and applied voltage) on NaCl removal via electrodialysis has been investigated using ANNs as the system model [21]. A comparison of semi-empirical and ANN models for the prediction of membrane fouling showed that the ANN models could predict the membrane flux more accurately (R^2 = 0.996) for a longer operating time than the semiempirical models [22]. Radial basis function neural networks have also been used for the prediction of temperature

elevation in multi-stage flash desalination plants with low error for newly introduced data. This method has error an order of magnitude lower than that of correlations used for the same purpose [23]. Ensemble machine learning methods have been applied to predict effluent composition from a municipal wastewater treatment plant and a neural network ensemble model was found to provide predictions with up to 24% lower error than non-ensemble methods, however, ensemble machine learning methods increase the computational intensity of the problem [24]. AI algorithms have also been paired with model predictive control to optimize control of municipal wastewater treatment to balance the effluent purity and energy consumption [25]. Multiple optimization strategies, including genetic algorithms and Bayesian optimization, have been used to reduce the error of ANNs in wastewater treatment applications [11, 26]. To the best of our knowledge, the use of analytical models to generate an input parameter to a neural network has not been investigated for any applications.

ANNs have been applied to many complex systems with high levels of accuracy, however, they have important drawbacks. For example, many back-propagation learning schemes are susceptible to finding local error minima rather than the global minimum of the system. For this reason, other AI algorithms, such as genetic algorithms or particle swarm optimization, or statistical methods, such as Gaussian or Bayesian statistics, can be used to train the network rather than typical back-propagation [1, 10, 11, 14, 26]. Error back-propagation is a process where the error of the network is calculated for the given data and the weights of each connection are altered to minimize the error. Back-propagation is still the most common method of ANN training [1, 3, 4, 8, 18, 27]. Another drawback of ANNs is that they are unable to operate outside of the range they are trained for, though by modeling extreme cases (such as rare weather events, etc.) the range of the networks can be expanded [1, 3]. Perhaps the most limiting drawback of ANNs is the amount of data necessary to train a network. The number of data points in a training data set should be at least ten times larger than the number of weights in the network [15, 28]. For networks with small data sets, the size and thus the accuracy of the network is limited. There have been cases involving the use of hard-computing modeling to supplement training data sets and networks can easily be updated as new data becomes available, but there is simply no

getting around the fact that large amounts of data are necessary to sufficiently train such a network [1, 4, 17].

The architecture of a network involves the size of the network: the number of input parameters, the number of hidden layers, the number of neurons in each hidden layer, and the number of output parameters. Any reduction in architecture leads to a reduction in computational cost. It has been established that reducing the number of inputs to a network leads to an increase in the error of the network [13, 15]. The choice of input parameters is critical to the success of the network [1, 3, 12, 13].

Additionally, there have been multiple studies about the number of hidden layers and the number of neurons per hidden layer of a network and their effect on the error of the network [3, 6, 12, 15]. It is widely accepted that the best network architecture is determined via trial and error or prior experience of the network creator [1, 3, 4, 13, 15, 29]. There are a few guidelines in the literature for determining network size. As a rule of thumb, the first hidden layer should have the same number of neurons as the input layer and the number of neurons per layer should decrease toward the output layer [1, 4]. Typically, a single hidden layer is considered to be sufficient for continuous problems, but a second layer may be required for discontinuous problems, such as cases where a single neural network is used to model multiple operating conditions [3, 30]. Only a single hidden layer is necessary for a network to be a universal approximator [9]. However, these guidelines are rarely followed in previous work reported in the literature. Often in practice, the first hidden layer has many more neurons than the number of inputs.

Network architecture is critical to the successful application of the network. There is a tradeoff between network architecture and computational intensity. By combining traditional, statistical neural network and analytical models, the error of the system can be reduced without increasing the network architecture. This combined physics-guided artificial neural network uses hard-computing analytical models to generate an initial guess for the output of the network. That initial guess is provided to the network as an additional network input.

Small-scale, low-pressure Venturi nozzles are difficult to model because losses that would be negligible in the more common high-pressure Venturi nozzles have important

impacts on their performance. Even including various loss terms in governing equation analysis does not yield useable performance predictions for low-pressure Venturi nozzles. These nozzles are relevant to water treatment as well as chemical and pharmaceutical processes and other applications due to their low energy consumption and lack of moving parts [31]. The difficulty of conducting experiments, sensitivity to losses, and the need for highly precise predictions make low-pressure Venturi nozzle a very good candidate to assess our PGANN.

Swirling demisters can be used in humidification-dehumidification water treatment processes to separate treated water from air and gaseous contaminants. In these systems, the water droplets are pushed to the perimeter of the demister by the swirling motion of the air and the treated water is then collected via a small gap along the edge of the demister while the air and gaseous contaminants pass through the center of the demister and are not collected. This component, like high-pressure venturi nozzles, is not usually sensitive to small losses. It was, therefore, selected to test our PGANN in this class of problem and complement the low-pressure Venturi nozzle case study and extends the applicability range of our PGANN.

Humidification-dehumidification is a major field of research in desalination and therefore accurate prediction and optimization of humidification processes is critical to the success of the desalination systems. Existing prediction tools for spray humidification processes is typically based around droplet and bulk liquid analysis. These types of analysis have large fluctuations and are insufficient to pinpoint the thermodynamic state of the humid air [32]. This makes spray humidification a very useful case study for PGANN evaluation. It also helps extend the applicability of model to treatment systems that rely on atomization.

In this work a physics-guided artificial neural network is developed and applied to a Venturi mixing nozzle, a swirl demister, and the mixing of air and water in a spray humidification system. A physics-guided network helps to inform the decision of which input parameters to use in a network as well as reducing the overall network architecture and increasing the accuracy. The quantity of data necessary to train and test artificial neural networks is one of the most important drawbacks to their development and application. Given that the data-to-weight ratio for a network should

always be greater than ten, any reduction in network architecture also helps to reduce the number of data points necessary to sufficiently train the network. The application of the physics-guided artificial neural network methodology to three multi-species mixing applications demonstrates the capability of physics-guided networks to reduce both network error and architecture.

4.2 Methodology and results

This study explores three specific applications to illustrate the efficacy of the proposed physics-guided artificial neural network approach: multi-species gas phase mixing flow in a Venturi nozzle, air and water flow in a swirling demister, and spray evaporation in an airblast atomizer. For each application a black box, or typical, artificial neural network (BBANN) and a physics-guided artificial neural network (PGANN) were developed. The PGANN has all the same inputs as the black box network plus an initial guess of the performance parameter of interest. Each neural network is implemented in Python using existing TensorFlow machine learning libraries [33].

The initial guess input parameter for each system studied was calculated using fundamental governing equations. The Adamax gradient descent optimization method was used to train the networks [34]. A single hidden layer was used with 20% dropout and the sigmoid activation function for all networks. Several activation functions and dropout values were tested, and this combination was found to give the lowest error values. These “hyper-parameters” were held constant for all cases. The number of neurons in the single hidden layer was varied for each application and further analysis was conducted for three network sizes: the case with the largest difference in error between the BBANN and PGANN, the case with the lowest PGANN error, and an average case between the two. For these three network sizes an input parameter reduction study was conducted in order to compare the networks when they have the same number of input parameters.

4.2.1 Venturi mixing nozzle application

For the Venturi nozzle case, the output of each neural network, or the unknown in the system, is the suction ratio of the nozzle. The suction ratio is defined to be the ratio of the suction mass flow rate to the motive mass flow rate. In order to determine the initial guess of the suction flow rate, and thus the suction ratio, for the mixing nozzle, the

continuity, conservation of energy, and conservation of linear momentum equations were used for a control volume drawn such that it cuts through the throat of the nozzle, as well as the suction inlet and outlet of the nozzle. Figure 4.1 shows a labeled cross-section of a representative Venturi mixing nozzle, with the control volume shown. For the cases with air as both the motive and suction fluid, Equations 4.2 – 4.7 were used, where the subscript *m* refers to the motive stream, *s* refers to the suction stream, *o* refers to the mixed outlet stream, and *t* refers to the throat of the nozzle.

$$\dot{m}_m + \dot{m}_s = \dot{m}_o \tag{4.2}$$

$$\dot{m}_m\left(h_t + \frac{1}{2}V_t^2\right) + \dot{m}_s\left(h_s + \frac{1}{2}V_s^2\right) = (\dot{m}_o)\left(h_o + \frac{1}{2}V_o^2\right) \tag{4.3}$$

$$P_{t_{gage}}A_m = \dot{m}_o V_o - \dot{m}_m V_t - \dot{m}_s V_s \tag{4.4}$$

$$\rho_t = f(P_t,\, T_{amb}) \tag{4.5}$$

$$\rho_o = \frac{\dot{m}_m\rho_t + \dot{m}_s\rho_s}{\dot{m}_m + \dot{m}_s} \tag{4.6}$$

$$h_o = f(\rho_o, P_o) \tag{4.7}$$

For the cases with air as the motive fluid and steam as the suction fluid, the psychrometrics of the humid air must be considered. For these cases, Equations. 4.8 – 4.15 were used.

$$\dot{m}_m + \dot{m}_s = \dot{m}_o \tag{4.8}$$

$$\dot{m}_m\left(h_t + \frac{1}{2}V_t^2\right) + \dot{m}_s\left(h_s + \frac{1}{2}V_s^2\right) = (\dot{m}_o)\left(h_o + \frac{1}{2}V_o^2\right) \tag{4.9}$$

$$P_{t_{gage}}A_m = \dot{m}_o V_o - \dot{m}_m V_t - \dot{m}_s V_s \tag{4.10}$$

$$\rho_t = f(P_t,\, T_{amb}) \tag{4.11}$$

$$\rho_o = \frac{\dot{m}_m\rho_t + \dot{m}_s\rho_s}{\dot{m}_m + \dot{m}_s} \tag{4.12}$$

$$h_{air} = f(T_o, P_{atm}), h_{steam} = f(T_o, P_{atm}) \quad (4.13)$$

$$\omega = {\dot{m}_s}/{\dot{m}_m} \quad (4.14)$$

$$h_o = h_{air} + \omega h_{steam} \quad (4.15)$$

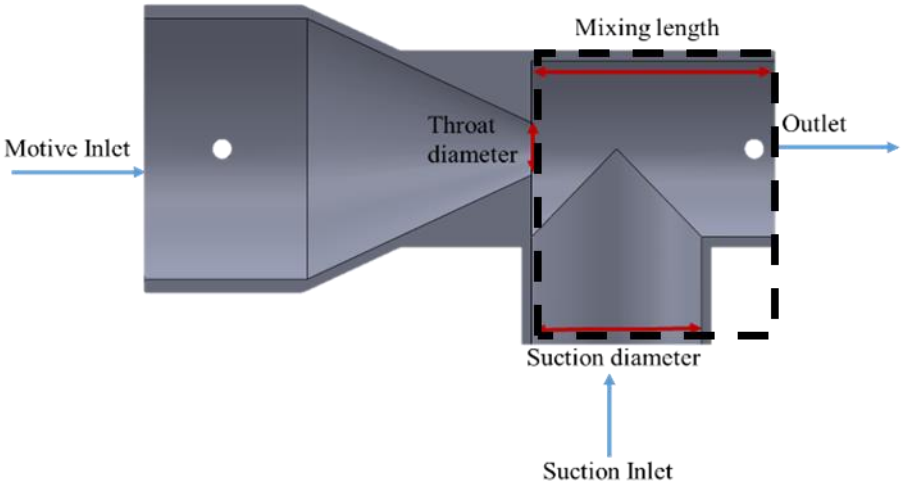

Figure 4.1: Cross-section of representative Venturi mixing nozzle, with control volume denoted by black dashed line.

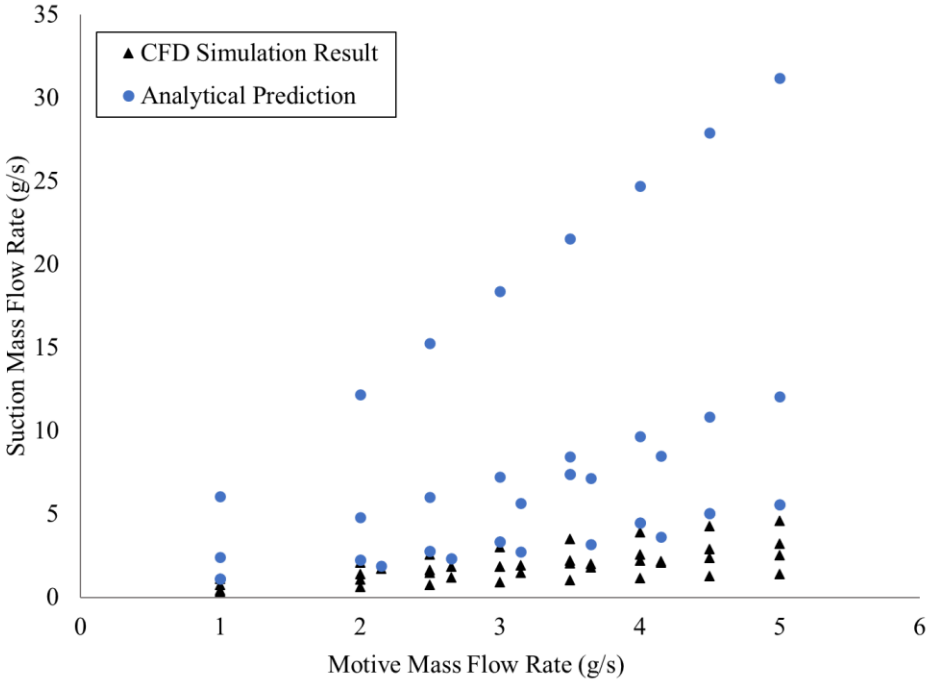

Figure 4.2: Suction mass flow rate as determined by CFD simulation and governing equations versus the motive flow rate. The governing equations overpredict the suction mass flow rate.

The governing equations for the system were solved using Engineering Equation Solver (EES) [35] and presented in an earlier study by the authors [31]. The results of the analytical model and CFD simulation are shown in Figure 4.2. On average this initial guess has an error of 270%, as compared to experimentally validated simulations of six different nozzle geometries with flow rates varying from 1 g/s to 5 g/s, and thus cannot be used to accurately determine the suction ratio of a mixing nozzle. However, this guess can be used as an input to the PGANN in order to reduce the error of the network. The input parameters for the BBANN for the Venturi mixing nozzle are the ratio of motive to throat area, the ratio of mixing length to suction inlet diameter, the Reynolds number at the throat, the ratio of motive fluid to suction fluid kinematic viscosity, and the ratio of static pressure at the suction inlet to the dynamic pressure at the throat and the output is the suction ratio (Equation 4.16).

$$\frac{\dot{m}_s}{\dot{m}_m} = f\left(\frac{A_m}{A_t}, \frac{L}{D_s}, \frac{\dot{m}_m}{\mu_m D_t}, \frac{\upsilon_s}{\upsilon_m}, \frac{P_{static}}{P_{dynamic}}\right) \tag{4.16}$$

The PGANN has the same inputs and output but uses the initial guess ($\frac{\dot{m}_s}{\dot{m}_{m_i}}$) generated by the governing equations as an additional input, as shown in Equation 4.17 and Figure 4.3.

$$\frac{\dot{m}_s}{\dot{m}_m} = f\left(\frac{A_m}{A_t}, \frac{L}{D_s}, \frac{\dot{m}_m}{\mu_m D_t}, \frac{\upsilon_s}{\upsilon_m}, \frac{P_{static}}{P_{dynamic}}, \frac{\dot{m}_s}{\dot{m}_{m_i}}\right) \tag{4.17}$$

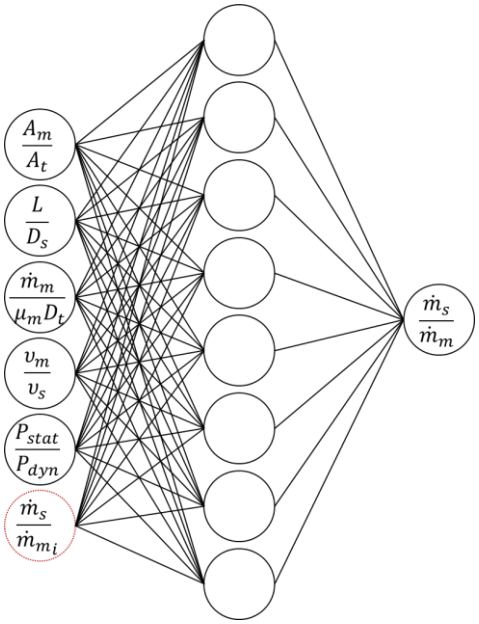

Figure 4.3: Physics-guided neural network for Venturi nozzle mixing with eight representative neurons in the hidden layer. The input parameters shown in solid black circles are present in both the black box and physics-guided networks. The physics-based initial guess input parameter is shown in a dashed red circle as it is only present in the physics-guided artificial neural network.

To develop the networks, 3687 data points were used with 70% of the data used for training and 30% for testing. Experimentally validated simulations and empirical models were used to generate the data set for this application [31]. The number of neurons in the hidden layer was varied from 4 to 22, as shown in Figure 4.4. Regardless of the number of neurons in the hidden layer, the PGANN had lower error than the BBANN. For all cases, the data-to-weight ratio was greater than ten, as recommended [15, 28]. The PGANN had the lowest overall mean squared error (MSE) (1.78%) when there were twenty neurons in the hidden layer. The lowest error for the BBANN (1.89%) also occurred when there were twenty neurons in the hidden layer. As the number of neurons in the hidden layer was reduced, the difference in error between the two networks increased. When there were four neurons in the network, the difference in error between the BBANN and PGANN was the largest (22%). On average, the PGANN had 13% lower error than the BBANN for this application. Based on these results, if a certain error level is acceptable for an application, that error can be achieved with a reduced network architecture if a PGANN is used.

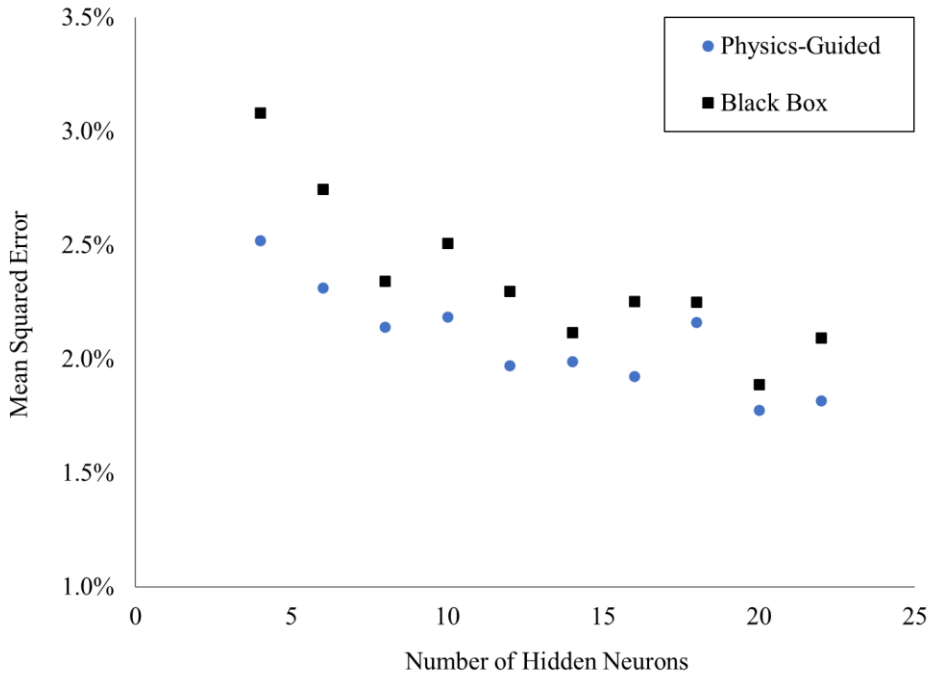

Figure 4.4: Mean squared error of the black box and physics-guided neural networks for the Venturi mixing nozzle as the number of neurons in the hidden layer is changed.

In order for the two networks to have identical architecture, with the same data-to-weight ratio and number of network connections for a direct comparison of the network errors, one input must be removed from the PGANN, such that both networks will have five input parameters. The input parameter reduction study was conducted for three different network configurations: with four neurons in the hidden layer as the configuration has the largest difference between the BBANN and PGANN, with twenty neurons in the hidden layer as this is the configuration with the lowest error, and with twelve neurons as an average configuration.

Each input parameter was removed one at a time, so the PGANN would have five inputs rather than six, to match the BBANN. For all cases, with the exception of the removal of the pressure ratio from the twenty-neuron configuration, the PGANN still had lower error than the BBANN, with the exact same architecture for the three architecture cases considered (Table 4.1). When the initial guess for suction ratio is removed, the error is the same as the BBANN as the networks are identical. The case with all PGANN inputs present has the largest decrease in error between the two networks. For the cases where the area ratio, length ratio, viscosity ratio, and pressure ratio are removed, there is still an increase in accuracy for the PGANN but the improvement is less pronounced. The

choice of input parameters is critical for any application, but these results indicate that PGANNs are less sensitive to input parameter choice than traditional networks. If a system parameter is not included as an input parameter to a PGANN, the network will still be able to accurately predict system performance.

Table 4.1: Venturi mixing physics-guided network mean squared error (MSE) as each input parameter is sequentially removed and comparison to the MSE of the black box network for each configuration.

	Four Neurons (BBANN MSE = 3.08%)		Twelve Neurons (BBANN MSE = 2.30%)		Twenty Neurons (BBANN MSE = 1.89%)	
Removed Input	PGANN MSE (%)	Improvement from black box MSE (%)	PGANN MSE (%)	Improvement from black box MSE (%)	PGANN MSE (%)	Improvement from black box MSE (%)
None	2.52	22	1.97	17	1.78	6
Area Ratio	2.69	14	2.15	7	1.87	1
Length Ratio	2.52	22	1.97	17	1.78	6
Reynolds Number	3.06	1	2.25	2	1.84	3
Viscosity Ratio	2.98	4	2.08	10	1.85	2
Pressure Ratio	3.01	3	2.30	0	2.29	-17

To further investigate the stability of the Venturi nozzle PGANN, a secondary input reduction study was conducted. As the length ratio was determined to be the least important input parameter, it was removed from the PGANN, then each other input parameter (area ratio, Reynolds number, viscosity ratio, and pressure ratio) were sequentially removed and the error for each configuration was recorded. The results of the secondary input reduction study are shown in Table 4.2. In this study with four input parameters to the PGANN, the MSE of the PGANN is still lower than that of the BBANN in all but two cases: the removal of the pressure ratio in the twelve- and twenty-neurons configurations. Again, these results indicate that the addition of a physics-based initial guess lends stability to the PGANN, ensuring low error results if an input parameter is erroneously omitted.

Table 4.2: Venturi mixing physics-guided network mean squared error (MSE) as the length ratio and each additional input parameter are sequentially removed and comparison to the MSE of the black box network for each configuration.

	Four Neurons (BBANN MSE = 3.08%)		Twelve Neurons (BBANN MSE = 2.30%)		Twenty Neurons (BBANN MSE = 1.89%)	
Removed Input in Addition to Length Ratio	PGANN MSE (%)	Improvement from black box MSE (%)	PGANN MSE (%)	Improvement from black box MSE (%)	PGANN MSE (%)	Improvement from black box MSE (%)
None	2.52	22	1.97	17	1.78	6
Area Ratio	2.55	21	2.05	12	1.89	0
Reynolds Number	2.64	17	2.23	3	1.86	1
Viscosity Ratio	2.61	18	2.03	14	1.80	5
Pressure Ratio	2.94	5	2.74	-16	2.75	-31

4.2.2 Swirling demister application

In the case of the swirling demister (Figure 4.5), the parameter of interest is the ratio of the swirl pitch to the demister length [36]. The initial guess for this dimensionless group was calculated using the linear momentum equation to determine the angle at which the water exits the demister and trigonometry relations (Equations 4.18 & 4.19), where *Pitch* is the swirl pitch, *D* is the demister diameter, θ is the angle at which the air enters the demister and ϕ is the swirl angle. The analytical model predicts the ratio of swirl pitch to demister length with 20% error as shown in Figure 4.6.

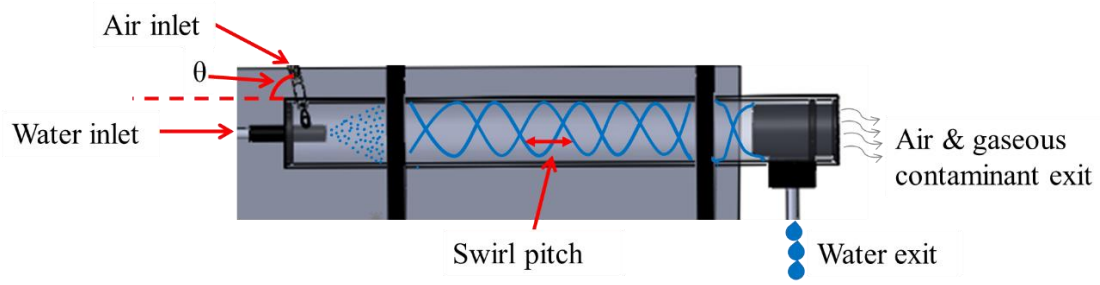

Figure 4.5: Schematic of swirling demister [36].

$$0 = \dot{m}_{water} V_{water_{out}} \cos(\phi) + \dot{m}_{air} V_{air_{out}} \cos(\phi) - \dot{m}_{water} V_{water_{in}} + \dot{m}_{air} V_{air_{in}} \cos(\theta) \quad (4.18)$$

$$Pitch_{swirl} = \frac{D_{demister}}{\tan(\phi)} \tag{4.19}$$

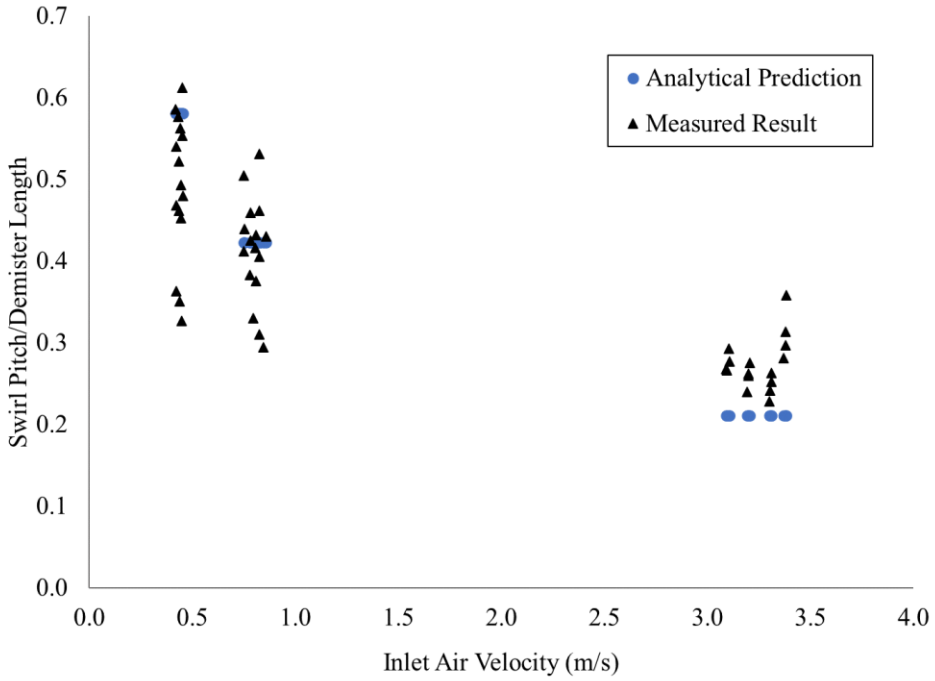

Figure 4.6: Ratio of swirl pitch to tube length as determined analytically and experimentally versus the inlet air velocity. The analytical model predicts the pitch to length ratio with 20% error.

The input parameters for the swirling demister BBANN are the ratio of inlet air velocity to inlet water velocity ($\frac{V_{air_{in}}}{V_{water_{in}}}$), the air injection angle (θ), and the ratio of demister diameter to air outlet diameter ($\frac{D_{demister}}{D_{air\ outlet}}$) (Equation 4.20). The PGANN has the same input parameters as well as the initial guess for swirl pitch to demister length ratio (Equation 4.21 & Figure 4.7).

$$\frac{Pitch_{swirl}}{L_{demister}} = f\left(\frac{V_{air_{in}}}{V_{water_{in}}}, \theta, \frac{D_{demister}}{D_{air\ outlet}}\right) \tag{4.20}$$

$$\frac{Pitch_{swirl}}{L_{demister}} = f\left(\frac{V_{air_{in}}}{V_{water_{in}}}, \theta, \frac{D_{demister}}{D_{air\ outlet}}, \frac{Pitch_{swirl}}{L_{demister\ i}}\right) \tag{4.21}$$

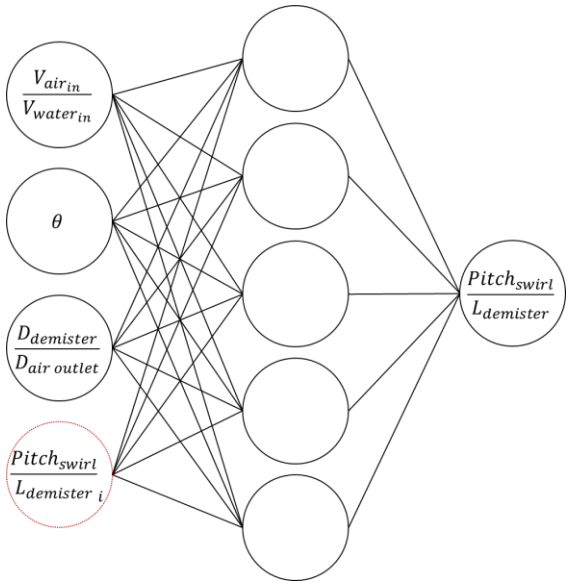

Figure 4.7: Physics-guided neural network for the swirling demister with five representative neurons in the hidden layer. The input parameters shown in solid black circles are present in both the black box and physics-guided networks. The physics-based initial guess input parameter is shown in a dashed red circle as it is only present in the physics-guided artificial neural network.

To train and test the swirling demister neural networks, 3984 data points were used, with 70% used to train the networks and 30% to test them. Experimental data and an empirical model were used to generate part of the data set [36]. The number of neurons in the hidden layer was varied between four and twenty-two. For all network configurations, the PGANN had lower error than the BBANN, as shown in Figure 4.8. The PGANN configuration with twenty neurons in the hidden layer had the lowest mean squared error (5.67%) of the PGANN cases, and thus the lowest overall error including the BBANN cases. For the configurations with four and twenty neurons, there was the largest difference in error between the BBANN and the PGANN (40%). Among the BBANN cases the lowest error (7.94%) occurred with four neurons in the hidden layer. The average improvement in error for the PGANN across all network configurations for this application was 33%.

The network reduction study was conducted for the four neuron, twelve neuron, and twenty neuron configurations, as shown in Table 4.3. When the velocity ratio term was removed from the twelve and twenty neuron configurations, the mean squared error of the PGANN was higher than the BBANN. Removal of the diameter ratio did not impact the error of the PGANN for any configuration. The velocity ratio was the most

important term in the swirling demister networks, as its removal had the largest impact on the overall error of the network.

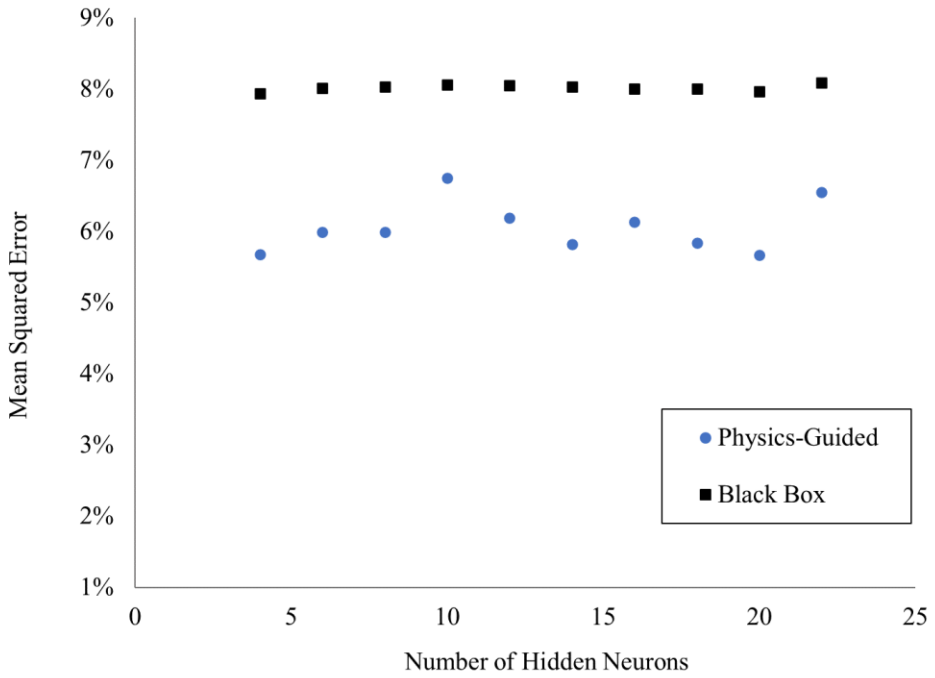

Figure 4.8: Mean squared error of the black box and physics-guided neural networks for the swirling demister application as the number of neurons in the hidden layer is changed.

Table 4.3: Swirling demister physics-guided network mean squared error (MSE) as each input parameter is sequentially removed and comparison to the MSE of the black box network for each configuration.

	Four Neurons (BBANN MSE = 7.94%)		Twelve Neurons (BBANN MSE = 8.05%)		Twenty Neurons (BBANN MSE = 7.97%)	
Removed Input	PGANN MSE (%)	Improvement from black box MSE (%)	PGANN MSE (%)	Improvement from black box MSE (%)	PGANN MSE (%)	Improvement from black box MSE (%)
None	5.68	40	6.19	30	5.67	40
Velocity Ratio	7.94	0	10.65	-24	11.55	-31
Injection Angle	6.56	21	6.80	18	7.22	10
Diameter Ratio	5.68	40	6.19	30	5.67	40

4.2.3 Spray humidification application

For the spray humidification application (Figure 4.9) [32], the humidity ratio of the air leaving the humification system is the system parameter of interest. This value is difficult to determine via analytical methods because the state of the water in the spray nozzle cannot be fully defined. The analytical model for this system (Equations 4.22 – 4.24) is based on the assumption that there is 100% efficient heat transfer between the hot air and relatively cool water streams entering the spray nozzle. This analytical model overpredicts the actual humidity ratio by 617% on average (Figure 4.10) and therefore is not suitable as a standalone model for the system but can still be used to generate initial guesses for the PGANN.

$$\Delta T = T_{air} - T_{water} \tag{4.22}$$

$$\dot{m}_{air} c_{P_{air}} \Delta T = \dot{m}_{steam} c_{P_{steam}} \Delta T \tag{4.23}$$

$$\omega = {\dot{m}_{steam}}/{\dot{m}_{air}} \tag{4.24}$$

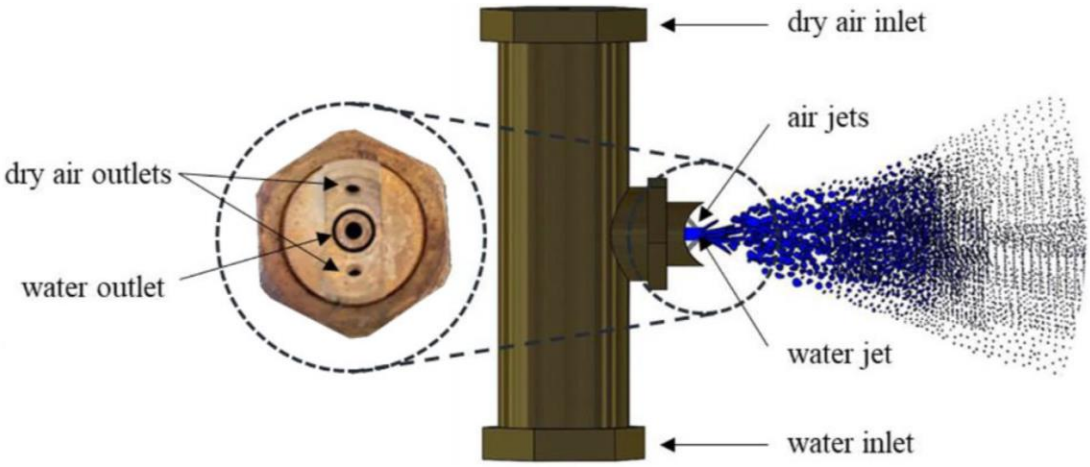

Figure 4.9: Schematic of atomization through an external-mixing atomizer [32].

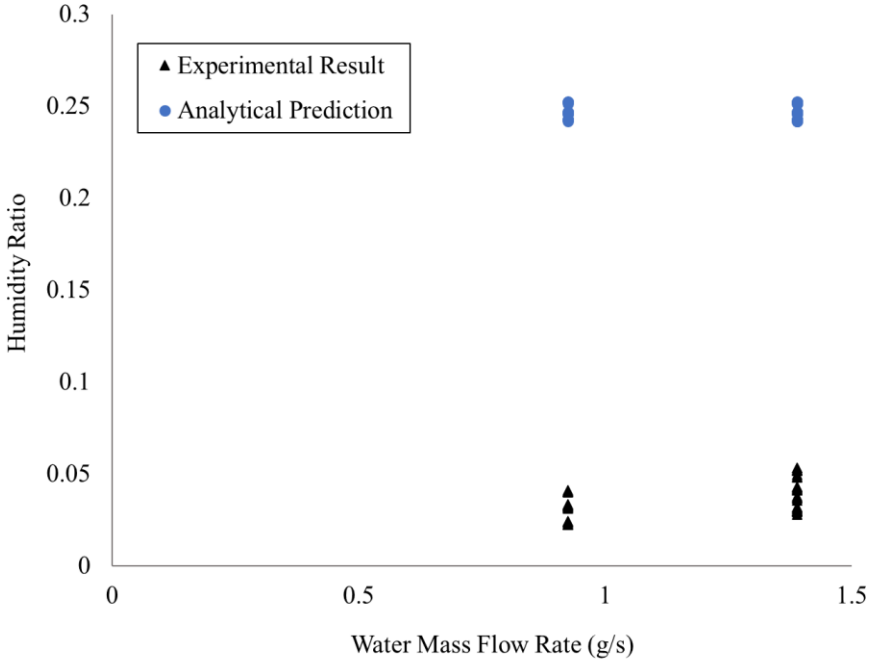

Figure 4.10: Humidity ratio as determined experimentally and analytically versus the water mass flow rate. The analytical model greatly overpredicts the humidity ratio but still provides a useful input to the PGANN.

The input parameters for the BBANN for the spray humidification application are a modified Jakob number (first term), the Lewis number (second term), the ratio of axial distance from the atomizer orifice to the spray diameter at that location, or geometric ratio (third term), the Reynolds number based on the total flow rate and effective atomizer diameter (fourth term), and the ratio of air mass flow rate to water mass flow rate, or mass ratio (fifth term) (Equations 4.25 & 4.26).

$$\omega = \frac{\dot{m}_v}{\dot{m}_a} = f\left(\frac{c_P(T_a - T_w)}{h_{lv}}, \frac{\alpha}{\mathfrak{D}}, \frac{x}{D}, \frac{4(\dot{m}_a + \dot{m}_w)}{\pi\, D_{atom}\, \mu_{avg}}, \frac{\dot{m}_a}{\dot{m}_w}\right) \tag{4.25}$$

$$\omega = \frac{\dot{m}_v}{\dot{m}_a} = f\left(Ja_{mod}, Le, \frac{x}{D}, Re_D, \frac{\dot{m}_a}{\dot{m}_w}\right) \tag{4.26}$$

The PGANN has the same inputs and output but uses the initial guess (ω_i) generated by the governing equations as an additional input, as shown in Equation 4.27 and Figure 4.11.

$$\omega = \frac{\dot{m}_v}{\dot{m}_a} = f\left(Ja_{mod}, Le, \frac{x}{D}, Re_D, \frac{\dot{m}_a}{\dot{m}_w}, \omega_i\right) \tag{4.27}$$

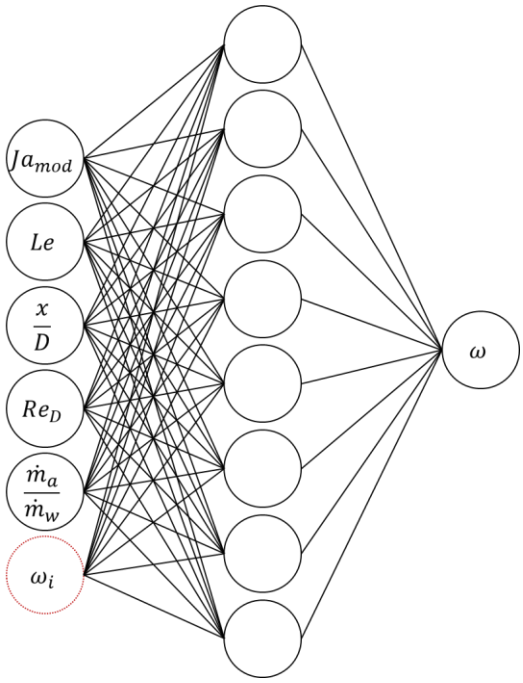

Figure 4.11: Physics-guided neural network for spray humidification with eight representative neurons in the hidden layer. The input parameters shown in solid black circles are present in both the black box and physics-guided networks. The physics-based initial guess input parameter is shown in a dashed red circle as it is only present in the physics-guided artificial neural network.

To train and test the BBANN and PGANN for this application, 3780 data point were used, with 70% for training and 30% for testing. Empirical models were used to generate this data set [32]. The number of neurons in the hidden layer was varied from 4 to 22, as shown in Figure 4.12. The PGANN had lower error than the BBANN for each network configuration. The lowest error for the BBANN (2.33%) occurred when there were 20 neurons in the network. The PGANN had an error of 2.33% with only four neurons in the hidden layer. The lowest error for the PGANN (2.31%) occurred with 18 neurons in the hidden layer. With four neurons in the hidden layer the difference in error between the PGANN and BBANN is the largest at 17%. The average improvement in error across all network configurations is 5%.

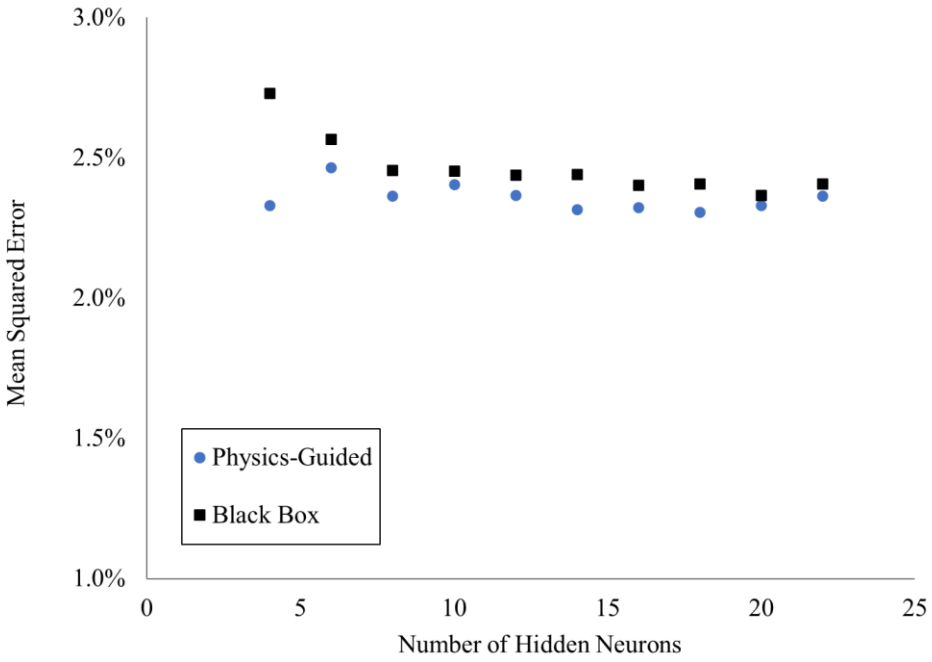

Figure 4.12: Mean squared error of the black box and physics-guided neural networks for the spray humidification application as the number of neurons in the hidden layer is changed.

As with the previous test cases, to compare the networks with the same number of input parameters, an input parameter reduction study was conducted. The input parameter reduction study was conducted on three different network configurations: with four neurons in the hidden layer as this case has the largest difference in error between the BBANN and PGANN, with eighteen neurons in the hidden layer as this case has the lowest error for the PGANN, and with twelve neurons in the hidden layer as an average case. Each input parameter was sequentially removed, both to determine the relative importance of each term and to investigate the effect of the PGANN on error when the number of input parameters is the same between the PGANN and BBANN.

Table 4.4: Spray humidification physics-guided network mean squared error (MSE) as each input parameter is sequentially removed and comparison to the MSE of the black box network for each configuration.

	Four Neurons (BBANN MSE = 2.73%)		Twelve Neurons (BBANN MSE = 2.44%)		Eighteen Neurons (BBANN MSE = 2.41%)	
Removed Input	PGANN MSE (%)	Improvement from black box MSE (%)	PGANN MSE (%)	Improvement from black box MSE (%)	PGANN MSE (%)	Improvement from black box MSE (%)
None	2.33	17	2.37	3	2.31	3
Jakob Number	2.51	9	2.41	2	2.32	2
Lewis Number	2.44	12	2.65	-8	2.70	-12
Geometric Ratio	2.72	0	2.67	-9	2.62	-9
Reynolds Number	7.55	-64	7.32	-67	7.28	-67
Mass ratio	4.20	-35	2.94	-17	2.92	-19

Table 4.4 shows the results of the input parameter reduction study for the spray humidification case. In this case the Jakob number was found to be the least important input parameter and the Reynolds number was found to be the most important parameter. For all three network configurations, if the Reynolds number is removed, the error increases significantly. For all cases, the error of the PGANN is still lower than that of the BBANN with the same input parameter removed, but the inclusion of an initial guess for the humidity ratio does not have a significant impact on the result of the network. The initial guess of the PGANN increases the accuracy of the network slightly but cannot overcome the significant dependence on the Reynolds number which has the largest impact on error. Given the significant dependence of both the PGANN and BBANN on the Reynolds number for this application, an input parameter reduction study was also conducted on the empirical model used to help expand the network data set [35]. It was found that removing the Reynolds number from the empirical model and re-optimizing the model results in a 101% increase in error. These results indicate that the Reynolds number is a critical parameter in the prediction of the humidity ratio for spray humidification, regardless of the prediction method (i.e., empirical model, ANN, etc.).

In the case of the spray humidification, the physics-guided network was significantly more dependent on the Reynolds number than the analytical solution for the humidity ratio. For this case, the error of the physics-guided network with reduced inputs was

greater than that of the black box network in almost all cases, however, if the black box network has the same input parameter removed, the physics-guided network will have lower error. The inclusion of the physics-guided input parameter creates a more stable network such that if a parameter is accidentally omitted, the error of the network may still acceptable. However, changes in error are dominated by the Reynolds number and changes to any other input parameters has a relatively small impact on the error of the system. PGANNs can decrease the error of a system when all input parameters are of relatively equal importance but if there is one term with significantly higher system importance, the inclusion of an initial guess is less impactful. Future work is necessary to further study the lack of dependency on the initial guess in the case of the spray humification PGANN.

4.3 Conclusions

Physics-guided artificial neural networks, as well as black box networks, were developed to determine the benefits of adding an analytical initial guess as an input parameter to the neural network. The physics-guided artificial neural network methodology was applied to three multi-species mixing systems that are applicable to wastewater treatment; specifically to find the suction ratio of a Venturi mixing nozzle, the swirl pitch to demister length ratio for a swirling demister, and humidity ratio of a spray humidification system. The physics-guided network had lower mean squared error than the typical black box network for all network sizes for each applications studied.

In the case of the Venturi mixing nozzle, even when input parameters are removed so the two network types have the same number of input parameters, the physics-guided network has lower error for all cases but one: the removal of the pressure ratio from the twenty-neuron configuration. Additionally, when two input parameters are removed, the physics-guided network has lower mean squared error in all cases but two. These results indicate that physics-guided artificial neural networks can be used to reduce the error and complexity of a network. Additionally, if an input parameter is accidentally left out of a network, physics-guided networks will maintain their high accuracy in almost all cases, making the choice of input parameters less critical to the success of the network.

In the case of the swirling demister, the PGANN has lower error than the BBANN, by 33% on average. In the input parameter reduction study, the PGANN still had lower error than the BBANN in all cases except for the removal of the velocity ratio from the twelve and twenty neuron configurations. The swirl pitch is a strong function of the velocity ratio.

In the case of spray humidification, the Reynolds number was identified as the most critical parameter for the success of predicting the humidity ratio. The inclusion of a physics-guided initial guess does not change the significant dependence on the Reynolds number. The PGANN does slightly outperform the BBANN in this case in terms of error and can therefore be used to reduce the network size.

The physics-guided network has lower error for every network configuration and application if all input parameters are present. Thus, if a certain error is acceptable for a given application, the physics-guided network can be used to achieve that error at a smaller network size and computational cost. Physics-guided artificial neural networks can be used to reduce the network error by up to 40% for the same network architecture, or reduce the network architecture, or computational intensity, by up to 60% for the same value of error.

When input parameters are removed from the PGANN such that it has the same number of input parameters as the BBANN, the PGANN still has lower error than the BBANN in the vast majority of cases examined. In the cases where a critical parameter is removed, the PGANN has higher error than the BBANN. In each application there is at least one critical parameter that, when removed, increases the error of the PGANN to above that of the BBANN. Therefore, the addition of a physics-guided initial guess is helpful to the error and stability of a given neural network, but cannot be used to replace important system parameters, and instead should be used to supplement logical system parameters. This shows that ANN is a powerful computational tool, but not a substitute for fundamental understanding and formulation of the physics of a process. When correct physical characterization and a first order governing equation analysis are paired with an ANN, it can produce the most reliable and computationally efficient predictions.

Future work on this topic is necessary to fully determine the capabilities of the physics-guided artificial neural network methodology. This method must be applied to further applications in the topic of multi-species mixing, as well as other processes. The difference in error between the PGANN and BBANN increases as the error of the initial guess decreases, so further work to characterize at what error the initial guess becomes less impactful should be conducted. Additionally, cases with multiple output parameters of interest should be studied to determine if a single physics-based initial guess is sufficient for multiple network outputs or if each output parameter should have an initial guess as an input parameter.

Nomenclature

y	Output value of a given neuron
f	Activation function
x_i	Input from ith neuron in previous layer
w_i	Weight of connection between given neuron and ith neuron in previous layer
$\dot{m}$	Mass flow rate (kg/s)
h	Enthalpy (J/kg)
V	Velocity (m/s)
P	Pressure (Pa)
ρ	Density (kg/m^3)
ω	Humidity ratio
A	Area (m^2)
L	Distance between nozzle throat and outlet (m)
D	Diameter (m)
μ	Viscosity (kg/m·s)
ν	Kinematic viscosity (m^2/s)
T	Temperature (K)
c_P	Specific heat (J/kg·K)
Re	Reynolds number
Ja_{mod}	Modified Jakob number
x	Distance from atomizer outlet
Le	Lewis number
$\mathfrak{D}$	Binary diffusion coefficient of water vapor and air
$Pitch$	Swirl pitch in demister (m)
Subscripts	
m	Venturi nozzle motive inlet
s	Venturi nozzle suction inlet
o	Venturi nozzle outlet
t	Venturi nozzle throat
a	Dry air

w	Liquid water
$atom$	Effective atomizer
v	Water vapor
$swirl$	In swirling demister
i	Physics-based initial guess

References

1. Yang, K.-T.: Artificial Neural Networks (ANNs): A New Paradigm for Thermal Science and Engineering. Journal of Heat Transfer. 130, (2008). https://doi.org/10.1115/1.2944238

2. Zahraee, S.M., Khalaji Assadi, M., Saidur, R.: Application of Artificial Intelligence Methods for Hybrid Energy System Optimization. Renewable and Sustainable Energy Reviews. 66, 617–630 (2016). https://doi.org/10.1016/j.rser.2016.08.028

3. Rafiq, M.Y., Bugmann, G., Easterbrook, D.J.: Neural network design for engineering applications. Computers & Structures. 79, 1541–1552 (2001). https://doi.org/10.1016/S0045-7949(01)00039-6

4. Krarti, M.: An Overview of Artificial Intelligence-Based Methods for Building Energy Systems. Journal of Solar Energy Engineering. 125, 331–342 (2003). https://doi.org/10.1115/1.1592186

5. O'Hern, H., Nikooei, E., Zhang, X., Hagen, C., Auyeung, N., Tew, D., Abbasi, B.: Reducing the water intensity of hydraulic fracturing: a review of treatment technologies. Desalination and Water Treatment. 221, 121–138 (2021). https://doi.org/10.5004/dwt.2021.27026

6. Yaïci, W., Entchev, E.: Performance prediction of a solar thermal energy system using artificial neural networks. Applied Thermal Engineering. 73, 1348–1359 (2014). https://doi.org/10.1016/j.applthermaleng.2014.07.040

7. Ng, B.C., Darus, I.Z.M., Jamaluddin, H., Kamar, H.M.: Application of adaptive neural predictive control for an automotive air conditioning system. Applied Thermal

Engineering. 73, 1244–1254 (2014). https://doi.org/10.1016/j.applthermaleng.2014.08.044

8. Kalogirou, S.: Applications of artificial neural-networks for energy systems. Applied Energy. 67, 17–35 (2000)

9. Hornik, K., Stinchcombe, M., White, H.: Multilayer feedforward networks are universal approximators. Neural Networks. 2, 359–366 (1989). https://doi.org/10.1016/0893-6080(89)90020-8

10. Khosravi, A., Syri, S., Zhao, X., Assad, M.E.H.: An artificial intelligence approach for thermodynamic modeling of geothermal based-organic Rankine cycle equipped with solar system. Geothermics. 80, 138–154 (2019). https://doi.org/10.1016/j.geothermics.2019.03.003

11. al Aani, S., Bonny, T., Hassan, S.W., Hilal, N.: Can machine language and artificial intelligence revolutionize process automation for water treatment and desalination? Desalination. 458, 84–96 (2019)

12. Tugcu, A., Arslan, O.: Optimization of geothermal energy aided absorption refrigeration system—GAARS: A novel ANN-based approach. Geothermics. 65, 210–221 (2017). https://doi.org/10.1016/j.geothermics.2016.10.004

13. Yaïci, W., Longo, M., Entchev, E., Foiadelli, F.: Simulation Study on the Effect of Reduced Inputs of Artificial Neural Networks on the Predictive Performance of the Solar Energy System. Sustainability. 9, 1382 (2017). https://doi.org/10.3390/su9081382

14. Ogliari, E., Grimaccia, F., Leva, S., Mussetta, M.: Hybrid Predictive Models for Accurate Forecasting in PV Systems. Energies (Basel). 6, 1918–1929 (2013). https://doi.org/10.3390/en6041918

15. Grimaccia, F., Leva, S., Mussetta, M., Ogliari, E.: ANN Sizing Procedure for the Day-Ahead Output Power Forecast of a PV Plant. applied sciences. 7, (2017)

16. Sözen, A., Özalp, M., Arcaklioğlu, E.: Calculation for the thermodynamic properties of an alternative refrigerant (R508b) using artificial neural network. Applied Thermal Engineering. 27, 551–559 (2007). https://doi.org/10.1016/j.applthermaleng.2006.06.003

17. Chouai, A., Laugier, S., Richon, D.: Modeling of thermodynamic properties using neural networks. Fluid Phase Equilibria. 199, 53–62 (2002). https://doi.org/10.1016/S0378-3812(01)00801-9

18. Bhagat, S.K., Tung, T.M., Yaseen, Z.M.: Development of artificial intelligence for modeling wastewater heavy metal removal: State of the art, application assessment and possible future research. Journal of Cleaner Production. 250, 119473 (2020). https://doi.org/10.1016/j.jclepro.2019.119473

19. Singh, K.P., Gupta, S.: Artificial intelligence based modeling for predicting the disinfection by-products in water. Chemometrics and Intelligent Laboratory Systems. 114, 122–131 (2012). https://doi.org/10.1016/J.CHEMOLAB.2012.03.014

20. Sargolzaei, J., Haghighi Asl, M., Hedayati Moghaddam, A.: Membrane permeate flux and rejection factor prediction using intelligent systems. Desalination. 284, 92–99 (2012). https://doi.org/10.1016/J.DESAL.2011.08.041

21. Jing, G., Du, W., Guo, Y.: Studies on prediction of separation percent in electrodialysis process via BP neural networks and improved BP algorithms. Desalination. 291, 78–93 (2012). https://doi.org/10.1016/J.DESAL.2012.02.002

22. Ghandehari, S., Montazer-Rahmati, M.M., Asghari, M.: A comparison between semi-theoretical and empirical modeling of cross-flow microfiltration using ANN. Desalination. 277, 348–355 (2011). https://doi.org/10.1016/J.DESAL.2011.04.057

23. Aminian, A.: Prediction of temperature elevation for seawater in multi-stage flash desalination plants using radial basis function neural network. Chemical Engineering Journal. 162, 552–556 (2010). https://doi.org/10.1016/J.CEJ.2010.05.060

24. Nourani, V., Elkiran, G., Abba, S.I.: Wastewater treatment plant performance analysis using artificial intelligence - an ensemble approach. Water Science & Technology. 78, 2064–2076 (2018)

25. Bernardelli, A., Marsili-Libelli, S., Manzini, A., Stancari, S., Tardini, G., Montanari, D., Anceschi, G., Gelli, P., Venier, S.: Real-time model predictive control of a wastewater treatment plant based on machine learning. Water Science & Technology. 81, 2391–2400 (2020)

26. Li, D., Yang, H.Z., Liang, X.F.: Prediction analysis of a wastewater treatment system using a Bayesian network. Environmental Modelling & Software. 40, 140–150 (2013)

27. Haffejee, R.A., Laubscher, R.: Application of machine learning to develop a real-time air-cooled condenser monitoring platform using thermofluid simulation data. Energy and AI. 3, (2021)

28. Baum, E.B., Haussler, D.: What Size Net Gives Valid Generalization? Neural Computation. 1, 151–160 (1989). https://doi.org/10.1162/neco.1989.1.1.151

29. Kemp, S.J., Zaradic, P., Hansen, F.: An approach for determining relative input parameter importance and significance in artificial neural networks. Ecological Modelling. 204, 326–334 (2007). https://doi.org/10.1016/j.ecolmodel.2007.01.009

30. Bansal, Y., Ertekin, T., Karpyn, Z., Ayala, L., Nejad, A., Suleen, F., Balogun, O., Liebmann, D., Sun, Q.: Forecasting Well Performance in a Discontinuous Tight Oil Reservoir Using Artificial Neural Networks. Society of Petroleum Engineers - SPE USA Unconventional Resources Conference 2013. 239–250 (2013). https://doi.org/10.2118/164542-MS

31. O'Hern, H., Murphy, T., Zhang, X., Liburdy, J., Abbasi, B.: A Design Method for Low-Pressure Venturi Nozzles. Applied Mechanics. 3, 390–411 (2022). https://doi.org/10.3390/applmech3020024

32. Elhashimi, M., Zhang, X., Abbasi, B.: Empirical prediction of saline water atomization pressure loss and spray phase change using local flow pressure analysis. Desalination. 514, (2021)

33. Abadi, M., Barham, P., Chen, J., Chen, Z., Davis, A., Dean, J., Devin, M., Ghemawat, S., Irving, G., Isard, M., Kudlur, M., Levenberg, J., Monga, R., Moore, S., Murray, D.G., Steiner, B., Tucker, P., Vasudevan, V., Warden, P., Wicke, M., Yu, Y., Zheng, X., Brain, G.: TensorFlow: A System for Large-Scale Machine Learning, https://tensorflow.org., (2016)

34. Adamax: https://keras.io/api/optimizers/adamax/

35. Klein, S.A.: Engineering Equation Solver (EES), (2021)

36. Anderson, K., Zhang, X., Abbasi, B.: A Method to Design and Optimize Axial Flow Cyclones for Gas–Liquid Separation. Journal of Fluids Engineering. 143, (2021). https://doi.org/10.1115/1.4050638

CHAPTER FIVE
Conclusions

In this chapter the work from Chapters Two, Three, and Four are summarized and a comparison of the various modelling methods used throughout the work is presented. Additionally, future work and applications of the physics-guided artificial neural network framework are outlined.

Three research goals were identified to evaluate the work described in this dissertation. The first research goal was to identify common parameters among existing thermal wastewater treatment methods such that a new model can be developed based on the common parameter space to accurately model hydraulic fracturing wastewater treatment for a number of technologies. This research goal was addressed in Chapter Two. The literature review undertaken of hydraulic fracturing wastewater as well as its management and treatment helped to inform the design of possible novel treatment systems, to identify the parameters critical to the successful treatment of hydraulic fracturing wastewater regardless of the treatment technology, and to identify the need for very accurate system models to predict the real time performance of these complex treatment technologies.

The second research goal was to develop empirical models for a component that is not well characterized analytically to provide a design guide for applications that need precise measurement or control of the mixing ratio, such as selective condensation of water from a muti-species gaseous flow. In order to address this goal, the work discussed in Chapter Three was completed. It was determined that the suction ratio of low-pressure Venturi nozzles can be determined analytically with 270% error. This method is insufficiently accurate to use in analysis of a wastewater treatment system involving low-pressure Venturi nozzles. To develop more accurate models for low-pressure Venturi nozzles, CFD simulations of the process were experimentally validated and used to conduct a parametric study of 109 cases over 15 different geometries. The results of the parametric study were used to develop empirical models which are all at least twice as accurate as the analytical model. These empirical models can be used to design low-pressure Venturi nozzles. Despite the significant improvement in error between the empirical and analytical models, the empirical

models are still insufficiently accurate to be used for real-time modeling and control of wastewater treatment systems. Thus, a different modeling method was adopted in an attempt to further reduce the model error.

The final research goal addresses the need for more accurate modeling methods: develop framework for physics-guided artificial neural networks and characterize change in network performance between black box and physics-guided artificial neural networks using various components relevant to wastewater treatment systems. This research goal is addressed in Chapter Four wherein the concept of a physics-guided artificial neural network is described and evaluated on three cases. For all cases the artificial neural networks have sufficiently low error to be incorporated in a real-time system model for hydraulic fracturing wastewater treatment applications. The error of these networks can be further reduced using a physics based initial guess as an input parameter in physics-guided artificial neural networks. The physics-guided artificial neural network framework can reduce both the error and computational cost of the model. The limitation of the physics-guided network framework is that it cannot be used to overcome the physics of the system, evidenced by other input parameters, such as the Reynolds number or ratio of static pressure to dynamic pressure, having a larger impact on the error of the network than the physics based initial guess. The range of cases studied provides a strong indication that the physics-guided network developed in this research can be applied to wastewater treatment and many other thermal-fluids applications, irrespective of the specific technology, as long as the network is supplied with correct input parameters based on the physics of the system, as well as a physics-guided initial guess.

Four types of models have been used in this work: CFD, analytical, experimentally-driven empirical, and neural network. Each type of model was applied to the case of low-pressure Venturi nozzles. The CFD model predicted the suction ratio within 11% but is the most computationally intensive model of those considered. Using a computer with 40 parallel processors with a base speed of 2.6 GHz the suction ratio of a single nozzle can be found in approximately one hour. Physics-guided artificial neural network models can produce predictions for Venturi nozzle suction ratio within one minute, using four parallel processors with a base speed of 2.5 GHz. The normalized

computational intensity can be found by calculating the product of the number of processors, the base speed, and the computational time. The normalized computational intensity of the physics-guided network model is approximately 624 times lower than that of the CFD model. The analytical model had the highest error: 270%. The empirical models had error of 22% and the physics-guided network had error of 2%. The physics-guided network model takes significant time to train and test before it can be used, but once trained can be used to quickly find the suction ratio with very low error for any case supplied to it. Functionally, for a single component the computational intensity of the analytical, empirical, and physics-guided network models is similar, however, for more complicated systems the differences in computational cost will be more pronounced. The results of the black box artificial neural network are five times more accurate than the CFD results and can be found with 624 times less normalized computational intensity. The black box and physics-guided artificial neural networks have comparable computational intensity, but the physics-guided network is, on average, 13% more accurate than the black box network for the case of the low-pressure Venturi nozzle.

Though artificial neural network models have much lower normalized computational intensity than CFD simulations, the CFD simulations provide much more information than the artificial neural network models. The neural networks can only provide the output information they are trained to predict. On the other hand, CFD models can provide detailed information about any particular problem, as well as information about the velocity profile, species transport, etc. If one knows the exact information they want from a model and need to calculate that information repeatedly, the lower computational intensity of the neural network models makes them the ideal modeling tool. However, if one needs additional detailed spatial analysis, gradients, other detailed or granular information, or only needs information about a few cases, CFD models can provide more information without the need for training and testing of the model, as is necessary in neural network models.

In this work, the concept of physics-guided artificial neural networks has been proven for multiple components used in larger wastewater treatment technologies, however, there is still significant future work necessary to further understand the limitations and

capabilities of the physics-guided network framework. First, for all cases considered a single hidden layer was used, as recommended by the literature. For more complicated processes, such as full treatment systems rather than individual components, additional hidden layers may be necessary. For cases with multiple hidden layers further architecture changes for the physics-guided networks should be investigated. It may be the case that fewer hidden layers are required for physics-guided networks than for black box networks. Second, a physics-guided neural network should be applied to a selective condensation process. Thus far the physics-guided networks have been applied to multi-species mixing and evaporation processes. It is necessary to investigate the error and computational intensity improvement for a multi-species selective condensation process, such as selective condensation in a packed bed, to see if the results mirror those of the mixing and evaporation processes. Finally, the physics-guided network architecture should be applied to a complete hydraulic fracturing wastewater treatment system. Many of the critical input parameters (wastewater composition, flow rate, target effluent purity, etc.) have already been identified via the critical review of the field presented in Chapter Two. The additional input for the physics-guided network will be an analytically determined performance parameter of the technology.